Solid solution strengthening in single-phase Mo alloys

Zur Erlangung des akademischen Grades eines

DOKTORS DER INGENIEURWISSENSCHAFTEN
(DR.-ING.)

von der KIT-Fakultät Maschinenbau des

Karlsruher Instituts für Technologie (KIT)

angenommene

DISSERTATION

von

M.Sc. Georg Winkens

aus Jülich

Tag der mündlichen Prüfung: 26.04.2024

Hauptreferentin: Prof. Dr. rer. nat. Ruth Schwaiger

Korreferent: Prof. Dr.-Ing. Martin Heilmaier

Korreferent: Prof. Dr. mont. Christoph Kirchlechner

Abstract

In body-centered cubic metals and alloys, screw dislocations are considered to control the strength due to their high critical stress. However, recent experimental and theoretical works on multicomponent solid solutions indicate a similar critical stress for edge dislocations in these alloys. With increasing atomic misfits due to different atomic sizes, the critical stress increases for edge dislocations, until a transition from screw to edge dislocation-controlled strength is achieved. While individual alloys have been identified as either screw or edge dislocation-controlled, the transition has not been observed in a systematic study yet. Consequently, the prerequisites to achieve this transition are not yet known.

While in multicomponent systems superimposed strengthening contributions from precipitation or local atomic ordering might occur, an investigation of binary solid solutions precludes potential problems from chemical complexity. Here, Mo-Ti and Mo-Nb solid solutions were investigated systematically. Both systems cover a similar range of lattice parameters, however, while the lattice parameter in Mo-Ti solid solutions increases strongly non-linearly with Ti content, the one in Mo-Nb changes almost linearly. Accordingly, the former presents a system where both small and large atomic misfits are realized within a single system and the latter serves as reference system with an intermediate misfit value. Mechanical testing from the nanometer to the millimeter scale revealed no significant strength contributions from grain boundaries or oxides potentially formed at grain boundaries. The combination of several chemical analysis methods revealed a significant amount of O dissolved in Ti-rich Mo-Ti solid solutions. As the O impacts the total yield strength, it is corrected for, consistent to the applied strengthening models. The remaining substitutional solid solution strengthening is compared to the models by Labusch, Suzuki as well as Maresca and Curtin to identify the strength-controlling dislocation types. While the strength in both systems can be described as controlled by screw dislocation motion, when appropriate energy parameters are used in the models, the parameter-free model for edge dislocation-controlled strength by Maresca and Curtin indicates competitive strengthening in both systems when certain misfit thresholds are surpassed.

These threshold values, when taking the shear modulus into account, allow for a comprehensive screening of binary and multicomponent solid solutions for candidate systems with edge dislocation-controlled strength to aid future model-guided alloy design.

Zusammenfassung

In kubisch-raumzentrierten Metallen und Legierungen gelten Schraubenversetzungen als bestimmend für die Festigkeit, da eine hohe Schubspannung für ihre Bewegung aufgewandt werden muss. Aktuelle experimentelle und theoretische Ergebnisse in Mehrkomponentenlegierungen zeigen allerdings ähnlich hohe Schubspannungen für Stufenversetzungen. Mit steigendem atomaren Volumenunterschied zwischen den Komponenten steigt auch die kritische Schubspannung für Stufenversetzungen, bis ein Übergang von schrauben- zu stufenversetzungskontrollierter Festigkeit möglich ist. Während einzelne Legierungen eindeutig als schrauben- oder stufenversetzungskontrolliert identifiziert worden sind, gibt es bisher keine systematischen Untersuchungen, die den Übergang abbilden. Dementsprechend sind die Voraussetzungen für diesen Übergang bisher unbekannt.
In Mehrkomponentenlegierungen können Ausscheidungen und lokale atomare Ordnung zusätzlich die Festigkeit erhöhen, während eine Untersuchung in binären Systemen mit reduzierter chemischer Komplexität diese Probleme vermeidet. In dieser Arbeit wurden daher Mo-Ti- und Mo-Nb-Mischkristalle systematisch untersucht. Die Gesamtänderung des Gitterparameters bei hohen Ti und Nb-Gehalten ist ähnlich, allerdings steigt der Gitterparameter in Mo-Ti stark nicht-linear mit steigendem Ti-Gehalt, während er in Mo-Nb nahezu linear ansteigt. Dementsprechend liegen in dem ersten System Legierungen mit kleinen und großen Volumenunterschieden vor, während das zweite System als Vergleich mit mittelgroßem Volumenunterschied dient. Mechanische Prüfverfahren von der Nanometer- bis zur Millimeterskala konnten signifikante Beiträge durch Korngrenzenverfestigung oder möglichen Ausscheidungen ausschließen. Die Kombination von mehreren chemischen Analyseverfahren ergab eine signifikante Menge von interstitiell gelöstem O in den Ti-reichen Mischkristallen. Dieser Einfluss auf die Festigkeit konnte mit modellkonsistenten Ansätzen korrigiert werden. Die verbleibende Substitutionsmischkristallverfestigung wurde mit Modellen von Labusch, Suzuki, sowie Maresca und Curtin verglichen, um die festigkeitsbestimmenden Versetzungstypen zu identifizieren. Beide Systeme können durch die Modelle für Schraubenversetzungen beschrieben werden, wenn entsprechende Energieparameter gewählt werden. Das parameterfreie Modell für die stufenversetzungskontrollierte Festigkeit beschreibt die Festigkeit in beiden Systemen, sobald ein bestimmter Grenzwert für den Volumenunterschied überschritten wird.
Unter Berücksichtigung des Schubmoduls lässt es dieser Grenzwert zu, alle binären und auch mehrkomponentigen Mischkristalle auf eine mögliche stufenversetzungskontrollierte Festigkeit zu untersuchen, um Vorhersagen für modellgestützte Legierungsentwicklung zu verbessern.

Nomenclature

Abbreviations

Abbreviation	Description
APT	Atom probe tomography
BCC	Body-centered cubic
BE	Base element
BSE	Backscattered electron
DDI	Dislocation-dislocation interactions
DFT	Density-functional theory
EDS	Energy-dispersive X-Ray emission spectroscopy
FCC	Face-centered cubic
GND	Geometrically necessary dislocations
HCGE	Hot carrier gas extraction
HCP	Hexagonally-closed packed
HT	Homogenization treatment
ICP-OES	Inductively-coupled plasma - optical emission spectroscopy
ISE	Indentation size effect
MSS	Multicomponent solid solution
NI	Nanoindentation
SEM	Scanning electron micropscopy
SS	Solid solution
TEM	Trasmission electron microscopy
TRIP	Transformation-induced plasticity
TWIP	Twinning-induced plasticity
UPS	Ultrasonic phase spectroscopy
VRH	Voigt-Reuss-Hill
XRD	X-ray diffraction

Symbols

Symbol	Description	Unit
a	Lattice parameter	m
a_P	Potential valley distance	m
A	Area	m^2
A_V	Area of Vickers indent	m^2
A_0	Initial sample area	m^2
α	weighting factor	-
α_V	Angle between pyramid faces	$^\circ$
b	Length of the Burgers vector	m
B	Bulk modulus	Pa
C_ij	Single crystal stiffnesses	Pa
d_i	Indent diagonal lengths	m
d_avg	Average indent diagonal length	m
d_G	Grain size	m
d_{hkl}	Distance of planes with Laue indices hkl	m
D	Numerical factor in the Labusch model	-
D'	Numerical factor in the Labusch model	-
δ	Varvenne misfit	-
δ_F	Fleischer misfit	-
e_A	Number of valence electrons per atom	-
E	Young's modulus	Pa
E_red	Reduced modulus	Pa
E_Ind	Indentation modulus	Pa
E_SD	Solute-dislocation interaction energy	J
E_kink	Kink formation energy	J
E_SI	Energy to form self-interstitials	J
E_V	Energy to form vacancies	J
ΔE_b	Energy barrier	J
$\Delta \tilde{E}_\mathrm{p}$	Change in solute-dislocation interaction energy	J
ε_E	Engineering strain	-
ε_F	strengthening parameter in the Fleischer model	-
ε_L	strengthening parameter in the Labusch model	-
$\dot{\varepsilon}$	Experimental strain rate	1/s
$\dot{\varepsilon}_0$	Reference strain rate	1/s
η	Dielastic interaction parameter	-
η'	Corrected dielastic interaction parameter	-
f_corr	Correction function	-
f_edge	Edge dislocation pressure field	-
f^{E_b}	Numerical factor	-
f^{τ_y0}	Numerical factor	-
F	Force	N
g	Gravitational acceleration	$\mathrm{m\,s}^{-2}$
G	Shear modulus	Pa
Γ	Dislocation line tension	$\mathrm{J\,m}^{-1}$

h	Indentation depth	m
$\hbar$	Reduced Planck constant	J s
H	Vickers hardness	Pa
H_{V}	Vickers hardness	$\mathrm{kgf\,m^{-2}}$
nH	Nanohardness	Pa
ΔH	Experimental enthalpy barrier	J
I	X-ray intensity	$\mathrm{W\,m^{-2}}$
k	Boltzmann constant	$\mathrm{J\,K^{-1}}$
k_{G}	Number of counted grains	-
K	Effective anisotropic shear modulus	Pa
K_m	Misfit volume ratio for interstitial species m	-
κ	Energy barrier parameter	-
l_0	Initial sample height	m
L	Kink glide distance	m
L_{G}	Length of lines for grain size determination	m
L_0	Kink glide distance at critical stress	m
λ	Wavelength	m
Δl	Change in sample height	m
m	Strain rate sensitivity	-
μ	Pearson correlation coefficient	-
n	Constituent elements of a solid solution	-
ν	Poisson's ratio	-
ν_{D}	Debye frequency	Hz
P	Load	N
P_{S}	Term used in the Suzuki model	Pa^4
Q	Term used in the Suzuki model	-
R	Term used in the Suzuki model	Pa^4
R^2	Coefficient of determination	-
R^2_{adj}	Adjusted coefficient of determination	-
ρ	Dislocation density	$\mathrm{m^{-2}}$
S	Term used in the Suzuki model	Pa^3
S_{c}	Contact stiffness	$\mathrm{N\,m^{-1}}$
S_{ij}	Single crystal compliances	$\mathrm{Pa^{-1}}$
$\sigma_{\mathrm{px\%}}$	x% Offset yield strength	Pa
σ_{E}	Engineering stress	Pa
σ_{y}	Yield strength	Pa
T	Temperature	K
Θ	Scattering angle	-
Θ_{D}	Debye temperature	K
τ_{b}	Backstress for kink glide	Pa
τ_{c}	Critical stress	Pa
τ_{ch}	Characteristic stress in the Maresca-Curtin model	Pa
τ_{k}	Stress required for kink glide	Pa

τ_{P}	Stress required for Peierls-like advancement	Pa
τ_{xk}	Stress required for cross-kink breaking	Pa
τ_{y}	Yield strength	Pa
$\Delta\tau_{\mathrm{c,F}}$	Increase in critical stress in the Fleischer model	Pa
$\Delta\tau_{\mathrm{c,L}}$	Increase in critical stress in the Labusch model	Pa
T_{D}	Temperature of onset of diffusion-controlled strength	K or °C
T_{K}	Knee temperature	K or °C
T_{M}	Melting temperature	K or °C
T_{S}	Solidus temperature	K or °C
ΔU	Solute-dislocation interaction energy	J
v	Velocity	$\mathrm{m\,s^{-1}}$
V	Unit cell volume	$\mathrm{m^3}$
V_{P}	Potential barrier	J
V^*	Activation volume	$\mathrm{m^3}$
ΔV	Misfit volume	$\mathrm{m^3}$
w_{c}	Bow-out of a dislocation	m
w_{k}	Kink width	m
x	Solute concentration	at%
ξ	Line tension parameter	-
ζ_{C}	Characteristic dislocation segment length	m
ζ_{SI}	Characteristic length scale for self-interstitial formation	m
ζ_{V}	Characteristic length scale for vacancy formation	m

Contents

1 Introduction and Motivation **1**

2 Fundamentals **4**
2.1 Plastic Deformation in BCC Metals 4
2.2 Solid Solution Strengthening 9
2.3 Fleischer Model 11
2.4 Labusch Model 13
2.5 Suzuki Model 15
2.6 Maresca-Curtin Models 20
2.6.1 Edge Dislocation Model 21
2.6.2 Screw Dislocation Model 23
2.6.3 Interstitial Strengthening in the Maresca-Curtin Models . . . 27

3 Experimental Methods **28**
3.1 Synthesis 29
3.2 Homogenization Treatment 29
3.3 Sample Preparation 30
3.4 Compositional Analyses 31
3.5 Microstructural Analysis 35
3.6 X-ray Diffraction 36
3.7 Mechanical Testing 37
3.7.1 Nanoindentation 38
3.7.2 Vickers Hardness Testing 42
3.7.3 Compression Testing 43

4 Experimental Results and Discussion **45**
4.1 Microstructure 45
4.2 Crystal Structure 47
4.3 Composition 50
4.3.1 Substitutional Element Contents 50
4.3.2 Interstitial Element Contents 51
4.4 Lattice Parameter 53
4.5 Misfit Parameter 54
4.6 Indentation Modulus 56
4.7 Mechanical Properties 57
4.7.1 Hardness 57
4.7.2 Offset Yield Strength 59
4.7.3 Correlation Analyses 61

5 Modelling Results and Discussion **64**
5.1 Shear Modulus Modelling 65
5.2 Interstitial Strengthening 71
5.3 Labusch Model 75
5.4 Suzuki-Rao Model 78
5.5 Maresca-Curtin Models 88
5.5.1 Edge Dislocation Model 88
5.5.2 Screw Dislocation Modelling in Mo-Ti 91
5.5.3 Screw Dislocation Modelling in Mo-Nb 93
5.6 Comparison of Interaction Energy Parameters 94
5.7 Deformation Mechanisms 96
5.8 Implications for Alloy Design 99

6 Conclusions **106**

7 Appendix **109**
7.1 Compression Testing Data 109
7.2 Nanoindentation Data 111
7.2.1 Mo-Ti solid solutions 111
7.2.2 Mo-Nb solid solutions 116

8 Acknowledgements **119**

List of Publications **120**

List of Figures **121**

List of Tables **123**

1 Introduction and Motivation

Refractory metals are those with high melting temperatures, $T_{\mathrm{M}} \gtrsim 2000°\mathrm{C}$. Especially the refractory metals of the fourth to sixth group of the periodic table have thus gathered an increasing interest for high temperature applications [1]. For the application in moving parts, for example in turbines of aircraft engines, a high yield strength and creep resistance are desired for mechanical stability, while a low density is required for engine efficiency. In practice, the required strength for high temperature applications is achieved by combining several strengthening mechanisms. In Ni-based superalloys, the current industry standard for turbine blades [2], the high yield strength is achieved by alloying elements for solid solution strengthening and precipitation strengthening as well as the use of single crystalline materials [3].

Recently developed multicomponent solid solutions (MSS) made from refractory metals show a competitive yield strength solely caused by solid solution strengthening, and maintain this high strength even at high temperatures, see Fig. 1.1 [4]. Two refractory metal solid solutions, equimolar Nb-Mo-Ta-W (red) and V-Nb-Mo-Ta-W (blue), retain their large yield strength up to 1600°C. The strength of two commercially available Ni-based alloys, Inconel718 (black dashed line) and Haynes230 (black solid line), which use a combination of several strengthening mechanisms, decreases rapidly above 700°C. These results are a promising starting point for further developments based on refractory metal alloys, but the densities of these alloys are still too high for a competitive commercial application. Thus, low-density refractory metals might be added or replace the ones used. However, this might impact the effectiveness of solid solution strengthening in these systems. For finding the optimal balance between these properties, computer-assisted alloy design can be used [5], where algorithms screen a large number of possible alloy compositions automatically. However, this process relies on accurate model predictions for the material properties, and established assumptions for the modelling of solid solution strengthening have been disputed recently [6], as outlined in the following.

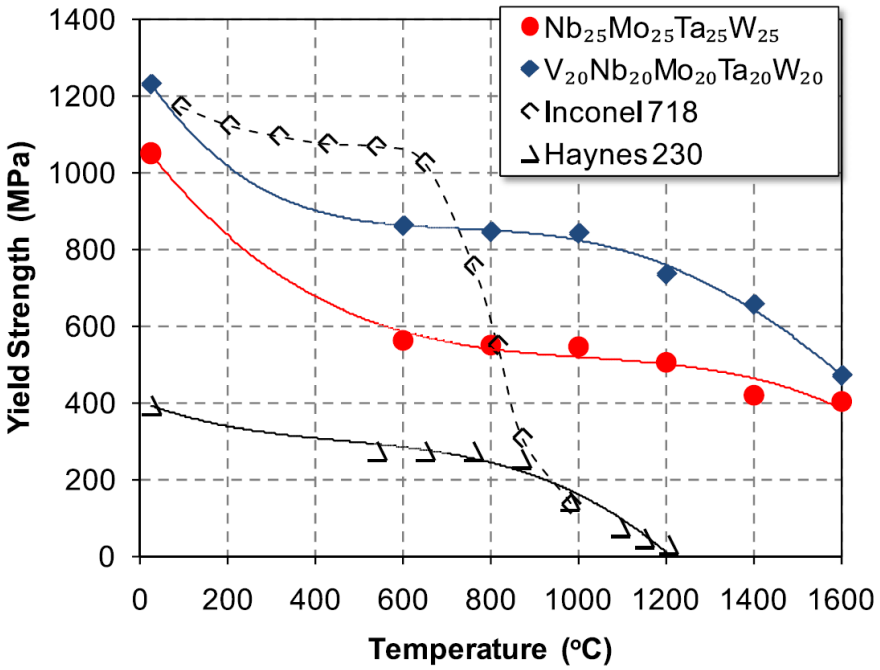

Figure 1.1: The yield strength as a function of temperature of two refractory metal solid solutions, equimolar Nb-Mo-Ta-W (red) and V-Nb-Mo-Ta-W (blue), compared to two commercially available Ni-based superalloys used in high temperature applications, Inconel718 (black dashed line) and Haynes230 (black solid line). While the Ni-based superalloys require the combination of several strengthening mechanisms for their application profile, refractory alloys can obtain competitive strength solely by solid solution strengthening. *Reproduced with permission from Ref. [4].*

For yielding, the onset of plastic deformation, dislocations must glide through the material. For body-centered cubic (BCC) metals and alloys, like many refractory metals and their solid solutions, screw dislocations are known to control the yield strength due to their high intrinsic energy barrier [7]. This barrier increases with the introduction of solutes, leading to solid solution strengthening [7]. In solid solutions, screw dislocations were still considered to control the yield strength [8]. This widely accepted assumption was recently challenged by experimental results [9, 10] and by theoretical considerations [11]. The combination of specific solute and matrix atoms might increase the energy barrier for edge dislocations until it becomes as high as, or even higher as for screw dislocations, leading to a yield strength controlled by edge dislocations [11].

Currently, it is not well understood which alloy compositions show either the commonly assumed strength controlled by screw dislocation motion or the unexpected edge dislocation-controlled one. Only reports on individual or a few selected alloy compositions are available, where contributions of both dislocation types are investigated [10, 11, 12, 13]. Criteria for the transition from screw to edge dislocation-controlled strength can thus not be clearly identified. As a consequence, the prerequisites for alloy compositions to exhibit either screw or edge dislocation-controlled strength are unclear. Thus, predictions for unknown material compositions are difficult. The transition from screw to edge dislocation-controlled strength was studied systematically in this work to address the following main questions:

- Is it possible to identify a transition between screw and edge dislocation-controlled yield strength in BCC solid solutions?
- Do the observations allow the derivation of general guidelines for this transition?

To this end, two binary solid solution series, Mo-Ti and Mo-Nb, are investigated in this work. After a review of the plastic deformation mechanisms in BCC metals and models for solid solution strengthening, experimental strength and hardness data are analyzed which allow to isolate solid solution strengthening in these systems. The strength-controlling dislocation type is then identified for each alloy based on the available models on solid solution strengthening and, finally, criteria are derived for screw or edge dislocation-controlled yield strength in BCC solid solutions.

2 Fundamentals

This chapter begins with a review of the mechanisms of dislocation motion in BCC metals. In the second part, these fundamentals are then extended to dislocation motion in solid solutions. The models for solid solution strengthening are then discussed which have been applied to the Mo-based solid solutions in this work.

2.1 Plastic Deformation in BCC Metals

On a macroscopic level, the yield strength describes the upper stress limit for a material to undergo exclusively elastic, reversible deformation. At a microscopic level, several processes can lead to plastic, irreversible deformation, for example transformation-induced plasticity (TRIP), where the applied stress leads to a crystallographic transformation of the material [14], twinning-induced plasticity (TWIP), where the applied stress causes twinning [15] or dislocation glide, where yielding is determined by the onset of screw and edge dislocation motion [16]. This work will focus on the last mechanism as there were no indications for the earlier mechanisms in the alloys studied here.

Peierls [17] was the first to quantify the stress required to move an edge dislocation in a simple cubic model system. In this model, a dislocation has to overcome an energy barrier between favourable low-energy positions along the glide plane with the help of applied stress. Due to the periodicity of the lattice, low and high energy positions alternate periodically, see Fig. 2.1. The additional half-plane of atoms that forms the dislocation is shown in grey. Light grey indicates the low-energy positions, the intermediate high energy position is shown in dark grey. The graph in b) illustrates the barrier height with respect to the Peierls energy barrier V_P for the different dislocation positions, where a_P indicates the distance between low-energy positions. Based on this derivation, the low-energy positions are called Peierls valleys, while the energy barrier itself is called Peierls barrier. The stress necessary to overcome this barrier, the critical stress, is then called Peierls stress. Although Peierls' original concept was developed for a simplified model system, these terms are sometimes also adopted for any periodic energy barrier to dislocation motion, irrespective of the crystal structure or dislocation type [18]. These terms will also be used here due to their simplicity, while keeping the conceptual imprecision in mind.

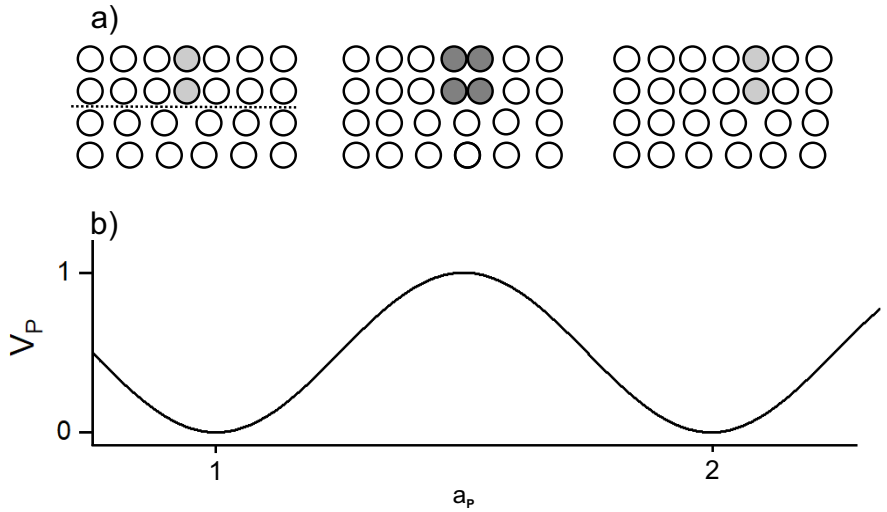

Figure 2.1: a) An edge dislocation gliding in a simple cubic structure, following the derivation of Peierls [17]. The additional half-plane of atoms is colored in grey. The bright grey color indicates low-energy positions, the Peierls valleys. The dark grey intermediate state indicates the position with highest energy. The dotted line indicates the glide plane. b) The corresponding Peierls barrier V_P, assuming a sinusoidal barrier, as a function of the dislocation position in units of the Peierls valley distance a_P.

A second energy barrier needs to be considered as well for dislocation motion. Dislocations form along many different directions within a crystal or grain. Consequently, other dislocations intersect the glide plane of a given dislocation. Dislocation-dislocation-interactions (DDI) then can lead to pinning points against glide, which need to be overcome. The combination of the Peierls barrier and the barrier set by DDI then determines the onset of dislocation motion and, consequently, yielding [19].

When the yield strength of body-centered cubic and face-centered cubic (FCC) metals is compared at different temperatures, different behaviors become apparent. In Fig. 2.2, the yield strength of polycrystalline Mo as typical BCC metal [20] (grey dashed line) and Ni as typical FCC metal [21] (black solid line) are shown as a function of temperature. The strength of Ni decreases almost linearly with increasing temperature. The slight inflection at approximately 550°C, marked as T_D, indicates the onset of diffusion-controlled dislocation motion, which further reduces the strength. For Mo, the yield strength decreases with a steep slope until approximately 300°C, the so-called knee temperature marked with T_K. Above this temperature, the yield strength behavior of Mo and Ni show similar trends. This transition will be explained below. At around 1000°C, diffusion processes become significant in Mo, leading to the steeper drop in strength with increasing temperature.

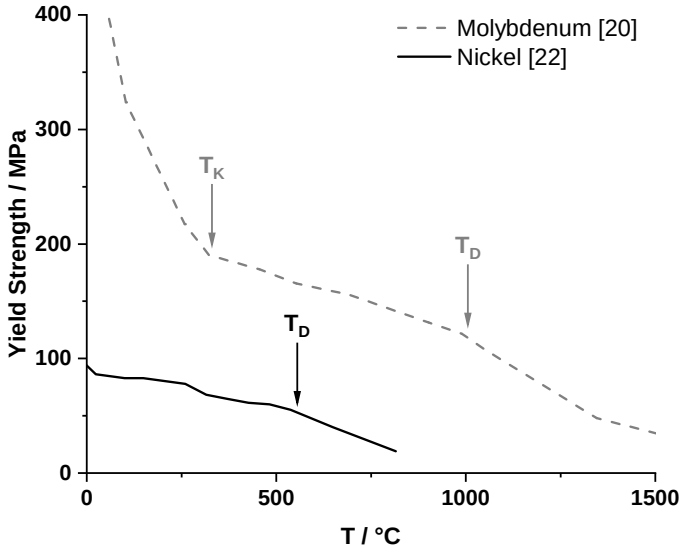

Figure 2.2: Yield strength of polycrystalline Mo [20], a typical BCC metal (grey dashed line), and polycrystalline Ni [22], a typical FCC metal (black solid line), as a function of temperature. Below the knee temperature T_K of Mo, both metals behave differently with increasing temperature. Above T_K, the behavior becomes similar. T_D marks the approximate onset of diffusion-controlled strength, leading to inflection points in the functions.

In addition to the different low-temperature slopes of Mo and Ni, BCC metals also show strain rate-sensitivity below T_K, i.e., the yield strength increases with higher applied strain rate [23]. Both low-temperature phenomena indicate that dislocation motion must differ in both crystal structures below this critical temperature.

A peculiarity of screw dislocations in BCC metals leads to this different behavior between both structures [8]. Screw dislocations are aligned along $\langle 111 \rangle$ directions in a BCC structure. Viewed along this direction, local stresses around the screw dislocation core simultaneously extend on several non-parallel planes [24]. Fig. 2.3 shows results of a simulation of the atomic displacements around a screw dislocation in Mo as differential-displacement maps. The arrows indicate the difference in atomic positions around the dislocation compared to the non-distorted crystal, normalized to $b/3$, where b is the length of the Burgers vector [25]. Fig. 2.3 a) shows displacements along the dislocation line, out of the paper plane, b) shows displacements perpendicular to it, magnified by a factor of 15 [26]. The displacements are localized along three non-parallel $\{110\}$ planes, indicated as arrows in the bottom left. In BCC structures, these are the close-packed ones, thus these are also the expected glide planes. However $\{112\}$ and $\{123\}$ planes, which also contain the $0.5\,a\,\langle 111 \rangle$ Burgers vector, have also been reported [27]. This dislocation core extension onto several non-parallel planes, its *non-planar core structure*, is unique to screw dislocations in BCC metals from among dislocations in BCC and FCC metals [28] and leads to the different behavior of BCC and FCC metals.

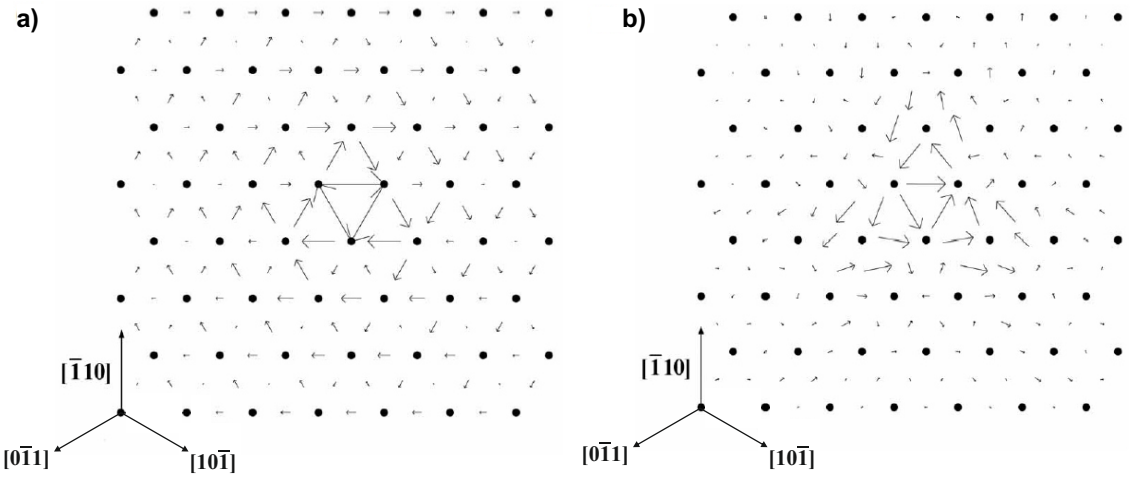

Figure 2.3: Differential displacement maps for a screw dislocation in Mo, viewed along $\langle 111 \rangle$. The arrows indicate the difference in nearest-neighbor positions of atoms between an undistorted crystal and a crystal with dislocation. All arrows are normalized so that the longest arrows indicate a displacement by $b/3$ [25]. The 110 planes are indicated. a) For displacements along the dislocation line direction, i.e, out of the paper plane, and b) for displacements perpendicular to it. These arrows have been magnified by a factor of 15. The threefold symmetry parallel to the 110 planes becomes apparent, i.e., the non-planar core structure of screw dislocations. *Reproduced with permission from Ref. [26]. Copyright ©2006 Taylor & Francis Group.*

In order to advance a screw dislocation, its core has to be transformed temporarily into a planar one, extended only on one distinct glide plane, which is an energetically costly process [28]. Thus, screw dislocations in BCC structures have a much larger energy barrier against motion and, accordingly, much higher critical stresses are required to advance screw dislocations. For example, simulations in Mo indicate a critical stress ten [29] or 30 times [30] as high for screw as for edge dislocations.
For screw dislocations, it is thus more favorable to advance only small segments at once instead of the entire dislocation, see Fig. 2.4. The non-planar dislocation core becomes planar for this small segment only, which then is able to advance into the next Peierls valley, where the core relaxes again into its non-planar configuration. This small dislocation segment is still connected to the remaining dislocation line via step-like extensions across the energy barrier, which are called kink-pairs. With applied stress, the kinks can glide along the barrier away from each other, moving the dislocation stepwise into the next valley. The required stresses for kink glide along the constant energy barrier are small compared to the ones required for kink-pair formation [8].

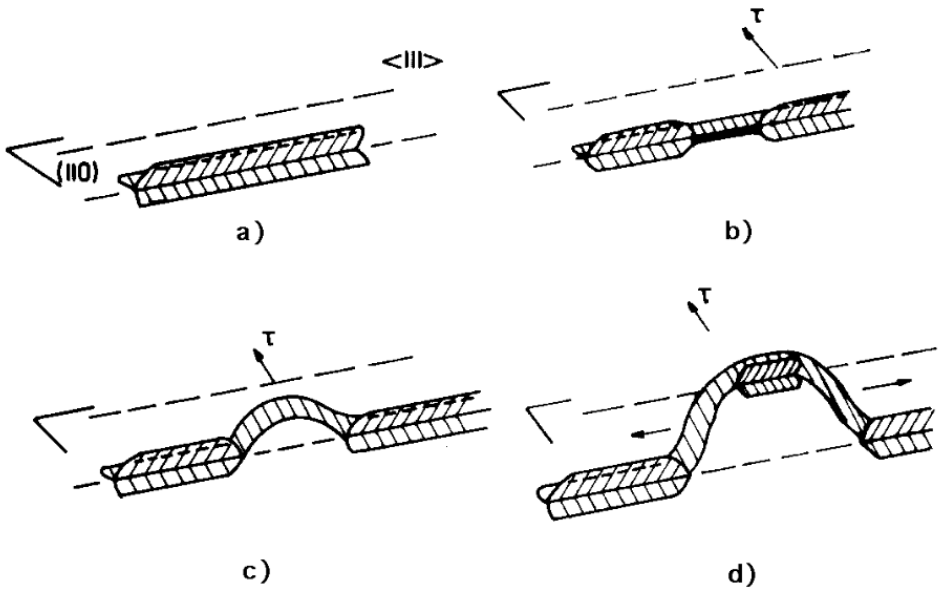

Figure 2.4: An illustration of the dislocation advancement via kink-pair formation. a) A screw dislocation lying in $\langle 111 \rangle$ direction in an Peierls valley (dashed line). The non-planar dislocation core is illustrated as the three extending lobes along the (110), (101) and (011) planes, cf. also Fig. 2.3. b) When a stress τ is applied, the latter two lobes become confined onto the (110) plane. c) The now planar core segment extends across the barrier into the neighboring Peierls valley. d) The core of the small advanced dislocation segment becomes non-planar again to lower its energy. The now formed kink-pair is able to glide along the dislocation line. *Reproduced from Ref. [28] with permission.*

The formation of kink-pairs can be assisted by thermal energy and/or applied stress [19]. This explains the strong temperature dependency of the yield strength in BCC metals: With increasing temperature, the number of kink-pairs formed in a given time interval increases, leading to additional dislocation motion and thus lower resistance against applied stress. At a constant temperature, only a limited number of kink-pairs is formed in a given time interval via thermal assistance. Thus, to accommodate higher deformation rates, additional activation of kink-pair formation via applied stress is required, leading to a higher yield strength. Above T_{K}, sufficient thermal energy is available so that kink-pair formation does not limit the dislocation motion, and only DDI controls the motion. Thus, BCC and FCC metal behave similarly above T_{K}.

As the energy barriers for screw and edge dislocations are very different in BCC metals, one might assume that plastic deformation should be controlled exclusively by the motion of edge dislocations, i.e., the process with lower energy barrier. It is activated at lower applied stresses than screw dislocation motion. The experimental results show, however, that the high energy process, the advancement of screw dislocations, is the rate-limiting one. To explain this discrepancy, the process of dislocation multiplication needs to be taken into consideration. To obtain plastic deformation on a macroscopic scale, more dislocations have to glide than are intrinsically available. Thus, additional dislocations have to be generated for plastic deformation, e.g., by activation of Frank-Read sources [31]. These sources generate a dislocation loop, a combination of screw and edge dislocation segments. Both types of segments have to glide away from the source before new dislocations can be generated [32]. Thus, the higher energy barrier for screw dislocation motion controls the dislocation source activation and, correspondingly, the plastic deformation behavior.

2.2 Solid Solution Strengthening

The yield strength of solid solutions, i.e. single-phase alloys containing more than one atom species, changes compared to a pure metal. Except for the uncommon case of solid solution softening [33], solid solutions show a larger yield strength compared to the pure base element, the so-called solid solution strengthening. Thus, solute atoms must act as additional energy barriers against dislocation motion and thus cause the observed solid solution strengthening. As the high energy barrier for screw dislocations is a phenomenon based on the crystallographic properties of BCC structures, screw dislocations were considered to be deformation rate-limiting in BCC solid solutions as well (see, e.g., Refs. [7, 8]).

Modelling of solid solution strengthening attempts to quantify the resulting increase in yield strength based on the interactions between solute atoms and dislocations. Some early models, like the ones developed by Fleischer [34] and Labusch [35], did not consider the advancement of screw dislocations by kink-pair formation. They assumed both screw and edge dislocations to glide with low intrinsic energy barriers, only hindered by DDI. Solute atoms would then locally increase the barrier, pinning the dislocation [34, 35]. Suzuki [36] developed the first model for solid solution strengthening that includes the advancement via kink-pair formation and kink glide. In this model, the kink-pair formation itself is not altered by the addition of solutes. However, solute atoms increase the energy barrier for kink glide along the barrier, which then leads to an increase in stress required to advance a screw dislocation into the neighboring valley.

With the development of MSS in the last decades, solid solution strengthening in BCC alloys found new interest (see Ref. [1], for example), and the models developed by Labusch [37] and Suzuki [38], initially developed for binary solid solutions, were expanded to include an arbitrary number of different solute atoms. Experimental results indicated an unexpected contribution of edge dislocation motion [9, 10]. Maresca and Curtin [11] developed a model to explain this observation: Due to strong interactions between the strained lattice and edge dislocations [35, 39], the energy barrier might increase until it becomes as large as or even surpass the barrier for screw dislocations, which then would lead to edge dislocation-controlled yield strength in these alloys. Based on the same framework as for edge dislocation motion, Maresca and Curtin also developed a model for screw dislocation motion in the presence of solutes which respects the high intrinsic barrier [40].
All models mentioned above have been applied in the past three years to model the strength of BCC solid solutions [11, 38, 40, 41]. However, comprehensive comparisons of the applicability of these models in concentrated BCC solid solutions are not available. To that end, in this work, strengthening controlled by screw and edge dislocations will be evaluated using four different models. They will be reviewed and then compared to experimental results in order to determine the strength-controlling dislocation types:

(i) The Labusch model [35], which is able to model both screw and edge dislocation-controlled solid solution strengthening. Although it does not consider the large difference in energy barrier for both dislocation types, it has been applied to BCC solid solutions [41, 42, 43].

(ii) The Suzuki model [36], which only considers screw dislocation-controlled strength by increasing the kink glide barrier due to solutes. This model has been applied successfully to many BCC solid solutions, e.g., in Refs. [44, 45]. It continues to be developed and extended [46]. However, its mathematical complexity and the necessity for input parameters calculated by density-functional theory (DFT) have limited its application.

(iii) The Maresca-Curtin models for a) screw dislocation-controlled strength [40, 47] and b) edge dislocation-controlled strength [11]. Based on common assumptions, but considering the differences in energy barrier, two individual models were developed for screw and edge dislocations.

2.3 Fleischer Model

In the Fleischer model [34, 48], a dislocation glides unhindered under applied stress until it encounters solute atoms on its glide plane. Upon contact, the dislocation becomes pinned at these anchor points and it bows out between the solutes. It is assumed that the dislocation bows out between solutes until solutes are contacted at a constant distance. These pinning points for the dislocation can be overcome, when the critical stress is reached. Dislocation segments then break away from the anchor points and advance freely until the next solutes are encountered. This situation is illustrated in Fig. 2.5.

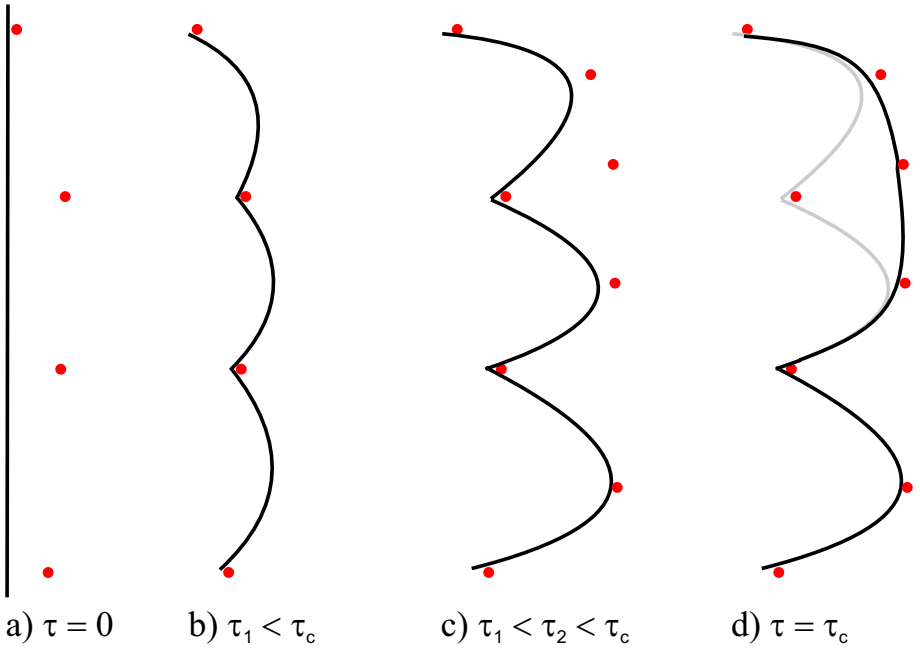

Figure 2.5: Schematic representation of dislocation-solute interactions in the Fleischer model [34, 48]. a) Without applied stress τ, the black dislocation line lies straight on the glide plane between point-like solute atoms located on the plane (red dots). b) When a small stress τ_1 is applied, the dislocation glides, until it contacts the solutes. c) At higher applied stress, $\tau_2 > \tau_1$, the dislocation bows out more strongly between the solutes, but remains pinned. d) When a critical stress τ_c is reached, dislocation segments break away and advance to the next solutes, indicated as grey and black line before and after the local breakaway, respectively.

Fleischer assumed that the energy barrier is equal for all solutes and can be described as a step-like function, i.e., either the dislocation encounters the full potential barrier or none at all [49]. According to Fleischer [34, 48], the barrier height, and consequently the required critical stress, is determined by two contributions:
(i) Due to the different atomic sizes of solute and matrix atoms, the lattice is locally distorted. This distortion, also called lattice misfit, then interacts with the stress field around a dislocation. Fleischer quantifies this contribution via

$$\delta_{\mathrm{F}} = \frac{1}{a} \cdot \frac{\mathrm{d}a}{\mathrm{d}x} \tag{2.1}$$

Where a is the lattice parameter and x the solute concentration [48].

(ii) A local change in shear modulus due to solute atoms leads to a change in elastic energy stored in the dislocation, analogously to (i) called modulus misfit.

$$\eta' = \frac{\eta}{0.5\eta + 1} \quad \text{with} \tag{2.2}$$

$$\eta = \frac{1}{G} \cdot \frac{\mathrm{d}G}{\mathrm{d}x} \tag{2.3}$$

Where G is the alloy shear modulus.
The considerations of Fleischer then lead to an increase in critical stress compared to the pure base element as

$$\Delta\tau_{\mathrm{c,F}} \propto \varepsilon_{\mathrm{F}}^{3/2}\, x^{1/2} \tag{2.4}$$

Here, ε_{F} combines the contributions of both misfits assuming a linear superposition of both effects as $\varepsilon_{\mathrm{F}} = \alpha\,\delta_{\mathrm{F}} + \eta'$. The numerical factor α quantifies the interaction strength of the lattice misfit with screw and edge dislocations, suggested to be $\alpha = 16$ for edge dislocations and $\alpha = 3$ for screw dislocations based on correlation plots with experimental data [34]. These numbers reflect the stronger interactions between the hydrostatic stress components of the solute and the edge dislocation compared to the short range stress components of the screw dislocation.

2.4 Labusch Model

The Labusch model [35] builds upon some of the considerations described above. However, a number of improvements are incorporated, see Fig. 2.6:

(i) The model accounts for the random distribution of solute atoms, i.e., the assumption of a constant distance between pinning solutes is lifted.

(ii) It introduces a gradually changing interaction potential over distance between solutes and dislocation instead of a step-like function. Accordingly, an interaction range of the potential also needs to be assumed.

(iii) Not just solutes directly on the glide plane are considered, but those on neighboring parallel planes as well, leading to dislocation obstacles with different strengths.

(iv) The total dislocation energy is minimized in a trade-off between dislocation line tension and local energy maxima due to the solute configuration. This allows local deviations from a straight dislocation line to avoid unfavorable solute configurations.

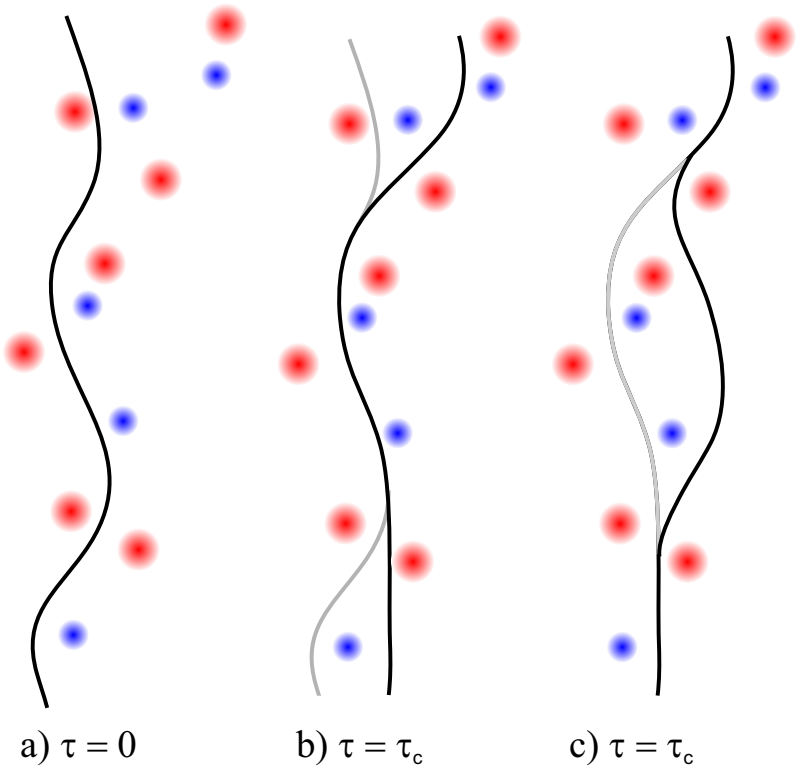

Figure 2.6: Schematic representation of the dislocation motion in the Labusch model [35]. a) Without applied stress τ, the black dislocation line bows out between solutes. The red solutes lie in the glide plane, the smaller blue ones on neighboring planes. Accordingly, their interaction strengths are different, indicated as circle size. b), c) When the critical stress τ_c is reached, dislocation segments can overcome locally the energy barrier set by the solute configuration. In b), the outer two segments have advanced. The former positions are indicated by the grey line. In c), also the center segment has advanced.

In order to advance the dislocation, additional energy is required to overcome these local barriers. Labusch [35] derives a system of equations to describe the interplay between line tension and a random distribution of solutes. This system can then be solved for the energetically most favorable dislocation shape, and consequently the expected energy barrier for the most unfavorable solute configuration. The critical stress to overcome this barrier, $\Delta\tau_{\mathrm{c,L}}$, is [35]

$$\Delta\tau_{\mathrm{c,L}} = D\,G\,\varepsilon_{\mathrm{L}}^{4/3}\,x^{2/3} \tag{2.5}$$

Which, as in the Fleischer model, has to be added to the critical stress of dislocation motion in the pure base element (BE), leading to the total stress of the solid solution as $\tau_{\mathrm{SS}} = \tau_{\mathrm{BE}} + \Delta\tau_{\mathrm{c,L}}$. Labusch [35] adopted the misfit parameters δ_{F} and η' from Fleischer, but his calculations lead to a different combination of both misfits, $\varepsilon_{\mathrm{L}} = \sqrt{\eta'^2 + \alpha^2\delta_{\mathrm{F}}^2}$. Again, α is assumed to be 16 for edge dislocations and 3 for screw dislocations. D subsumes several numerical factors dependent on the assumed shape, height and interaction range of the solute barriers. While no numerical values for D were provided initially [35], Refs. [50] and [51] give $D = 0.0013$, while Ref. [52] gives $D = 0.0018$ for Cu solid solutions based on experimental data. The latter value has also been adapted for Mo solid solutions [42, 43].

In a comprehensive comparison between the Fleischer and Labusch models of solid solution strengthening, Leyson and Curtin [53] found that the latter should be preferred over the Fleischer model for solute concentrations $x \gtrsim 0.01\,\mathrm{at\%}$, where the exact transition concentration depends on the used input values. Thus, for all practical applications, the Labusch model should be used. As the Labusch model has been applied to model solid solution strengthening in BCC solid solutions [41, 42, 43] it will be evaluated here against the experimental data.

A formulation for two different solute species was presented as $\Delta\tau_{\mathrm{c,L}} = D\,G\,(x_1\,\varepsilon_1^2 + x_2\,\varepsilon_2^2)^{2/3}$ [49] and adopted in an early model for solid solution strengthening in MSS in generalized form [37]. Recent works [41, 43] applied the Labusch model to experimental data in binary BCC refractory solid solutions. In Ref [43], the average measured change in hardness per solute concentration was compared to the Labusch strengthening parameter in dilute Mo solid solutions, evaluating $\Delta H/\Delta x \simeq \partial H/\partial x \propto \varepsilon_{\mathrm{L}}$. The highest correlation factor R^2 was found for $\alpha = 18$. Ref. [41] used the difference in measured hardness between concentrated, refractory solid solutions and the pure constituent metals in comparison to the Labusch model prediction, $\Delta H \propto G\,\varepsilon_{\mathrm{L}}^{4/3}\,x^{2/3}$. The best correlation quality was achieved for $\alpha = 16$. Both results thus indicate edge dislocations as strength-controlling dislocation type in these solid solutions.

Due to the large difference in critical stress for screw and edge dislocations in BCC metals, an experimental determination of $\Delta\tau_{\mathrm{c,L}}$ always refers to (the higher) $\tau_{\mathrm{c,screw}}$. Thus, values obtained for $\Delta\tau_{\mathrm{c,L}}$ resemble a lower bound for strengthening and, therefore, a lower bound for α.

2.5 Suzuki Model

In contrast to the Fleischer and Labusch models described above, the Suzuki model [36, 54, 55] addresses the high critical stress for screw dislocation motion and the resulting motion by kink glide in BCC alloys. The energy required for kink-pair formation is assumed to be much lower than the energy required for kink glide and is therefore neglected. Accordingly, kink-pair formation is not considered a deformation rate-limiting contribution, and it is assumed that there is always a sufficient number of kink-pairs available [36]. The concepts used in the Suzuki model are presented in Fig. 2.7. An initially straight dislocation line (a) spontaneously forms kink-pairs when stress is applied (b). These kinks then can glide along the dislocation line when sufficient stress is applied to overcome the energy barrier set by the solute fluctuations, advancing the dislocation segment-wise (c). When kink-pairs on different glide planes form (d) and glide, they form cross-kinks, which serve as high energy barrier positions for kinks.

During kink glide, the atomic environment around a screw dislocation changes, depending on the number of solute atoms entering or leaving the vicinity. According to Suzuki's calculations [36], the six closest atom columns around the dislocation line interact significantly with the dislocation and impact the energetic environment during kink glide. Therefore, these six closest positions are used in the model, see Fig. 2.8.

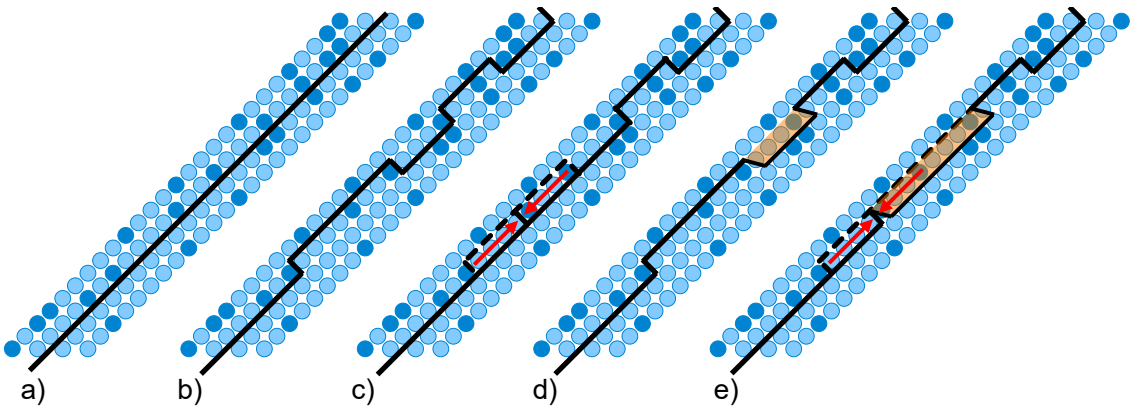

Figure 2.7: Fundamental concepts used in the Suzuki model. a) Without applied stress, the dislocation line (black line) lies straight in the glide plane. Light and dark blue atoms indicate constituent atoms in a binary solid solution. b) When stress is applied, kink-pairs form spontaneously along the dislocation line. c) Kinks glide along the dislocation line (red arrows), changing the local atomic environment of the dislocation. d) Kink-pairs can form on different possible glide planes. Here, the orange shaded kink-pair forms on a different glide plane. e) When kinks from different glide planes collide, a cross-kink is formed, which represents a strong pinning point against further dislocation motion.

Stress is required for kinks to glide along the dislocation line to counteract the mutual attraction of the kinks in a pair [8]. However, due to the constantly changing energetic environment during kink glide, the stress for kink glide in a solid solution increases significantly compared to the kink glide in a metal. The solute distribution and thus the distribution of encountered energy barriers is a statistical process and the following equation is derived for the average kink glide distance L [55]:

$$\frac{1}{\sqrt{2\,\pi}} \int_{\kappa_\mathrm{t}}^{\infty} \exp(-0.5\,y^2)\mathrm{d}y = \frac{b}{3\,L\,x\,(1-x)} \tag{2.6}$$

x is the solute concentration[1], b is the length of the Burgers vector and κ is a dimensionless parameter characterizing the energy barrier height for kink glide. The average glide distance is then calculated based on the probability for a kink to encounter a barrier of threshold height κ_t or larger [44]. This barrier is eventually overcome by thermal assistance after a dwell time based on the Debye frequency ν_D. This waiting time is assumed to be large compared to the actual glide duration for the calculation of the velocity of a kink v_kink [44]. Each kink on a screw dislocation glides by L on average, moving the entire dislocation by the distance of one Peierls valley a_P. Thus, $L/v_\mathrm{kink} = a_\mathrm{P}/v_\mathrm{dislocation}$. This provides a link between the statistics of individual kink motion and macroscopic deformation [55].

Using an equation for the dislocation density [56] and a term for the activation enthalpy of kink motion, the following expression for the stress required to move kinks, τ_k, was derived [44]:

$$0 = \tau_\mathrm{k}^4 + S \cdot \tau_\mathrm{k} - R \tag{2.7}$$

where

$$S = \frac{18\,\kappa_\mathrm{t}^2\,E_\mathrm{SD}^2\,x\,(1-x)\,kT}{a_\mathrm{P}^3\,b^4\,w_\mathrm{k}^2} \cdot \ln\left(\frac{(5\,\pi\,kT)^2\,\nu_\mathrm{D}\,a_\mathrm{P}\,b^2}{(G\,b\,V^*)^2\dot{\varepsilon}\,w_\mathrm{k}}\right) \tag{2.8}$$

$$R = \frac{27\,\kappa_\mathrm{t}^4\,E_\mathrm{SD}^4\,x^2\,(1-x)^2}{a_\mathrm{P}^4\,b^6\,w_\mathrm{k}^2} \tag{2.9}$$

$$V^* = \frac{3\,\kappa_\mathrm{t}^2\,E_\mathrm{SD}^2\,x\,(1-x)}{2\,\tau_\mathrm{k}^2\,a_\mathrm{P}\,b^2} + \frac{\tau_\mathrm{k}^2\,a_\mathrm{P}^3\,b^4\,w_\mathrm{k}^2}{6\,\kappa_\mathrm{t}^2\,E_\mathrm{SD}^2\,x\,(1-x)} \tag{2.10}$$

In these equations, E_SD denotes the interaction energy between a solute and the dislocation. $k\,T$ is the thermal energy using Boltzmann's constant k and the absolute temperature T. w_k is the kink width, the average distance between the kinks of a kink-pair, which is typically assumed as $w_\mathrm{k} \approx 10\,b$ [40, 45]. V^* is the activation volume of deformation. $\dot{\varepsilon}$ denotes the experimental strain rate. ν_D is the Debye frequency, which is used to estimate the dwell time and calculated from the Debye temperature as $\nu_\mathrm{D} = \Theta_\mathrm{D} \cdot \frac{k}{\hbar}$ using the thermal energy and the reduced Planck constant $\hbar$.

[1] In contrast to Ref. [55], Refs. [36, 38, 44, 54] replace the term $x(1-x)$ by x. None of the authors, not even Suzuki, comment on this difference. The first version is symmetrical around $x = 0.5$, when the solute element becomes the matrix and vice versa. The second term can be considered an approximation for small concentrations, $x\,(1-x) \approx x$ for $x \ll 1$. As the model is applied to concentrated solid solutions in this work, the complete term will be used.

In the second term of Eq. 2.10 for the activation volume, the term $x\,(1-x)$ appears in the denominator. For dilute solid solutions, the equation then results in unrealistically large activation volumes. In these cases, the strength contribution from kink-pair formation cannot be neglected in comparison to the other processes, thus a fundamental model assumption is invalid. Rao et al. [46] give a minimum solute concentration of $x = 5\,\text{at}\%$ for the Suzuki model.

Kink-pairs can form on different glide planes. When gliding kinks from different planes collide, cross-kinks are formed. These cross-kinks represent a high energy barrier against any further kink glide with $\kappa \geq \kappa_\text{t}$, see Fig. 2.7. Thus, cross-kinks are assumed to form at an average distance of $2\,L$ and can be overcome by bowing out of the dislocation in between the cross-kinks, similar to the process in precipitate strengthening. The stress to overcome these cross-kinks τ_xk is then calculated as [55]

$$\tau_\text{xk} = \frac{G\,b}{4\,L} \tag{2.11}$$

The strength contributions of kink glide and the cross-kink mechanism add up to the total strength τ_total,

$$\tau_\text{total} = \tau_\text{k} + \tau_\text{xk} \tag{2.12}$$

τ_xk decreases with increasing glide distance L, while τ_k increases. Thus, the total strength reaches a minimum value for an intermediate distance of L_0, i.e. $\partial\tau_\text{total}/\partial L = 0$ at L_0. The critical stress required to advance the dislocation is then the value of τ_total at that glide distance, $\tau_\text{total}(L_0) = \tau_\text{y}$. The minimization of τ_total with respect to L results in the following equation [44]:

$$\kappa_\text{t}^2 - \ln\left(\kappa_\text{t}^2\right) - 2\ln\left(\frac{3\,G\,x\,(1-x)}{4\,\sqrt{2\,\pi}\,\tau_\text{k}\,Q}\right) = 0 \tag{2.13}$$

With the abbreviations Q and P

$$Q = \frac{2\,S\,\tau_\text{k} - 4\,R - P_\text{S}}{3\,S\,\tau_\text{k} - 4\,R - P_\text{S}} \tag{2.14}$$

$$P_\text{S} = \frac{4\,kT}{V^*}\,\frac{3\,S\,\tau_\text{k} - 2\,R}{\tau_\text{k}} \tag{2.15}$$

where all quantities are defined above, see Eqs. 2.7 to 2.10. When P_S is omitted to simplify the calculations [54, 55], a relative error of less than 1% is made [44]. As the inclusion of P_S does not change the calculation times significantly on modern computers, it is included in the calculations presented below. Eqs. 2.6, 2.7, 2.11, 2.12, 2.13, together with the equations for P_S, Q, R, S and V^* have to be solved simultaneously. The complexity of this set of interdependent equations has hindered a widespread application and further developments based on this model for a long time.

Twenty years after its original publication, an approximation for small concentrations was derived and applied to dilute Fe solid solutions [44]. However, this simplified set of equations still required numerical solutions using a computer. A strongly simplified approximation was also suggested [55]:

$$\tau_{\mathrm{y,simple}} = \frac{E_{\mathrm{SD}}^2\, x\,(1-x)}{3\,kT\,b^3} \tag{2.16}$$

The recent advancements in computation power allow to determine the interaction energy E_{SD} via DFT calculations more precisely than earlier estimates and allow to find numerical solutions for the set of equations more rapidly. Based on the success in predicting the strength in several MSS [38], the model was subsequently expanded by Rao and co-workers [45, 46, 57]. Several modifications to the original formulation have been proposed:
(i) Instead of an Orowan-like mechanism for the bow-out between cross-kinks, breaking is considered, which requires the formation of vacancy-self-interstitial dipoles. Thus, Eq. 2.11 is replaced:

$$\tau_{\mathrm{xk}} = 0.707\,\frac{E_{\mathrm{SI}} + E_{\mathrm{V}}}{4\,b^2\,L} \tag{2.17}$$

where E_{SI} and E_{V} are the energies required to form self-interstitials and vacancies, respectively [45].
(ii) For systems containing more than two components, two different extensions are proposed. Following the concept that all constituent elements can be considered solutes in a virtual average alloy [40], strengthening contributions by all constituent elements n are calculated individually [45]. The total MSS strength is then calculated as $\tau_{\mathrm{total,\,MSS}} = \sum_n \tau_n$. Alternatively, the interaction energies for different solutes E_n are combined via $E_{\mathrm{total}}^2 = \sum_n E_n^2 \cdot x_n$ with their respective concentrations x_n to a total interaction energy. This then replaces the value E_{SD} in the original model.
(iii) Suzuki [36, 54, 55] assumed a constant energy interaction parameter E_{SD} between atoms of the six closest columns (nearest and second-nearest neighbors) and the screw dislocation. In the extension, this interaction is expanded to more atom columns. Additionally, the interaction energy is allowed to be different among the different neighboring columns based on DFT calculation results, see Fig. 2.8. In a), the relative interaction energy between solute positions and a dislocation (blue dot) are presented as numbers in the circles according to Suzuki's original calculations [36]. Nearest neighbor atomic columns are indicated as orange circles, second-nearest ones as brown circles, and their energies are assumed to be equal, $0.93 \approx 1$. Farther neighboring positions, which are shown in white, are not included in the Suzuki model calculations. In b), DFT calculated, relative energy values are presented exemplary for Mo solutes in Nb [46]. The relative strengths of third-(yellow) and fourth-nearest (light red) neighbors were also included in the calculation of the total interaction energy. The reference value for nearest neighbors is $E_{1,\text{Mo in Nb}} = 200\,\mathrm{meV}$.
In the three closest shells of atomic columns surrounding the dislocation, the respective energy contributions would be E_1, E_2 and E_3, for the columns in the first, second, and third nearest shells, respectively. By counting how many atoms change their relative position to the dislocation after a glide to the next Peierls valley, an

equation for the total change in interaction energy E_{SD} is obtained. This change in energy is redistributed onto the six closest atoms, which maintains the fundamental statistical considerations from Refs. [36, 54, 55]. For the three closest neighboring columns, the formula yields

$$6\,E_{\mathrm{SD}}^2 = 6\,E_3^2 + 2\,E_2^2 + 2\,(E_1 - E_3)^2 + 2\,(E_3 - E_2)^2 + 2\,(E_1 - E_2)^2 \tag{2.18}$$

The authors of Ref. [46] note the generality of this Ansatz to include interactions with farther atom columns. Values for these interaction energies are currently only available by first-principles simulations, e.g., for Mo, Ti and W solutes in Nb [46].
(iv) At high temperatures, diffusion leads to a recombination of vacancy-self-interstitial dipoles. During dislocation advancement, this leads to a gradient of vacancy and self-interstitial concentrations with respect to the dislocation, and, as a consequence, an additional drag on the cross-kinks and an increase in strength [45]. Rao et al. [45] estimate this phenomenon to be active above $\approx 0.5\,T_{\mathrm{S}}$. It will not be considered further here, as in this work, only room temperature behavior (e.g., $T_{\mathrm{room}} \approx 0.13\,T_{\mathrm{S}}$ for Mo-50Ti) is studied.

In addition to the modifications for substitutional solid solution strengthening, Ref. [57] proposes an adaptation for interstitial strengthening in BCC refractory metals. A linear dependency of yield strength on the interstitial solute concentration was reported, for example, for up to 0.24 at% O in Nb.

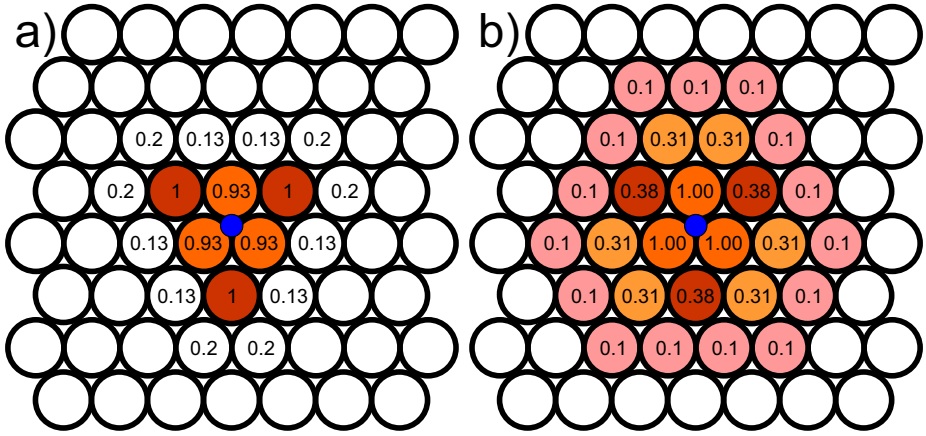

Figure 2.8: Atomic columns in a BCC structure, viewed along a ⟨111⟩ direction. The blue dot represents a screw dislocation. Colored circles represent the atomic columns that are considered for solute-dislocation interactions in (a) the original Suzuki model [55] and (b) the extended model by Rao et al. [46]. Nearest-neighbor to fourth nearest-neighbor atomic columns of the dislocation are coded using orange, brown, yellow and light red, respectively. Columns of white circles are not considered in the respective models. The numbers in the circles indicate the relative strength of interaction energy between dislocation and solute atoms located in the respective column, according to (a) Suzuki's calculations relative to a fundamental interaction energy E_{SD} for each alloy system [55] and (b) according to DFT calculations for Mo solutes in Nb, using $E_{\mathrm{F,Mo\ in\ Nb}} = 200\,\mathrm{meV}$ as reference.

2.6 Maresca-Curtin Models

The Maresca-Curtin models [11, 40] were developed for solid solutions with an arbitrary number of constituent elements n. Each atom, also the matrix atoms in a binary solid solution, is considered a solute in a hypothetical "average alloy", which has the macroscopic properties of the random solid solution [39]. Interactions between a dislocation and the atoms arise then from the local deviations between the properties of the average alloy and the properties due to the actual atomic configuration. If experimental data of the properties of the macroscopically average alloy are not available, they can usually be approximated by a linear rule-of-mixture of the respective constituent element properties (e.g., Refs. [11, 12, 13, 58], but see Ref. [59] for a counter-example).

Following the considerations by Labusch [35], the dislocation shape can deviate from a straight line in a trade-off between dislocation line tension and energetically unfavorable local element fluctuations [39]. However, shortcomings of the Labusch model, e.g., the necessary assumption of the interaction range, are addressed [39]. Two characteristic length scales arise naturally for a non-straight dislocation from the calculations: Assuming the dislocation is aligned along the z-direction, segments of a characteristic length ζ_c parallel to z bow out. In the $x-y$-plane, perpendicular to the dislocation line, these segments bow by an average distance of w_c away from the initially straight dislocation line. In the Maresca-Curtin models, the total change in solute-dislocation interaction energy by bowing out, $\Delta\tilde{E}_\mathrm{p}(w_\mathrm{c})$, is described as [39]

$$\left(\Delta\tilde{E}_\mathrm{p}(w_\mathrm{c})\right)^2 = \sum_{n,i,j} x_n \, \Delta U_n(x_i, y_j)^2 \quad \text{with} \tag{2.19}$$

$$\Delta U_n(x_i, y_j) = U_n(x_i + w_\mathrm{c}, y_j) - U_n(x_i, y_j) \tag{2.20}$$

By bowing out by w_c (arbitrarily set along the x-direction), the interaction energy U_n between a solute of species n at position (x_i, y_j) and the dislocation changes by ΔU_n. The changes in interaction energy are then subsumed for all solute species at all possible positions (x_i, y_j), weighted by their respective concentrations x_n, in the parameter $\Delta\tilde{E}_\mathrm{p}$.

Again, adapting the assumptions of the Labusch model as described in Sec. 2.4, the bow-out reduces the potential energy while the elastic energy of the dislocation increases. For edge dislocations, this is considered via an elastic energy proportional to the dislocation line tension, $\Gamma_\mathrm{elastic} \propto \xi\, G\, b^2$, with ξ being a numerical constant. Due to the low intrinsic barrier, the dislocation bow-out w_c can extend across several Peierls valleys. For screw dislocations with high barrier, the dislocation can only bow out into the next Peierls valley by forming kink-pairs, and then $w_\mathrm{c} = a_\mathrm{P}$. Accordingly, the energy increase is calculated using the kink formation energy E_kink. Calculating the minimum of the total dislocation energy with respect to w_c and ζ_c yields results for these length scales and allows to derive the energy barriers required to advance a dislocation [11, 40].

2.6.1 Edge Dislocation Model

When only elastic interactions between a dislocation and solute atoms are assumed, the solute-dislocation interaction energy can be described as [11]

$$U_n(x_i, y_j) = -\frac{G}{3\,\pi}\,\frac{1+\nu}{1-\nu}\,f_{\text{edge}}(x_i, y_j)\Delta V_n \tag{2.21}$$

Where G and ν are the shear modulus and Poisson's ratio of the alloy, respectively. This allows to separate the solute specific misfit volume ΔV_n from the dimensionless dislocation stress field for an edge dislocation $f_{\text{edge}}(x_i, y_j)$, which is independent of the solute species. Using Eqs. 2.19 and 2.20 and minimizing the total dislocation energy, $f_{\text{edge}}(x_i, y_j)$ reduces to two numerical values, $f^{\tau_{\text{y0}}}$ and $f^{E_{\text{b}}}$ for the zero Kelvin strength and the energy barrier, respectively. In Ref. [11], numerical values for these parameters were obtained by comparing the elastic approximation to exact numerical simulations for different solute-matrix combinations. A single set of $f^{\tau_{\text{y0}}}$ and $f^{E_{\text{b}}}$ yielded good agreement between the approximated model and simulated data for alloys containing two, three, four and five elements [11]. The resulting equations for $\tau_{\text{y0,edge}}$ and ΔE_{b} are then

$$\tau_{\text{y0,edge}} = 0.04\,\xi^{-1/3}\,G\,\left(\frac{1+\nu}{1-\nu}\right)^{4/3}\left[\frac{\sum_n x_n\,\Delta V_n^2}{b^6}\right]^{2/3} \tag{2.22}$$

$$\Delta E_{\text{b}} = 2\,\xi^{1/3}\;G\,b^3\left(\frac{1+\nu}{1-\nu}\right)^{2/3}\left[\frac{\sum_n x_n\,\Delta V_n^2}{b^6}\right]^{1/3} \tag{2.23}$$

Combining these results with equations for the strain rate and shear strength as a function of energy barrier, a phenomenological equation for the yield strength is obtained

$$\sigma_{\text{y,edge}}(T, \dot{\varepsilon}) = 3.06 \cdot \tau_{\text{y0,edge}} \cdot \exp\left(-\frac{1}{0.55}\left(\frac{kT}{\Delta E_{\text{b}}} \cdot \ln\left(\frac{\dot{\varepsilon}_0}{\dot{\varepsilon}}\right)\right)^{0.91}\right) \tag{2.24}$$

where $\dot{\varepsilon}_0 = 10^4\,\text{s}^{-1}$ is a reference strain rate [11], $\dot{\varepsilon}$ the experimental strain rate and $k\,T$ the thermal energy. A Taylor factor of 3.06 was included here for edge dislocation slip in polycrystalline BCC alloys ($\langle 111\rangle$ slip directions, $\{1\bar{1}0\}$ slip planes) [60].

One important contribution to edge dislocation strengthening in this model is the misfit volume term $\sum_n x_n \, \Delta V_n^2$, which quantifies the difference in atomic volume of the actual solid solution compared to the hypothetical average alloy. In Ref. [61], the formal definition for ΔV_n is presented as

$$\Delta V_n = \sum_m x_m \left(\frac{\partial \, V_{\text{alloy}}}{\partial \, x_n} - \frac{\partial \, V_{\text{alloy}}}{\partial \, x_m} \right) \tag{2.25}$$

with n and m both indicating solute species. For MSS, this definition thus requires full information about the change in atomic volume of the alloy as a function of all constituent elements. Instead, an approximation is commonly used, where the difference between the atomic volumes of the constituent elements V_n and the alloy V_{alloy} is calculated [5, 12, 13]

$$\Delta V_n = \sum_m x_m \, (V_n - V_{\text{alloy}}) \tag{2.26}$$

For binary solid solutions, the change in atomic volume as a function of the concentrations of the constituent elements can be obtained. Accordingly, a more precise calculation of the volume misfit is possible and, as a consequence, a more precise calculation of edge dislocation-controlled strengthening. Using the chain rule, the partial derivatives in Eq. 2.25 can be rewritten as

$$\frac{\partial V}{\partial x_n} = \frac{\partial V}{\partial a} \frac{\partial a}{\partial x_n} = 1.5 \, a^2 \, \frac{\partial a}{\partial x_n} \tag{2.27}$$

where $V = a^3/2$ as atomic volume for BCC structures was used. Thus,

$$\Delta V_n = 1.5 \, a^2 \sum_m x_m \left(\frac{\partial \, a}{\partial \, x_n} - \frac{\partial \, a}{\partial \, x_m} \right) \tag{2.28}$$

This leads in a binary system with $m = 1$ or 2 to

$$\Delta V_1 = 1.5 \, a^2 \, x_2 \left(\frac{\partial a}{\partial x_1} - \frac{\partial a}{\partial x_2} \right) \tag{2.29}$$

$$\Delta V_2 = 1.5 \, a^2 \, x_1 \left(\frac{\partial a}{\partial x_2} - \frac{\partial a}{\partial x_1} \right) \tag{2.30}$$

When the lattice parameter is expressed as function of one of the constituent elements, $a = a(x_1)$, then

$$\Delta V_1 = 1.5 \, a^2 \, (1 - x_1) \, \frac{\mathrm{d}a}{\mathrm{d}x_1} \tag{2.31}$$

$$\Delta V_2 = -1.5 \, a^2 \, x_1 \, \frac{\mathrm{d}a}{\mathrm{d}x_1} \tag{2.32}$$

Similar to the lattice misfit used in the Fleischer and Labusch models, δ_{F}, a dimensionless volume misfit parameter has been defined [61]

$$\delta = \frac{1}{3 V_{\text{alloy}}} \sqrt{\sum_n x_n \, \Delta V_n^2} \tag{2.33}$$

where V_{alloy} is the unit cell volume of the alloy. Inserting Eqs. 2.31 and 2.32 reveals a relationship between both misfit quantities for binary systems as

$$\delta = \delta_{\text{F}} \sqrt{x \, (1 - x)} \tag{2.34}$$

2.6.2 Screw Dislocation Model

In contrast to the model for edge dislocations, a separation of dislocation pressure field and solute dependent properties (like the volume misfit) is not possible. Thus, the interaction energy between dislocation and solutes remains in the model as parameter. Due to the high energy barrier, the bow-out distance w_c becomes the separation of neighboring Peierls valleys a_P. The combination of reducing the dislocation energy due to local favorable solute configuration, described by $\Delta\tilde{E}_\mathrm{p}$, and the necessity to form kink-pairs, included as kink formation energy E_kink, leads to a characteristic length scale ζ_c

$$\zeta_\mathrm{c} = \left(1.083\,\frac{E_\mathrm{kink}}{\Delta\tilde{E}_\mathrm{p}}\right)^2 b \tag{2.35}$$

The average dislocation segment length is then $2.5\,\zeta_\mathrm{c}$.
As the dislocation is already kinked in its inital state, the stress for kink-pair formation is not included in this model. Ghafarollahi and Curtin [47] developed a model for dilute solid solutions, where kink formation is included. In this model, additional input data are required, which can be obtained, e.g., by DFT calculations. As they estimate a significant impact only below solute concentrations of 5 at%, it is not further considered for the concentrated solid solutions studied in this work. Three mechanisms are considered for the advancement of screw dislocations, see also Fig. 2.9:

(i) A mechanisms similar to the original concept developed by Peierls, where a complete segment of length $2.5\,\zeta_\mathrm{c}$ advances by a_P simultaneously, accordingly denoted as "Peierls-like advancement".

(ii) The glide of kinks along the dislocation line with an average glide distance $2.5\,\zeta_\mathrm{c}$ in a changing energy environment.

(iii) The breaking of cross-kinks, which form when kinks on different glide planes collide.

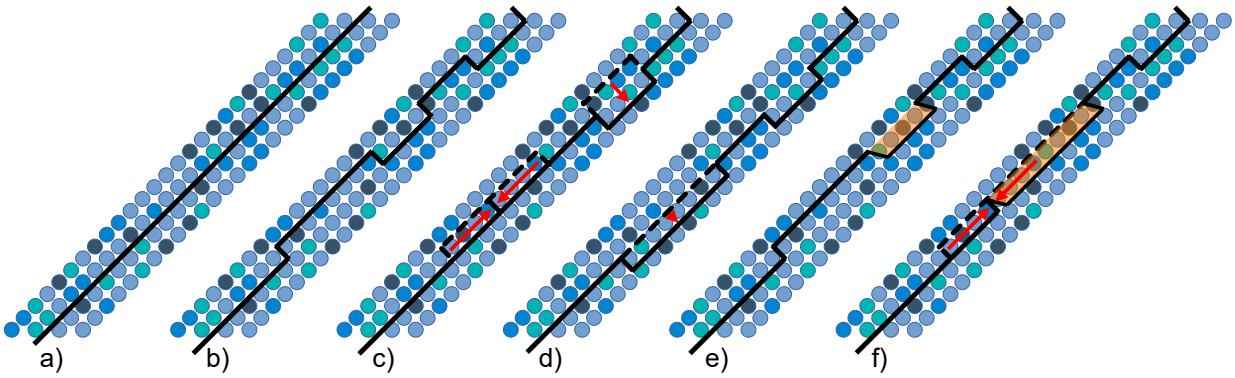

Figure 2.9: Fundamental concepts used in the Maresca-Curtin screw dislocation model [11]. a) A straight dislocation line (black line) in a MSS (different atomic species indicated as blue shades) spontaneously forms kinks to lower its total energy (b). c) When stress is applied, these kinks glide along the dislocation and advance it to an unstable high-energy position (lower red arrows). At low temperatures or high stresses, entire dislocation segments can also advance simultaneously (upper red arrow). d) The high-energy segment obtained by kink glide advances another valley into a lower energy configuration, thereby forming a new kink-pair. e) Kink-pairs can form on different possible glide planes. Here, the orange shaded kink-pair forms on a different glide plane. f) When kinks from different glide planes collide, a cross-kink is formed, which represents a strong pinning point preventing further dislocation motion.

For screw dislocation motion, the breaking of cross-kinks is always necessary. Additionally, the mechanism of lower energy, either the Peierls-like advancement or kink glide, is active.

$$\sigma_{\mathrm{y,screw}} = 2.74\ \left(\tau_{\mathrm{xk}} + \min\left[\tau_{\mathrm{k}}, \tau_{\mathrm{P}}\right]\right) \tag{2.36}$$

where a Taylor factor of 2.74 for screw dislocation slip in a random BCC polycrystal by pencil-glide ($\langle 111 \rangle$ slip directions, multiple sets of slip planes) [60] is used. The three mechanisms will be briefly described below.

Peierls-like Advancement

This mechanism describes the advancement of an entire dislocation segment of length $2.5\,\zeta_{\mathrm{c}}$ into the next Peierls valley [47], similar to the original concept derived by Peierls [17]. The stress required for Peierls-like advancement,τ_{P}, is calculated as [47]

$$\tau_{\mathrm{P}} = \tau_{\mathrm{P},0}\left[1 - \left(\frac{\Delta H}{\Delta E_{\mathrm{b,P}}}\right)^{2/3}\right] \tag{2.37}$$

with (2.38)

$$\tau_{\mathrm{P},0} = \frac{\pi V_{\mathrm{P}}}{a_{\mathrm{P}}\, b} + \frac{0.44\, E_{\mathrm{kink}}}{a_{\mathrm{P}}\, b\, \zeta_{\mathrm{c}}}\left(1 - \frac{5\, V_{\mathrm{P}}\zeta_{\mathrm{c}}}{20\, V_{\mathrm{P}}\, \zeta_{\mathrm{c}} + 0.7\, E_{\mathrm{kink}}}\right) \tag{2.39}$$

$$\Delta H = kT\, \ln\left(\frac{\dot{\varepsilon}_0}{\dot{\varepsilon}}\right) \tag{2.40}$$

$$\Delta E_{\mathrm{b,P}} = \frac{\left(10\, V_{\mathrm{P}}\zeta_{\mathrm{c}} + 0.7\, E_{\mathrm{kink}}\right)^3}{\left(20\, V_{\mathrm{P}}\zeta_{\mathrm{c}} + 0.7\, E_{\mathrm{kink}}\right)^2} \tag{2.41}$$

with the zero Kelvin stress $\tau_{\mathrm{P},0}$, the total energy barrier $\Delta E_{\mathrm{b,P}}$, V_{P} the intrinsic Peierls barrier of the average alloy, and the experimentally set enthalpy barrier ΔH using the same values as discussed above. For this phenomenon to be significant, either thermally assisted kink-pair formation and glide must be suppressed or large applied stress reduces the required energy sufficiently to advance entire segments. Accordingly, this mechanism is only active at high stresses and/or low temperatures. For example for Mo-Nb solid solutions, this mechanism was found to be active below 100 K at a strain rate of 0.001 1/s [11] and is, thus, not further considered here.

Cross-Kink Breaking

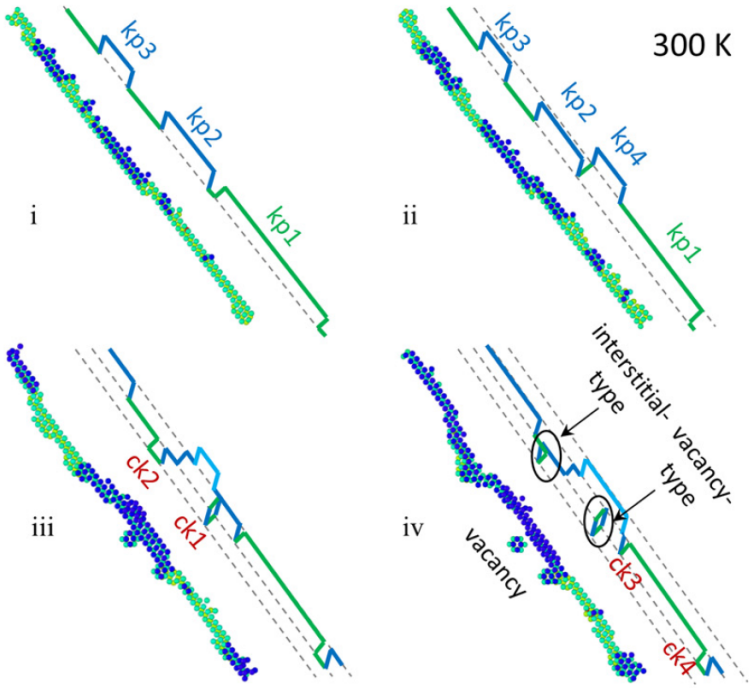

Figure 2.10: The mechanisms for the formation of vacancy and self-interstitial loops to break cross-kink pinning. In the left part of each image, the atomic positions close to the dislocation core as obtained from molecular dynamics simulations are shown. The right part of each image shows a corresponding sketch using the dislocation line visualization. i) A dislocation, where three kink-pairs formed, abbreviated as "kp". The dark blue and green colors indicate the formation on different glide planes. Dark blue and green atoms indicate the formation of the respective kink-pairs. ii) A new kink-pair, kp4, forms on the plane parallel to kp2 and kp3 in the neighboring Peierls valley. iii) kp2 advances on the plane parallel to kp1, closing the loop marked at ck1. At ck2, another cross-kink between green and blue kinks forms. A new kink-pair colored in light blue, forms on the blue segment which closed the loop at ck1. iv) The light blue kink-pair glides along the dark blue segment, separating the vacancy loop from the dislocation. The dislocation configuration at ck2 will leave a self-interstitial loop when the dark blue segments have been connected. At the bottom, the new cross-kinks ck3 and ck4 have formed by collision of blue and green kinks. *Reproduced with permission from Ref. [62].*

Kink-pairs can form on different glide planes, when the local energy distribution allows for it. When these kinks glide under applied stress, they will eventually collide, forming a cross-kink. To advance the dislocation, these cross-kinks can be broken by the formation of vacancies and self-interstitial loops, each with their associated energy barriers E_{V} and E_{SI}, respectively. See Fig. 2.10 for the concept of cross-kink breaking. The kink-pairs "kp1" and "kp2" collide, forming a cross-kink. Depending on surrounding kink-pair formation, cross-kinks, denoted as "ck1" and "ck2", can be overcome either by formation of self-interstitials of vacancies. Note that this process includes the formation of new kink-pairs, which contradicts the fundamental assumptions of the Maresca-Curtin model. However, the additional strength contribution due to required kink-pair formation can be neglected against the overall energy requirement for this process. Since both mechanisms are simultaneously active, the one with higher energy barrier controls the cross-kink breaking. The respective temperature and stress dependent strength for both mechanisms is modelled as

$$\tau_{\mathrm{xk}} = \tau_{\mathrm{xk},0} \left[1 - \left(\frac{\Delta H}{\Delta E_{\mathrm{V/SI}}} \right)^{2/3} \right] \tag{2.42}$$

$$\tau_{\mathrm{xk},0} = \frac{\pi \, \Delta E_{\mathrm{V/SI}}}{a_{\mathrm{P}} \, b \, \zeta_{\mathrm{V/SI}}} \tag{2.43}$$

where $\tau_{\mathrm{xk},0}$ is the zero Kelvin cross-kink strength with $\Delta E_{\mathrm{V/SI}}$ and $\zeta_{\mathrm{V/SI}}$ being the energy barrier and a characteristic length scale for vacancy and self-interstitial formation, respectively, modelled as $\zeta_{\mathrm{V}} = 7.5 \, \zeta_{\mathrm{c}}$ and $\zeta_{\mathrm{SI}} = 15 \, \zeta_{\mathrm{c}}$.

Kink Glide

The dislocation is initially kinked to lower its total energy according to the solute distribution. For glide, kinks need to overcome an energy barrier based on the overall change of solute concentration. This barrier height has been derived from simulations to be $2.7 \, E_{\mathrm{kink}}$ over the glide distance $2.5 \, \zeta_{\mathrm{c}}$. While this is the overall energy increase of this distance, local energy fluctuations due to the solute distribution have to be considered, too. A statistical analysis of these local fluctuations within the framework of a Wiener process or "random walk" [63], in this case with a preferred drift direction due to the applied stress, leads to the following equation for the kink glide stress in concentrated solid solutions

$$\tau_{\mathrm{k}} \left(\dot{\varepsilon}, T \right) = \tau_{\mathrm{b}} + \tau_{\mathrm{ch}} \left[3.26 \left(\frac{\Delta H}{\Delta \tilde{E}_{\mathrm{p}}} - 0.06 \, \frac{E_{\mathrm{kink}}}{\Delta \tilde{E}_{\mathrm{p}}} + 1.07 \sqrt{w_{\mathrm{k}}/b} \right)^{-1} - 1.58 \, \frac{\Delta \tilde{E}_{\mathrm{p}}}{E_{\mathrm{kink}}} \right] \tag{2.44}$$

where $w_{\mathrm{k}} \approx 10 \, b$ is the kink width. $\tau_{\mathrm{ch}} = \Delta \tilde{E}_{\mathrm{p}} / (a_{\mathrm{P}} \, b^2)$ is a characteristic stress based on the local solute fluctuations, and $\tau_{\mathrm{b}} = 2.7 \, E_{\mathrm{kink}} / \left(2.5 \, a_{\mathrm{P}} \, b \, \zeta_{\mathrm{c}} \right)$ describes the overall stress due to the energy change over the entire length as described above.

2.6.3 Interstitial Strengthening in the Maresca-Curtin Models

The Maresca-Curtin models allow for modelling substitutional solid solution strengthening, but interstitial solid solution strengthening is not captured. While the simulation of interaction energies between interstitial atoms and screw dislocation cores in refractory metals have been published [57, 64, 65], the incorporation of interstitial atoms into the models for solid solutions is still challenging. Accordingly, the impact of interstitial solutes can only be estimated, and the mathematically simple edge dislocation model will be used for this estimate. The following three simplifications and approximations are made:

(i) Only the zero Kelvin strength (Eq. 2.22) is considered and only ratios between strengths will be compared, which remain approximately constant as a function of temperature (cf. Eq. 2.24).

(ii) The addition of interstitial atoms does not change the elastic properties of the alloy, in contrast to experimental results, e.g., for O in Nb, Ta and V [66] or a BCC Ti–Nb–Ta–Zr alloy [67].

(iii) The strengthening by interstitials is treated like strengthening by substitutional atoms, using the mathematical form of a misfit volume.

Using these assumptions, interstitial atoms contribute to the misfit $\sum_i x_i \, \Delta V_i^2$. Considering m interstitial atom species and n substitutional atom species,

$$\sum_{i=n,m} x_i \, \Delta V_i^2 = \sum_n x_n \, \Delta V_n^2 + \sum_m x_m \, \Delta V_m^2 \tag{2.45}$$

The total strength in the presence of interstitials $\tau_{\mathrm{y0,total}}$ can then be written in terms of the strength in the absence of interstitials $\tau_{\mathrm{y0,subst}}$ as

$$\tau_{\mathrm{y0,total}} = \tau_{\mathrm{y0,subst}} \cdot \left(1 + \frac{\sum_m x_m \, \Delta V_m^2}{\sum_n x_n \, \Delta V_n^2} \right)^{2/3} = \tau_{\mathrm{y0,subst}} \cdot \left(1 + \sum_m K_m \, x_m \right)^{2/3} \tag{2.46}$$

The coefficients K_m thus quantify the ratio of the respective hypothetical interstitial misfit volume for each interstitial species m relative to the total misfit due to substitutional species n. Values for K_m have to be obtained either by simulations or can be estimated using experimental data on strength as a function of interstitial content.

3 Experimental Methods

This chapter describes the experimental methods that have been used to characterize the Mo-based solid solutions. The synthesis, the homogenization treatment (HT) and the metallographic preparation are described first, as these processes form the foundation for all subsequent characterization methods. Microstructural analysis by scanning electron microscopy (SEM) was used to verify the homogeneity of the polycrystalline samples and to determine the grain size. As the mechanical properties will be compared to models for solid solution strengthening in BCC alloys, the structure needs to be verified by X-ray diffraction (XRD). Simultaneously, XRD also allows to determine the lattice parameters of the alloys, which is a crucial input parameter for some of the models.
In order to verify that the alloys were synthesized with the desired compositions, several analysis methods were applied. Energy-dispersive X-ray emission spectroscopy (EDS) and optical emission spectroscopy by inductively-coupled plasma excitation (ICP-OES) allow to determine the composition with respect to substitutional atoms. Inevitable interstitial uptake also needs to be quantified to account for potential strengthening contributions of the respective atom species. Here, hot carrier gas extraction (HCGE) and atom probe tomography (APT) were used.
The chapter then closes with the methods of mechanical testing. Nanoindentation (NI), Vickers hardness and compression testing were combined in order to isolate solid solution strengthening from other strengthening mechanisms, which then can be compared to the models.

3.1 Synthesis

All alloys were synthesized by arc melting in an AM/0.5 arc melter (Edmund Bühler GmbH, Bodelshausen, Germany) equipped with a water-cooled Cu crucible. Prior to melting, the device chamber was evacuated to a pressure of $5 \cdot 10^{-2}$ mbar and consequently purged with Ar (99.998 at% purity) for three times. A final evacuation to $2 \cdot 10^{-4}$ mbar was performed before an Ar pressure of 600 mbar was set for melting. To ensure an O_2-lean atmosphere, a Zr getter was liquefied for 10 s before each melting step in order to extract residual O_2. Each button was flipped and remelted four more times to ensure compositional homogeneity. Details on the used raw materials are listed in Tab. 3.1. An investigation by HCGE (see Sec. 3.4) revealed quality problems in the Mo supplied by EvoChem GmbH (Offenbach am Main, Germany, 99.95 wt%), thus Mo supplied by Plansee SE (Reutte, Austria, 99.97 wt%) was used for Mo-Nb solid solutions. Ti (99.8 wt%) and Nb (99.9 wt%) were supplied by ChemPur GmbH, Karlsruhe, Germany.
Mo-Ti solid solutions were synthesized in increments of $\Delta x_{\mathrm{Ti}} = 10$ at% in order to capture potential changes in strengthening mechanism due to the non-linear behavior of the lattice parameter. Samples containing $x_{\mathrm{Ti}} = 0...50$ at% were synthesized by S. Obert (IAM-WK, KIT) [68]. Mo-Nb solid solutions were synthesized in increments of $\Delta x_{\mathrm{Nb}} = 25$ at%. To obtain consistent results within each solid solution series, two separate Mo buttons were synthesized using the Mo from the different suppliers.

Table 3.1: Raw elements used for the synthesis of the solid solutions, suppliers and the purity according to the supplier.

solid solution series	elements used	supplier	purity
Mo-Ti	Mo	EvoChem	99.95 wt%
	Ti	ChemPur	99.8 wt%
Mo-Nb	Mo	Plansee	99.97 wt%
	Nb	ChemPur	99.9 wt%

3.2 Homogenization Treatment

Bulk material of Mo-Ti solid solutions containing at least 40 at% Ti was homogenized in a HRTH tube furnace (Carbolite Gero GmbH, Neuhausen, Germany) by annealing at 1600 °C for 24 h with a heating and cooling rate of 100 K h^{-1} under Ar flow. The used Al_2O_3 carrier boats were covered in Mo foil to prevent any reaction between the boat and the samples. In each homogenization treatment, an additional boat filled with new Ti sponge (99%, ChemPur GmbH, Karlsruhe, Germany) was included in the furnace to extract residual O_2 from the Ar flow.

3.3 Sample Preparation

For compression testing and NI, parallel sample faces are required for reliable results. These samples were extracted from the as-cast buttons and homogenized bulk material using electrical discharge machining to ensure sample shape. Specimens for compression testing were $5 \cdot 3 \cdot 3\,\mathrm{mm}^3$, specimens for NI $10 \cdot 5 \cdot 3\,\mathrm{mm}^3$ in size. Other samples, e.g., for microstructural and compositional analyses, XRD and Vickers hardness testing, were extracted from the buttons or homogenized material using a diamond wire saw model 7500 (well Diamantdrahtsägen GmbH, Mannheim, Germany), as there are no specific requirements for the dimensions.

The contact faces of compression testing samples were prepared by subsequent manual grinding with grit P320, P600, P1000 and P2500 SiC papers in a special sample holder to ensure parallel contact faces. All other samples were hot mounted in EpoMet F (Buehler, Lake Bluff, Illinois, USA) and automatically ground to grit P4000 SiC paper following the preparation recipe in Tab. 3.2 on an AutoMet 300 automatic grinding and polishing device (Buehler, Lake Bluff, Illinois, USA). After each preparation step, the samples were ultrasonically cleaned in an ethanol bath. The samples were polished using a mixture of OP-S (Struers, Ballerup, Denmark), which is an alkaline (pH = 9.8) suspension of colloidal 40 nm-SiO_2 particles, and a 30% concentrated H_2O_2-water solution in a ratio of 5 (OP-S):1 (H_2O_2 solution) [69]. By the addition of hydrogen peroxide, surface defects are preferably oxidized and abraded [70]. This way, a mirror-smooth surface finish was obtained. Due to different etching rates, slight height differences were observed for individual grains.
All samples used in HCGE and ICP-OES as well as bulk material for HT were cleaned from potential synthesis and extraction process contaminations by manually grinding all surfaces with grit P320 and P600 SiC papers, followed by ultrasonic cleaning in an ethanol bath.

Table 3.2: The steps performed for metallographic preparation of the samples to obtain a mirror-smooth surface. "C" indicates central force application to the sample holder in the automatic grinding/polishing device, "I" indicates force application to the individual samples. All steps were performed using counter-rotation between plate and head of the device.

		Rotation speed / min^{-1}			
Grit size	Time / s	Head	Plate	Force / N	Appl.
320, 600, 1000	30	150	200	20	C
2500	120	150	200	20	C
4000	600	150	200	20	C
Polishing steps					
OPS+H_2O_2	600	150	150	20	I
H_2O	120	150	150	20	I

3.4 Compositional Analyses

All solid solutions were characterized to determine the ratios of Mo and Ti as well as Mo and Nb. EDS was applied to all alloys, and its results were then cross-checked using ICP-OES on selected samples to detect potential systematic errors. In EDS, an incident electron beam is used to excite electrons bound to the sample atoms from their ground state. During relaxation, these electrons emit X-rays of characteristic wavelengths for each element. Thus, the sample composition can be determined from the intensity and energy of detected X-ray peaks. All samples were investigated by EDS using a Si drift detector (Thermo Fisher Scientifc Inc., Waltham, MA, USA) in an EVO50 SEM (Carl Zeiss AG, Oberkochen, Germany). Measurements were performed at an acceleration voltage of 10 keV. At least five representative regions of 320 µm by 240 µm were evaluated, where each measurement included the X-ray emission data collected from the entire region. The software package accompanying the Si drift detector (Thermo Fisher Scientifc Inc., Waltham, MA, USA) identified and quantified the elements found in EDS automatically.

On selected samples (Mo-30Ti and Mo-50Nb), the EDS results were confirmed by ICP-OES using an iCAP 7600 DUO (Thermo Fisher Scientific Inc., Waltham, MA, USA), operated by Dr. T. Bergfeldt (IAM-AWP, KIT). Three samples per composition were analyzed in ICP-OES. The working principle is presented in Fig. 3.1. The samples are liquefied in acid and nebulized into an Ar plasma torch. Collisions between Ar ions and the sample atoms ionize the latter. Recombination of the sample ions and electrons and the consequent relaxation processes lead to emission of light with a characteristic energy spectrum for each element [71], similar to the X-ray emissions used in EDS measurements. Again, the detected energy and intensity distribution allow the identification of the sample composition. Depending on the atomic shells considered during the relaxation processes, either X-ray or visible light emission is detected and used for element identification in the respective method.

Interstitial O and N contents also need to be considered due to their potential strengthening contribution. While HCGE yields global O and N contents of an entire sample volume, i.e., including potential oxides, the interstitially dissolved amounts of O and N need to be known. To compare both data sets, APT was used as complementary method.

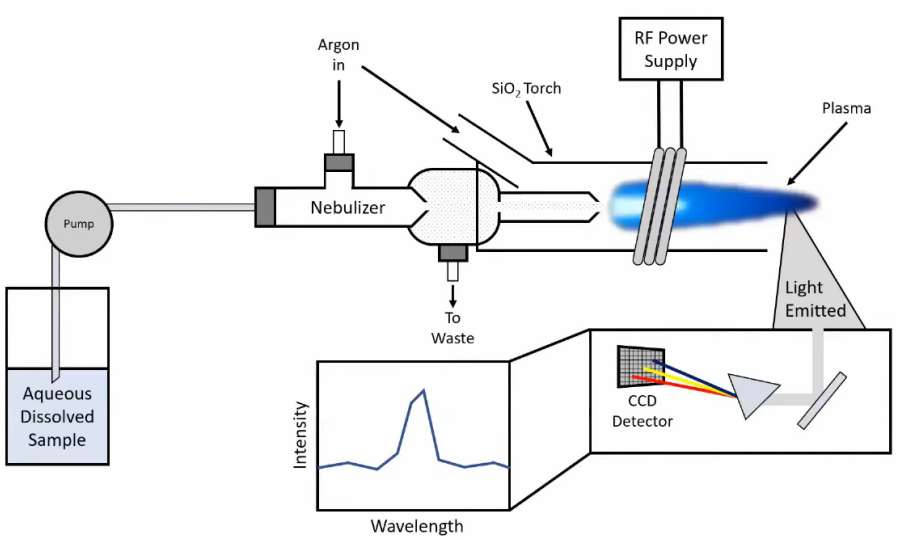

Figure 3.1: The operation principle of ICP-OES: A sample is dissolved in an acidic solution. Via a pump, the solution is transferred to a nebulizer, which sprays the solution into a SiO_2 chamber with Ar flow. The RF Power Supply introduces energy via electromagnetic fields oscillating at radio frequencies to ignite an Ar plasma, which in turn ionizes the sample solution via collisions. During recombination at the cool end of the chamber, optical light is emitted, which is recorded using a CCD detector. The resulting intensity distribution allows for identification and quantification of the elements in the sample. *Image taken from "Inductively coupled plasma optical emission spectroscopy (ICP-OES) Overview" by Z.G. Neale, U.S. Naval Research Laboratory, USA, licensed under CC-BY [71].*

Global contents were analyzed by HCGE using a TC600 device (Leco Instrumente, Mönchengladbach, Germany), operated by Dr. T. Bergfeldt (IAM-AWP, KIT). For each alloy, at least three samples were analyzed. In this method, a sample is evaporated in a graphite crucible using an electric arc. In a He gas stream, evaporated O_2 from the sample and C from the crucible react to CO_2, while the evaporated N forms N_2. After filtering other gaseous components, the gas mixture is analyzed in both an infrared photo cell and a thermal conductivity cell. The concentration of CO_2 is determined via its absorption of infrared light in the photo cell. The N_2 concentration is determined using the difference of thermal conductivity of the gas mixture compared to the pure carrier gas. This way, the global contents of O and N can be detected simultaneously from a single measurement [72].

Samples of Mo-10Ti and Mo-80Ti were investigated in APT by Dr. S. Seils (IAM-WK, KIT) to compare global interstitial content with dissolved interstitial contents. Sharp tips suitable for APT analysis were formed using a standard procedure for APT sample preparation, where a cantilever is extracted from the sample and placed on Si posts. On these posts, individual tips are then formed using annular ion milling (see Ref. [73], Fig. 3 a)). In this case, the cantilevers were extracted from grain centers to minimize the impact of potential O enrichment at grain boundaries. Annular milling was then performed using Ga^+ ions accelerated at 30 kV in a Strata400 dual beam SEM/focused ion beam device (FEI, Hillsboro, OR, USA). The diameter of the milling was decreased to an inner diameter of 0.2 µm. Final milling with a closed circular pattern was performed at 5 kV acceleration voltage to minimize the layer affected by Ga^+ ions on the tip surface [74]. Fig. 3.2 shows a secondary electron micrograph of a representative tip prepared for APT analysis made from a Nb-Al-O alloy, provided by M.K. Eusterholz (IAM-WK, KIT).

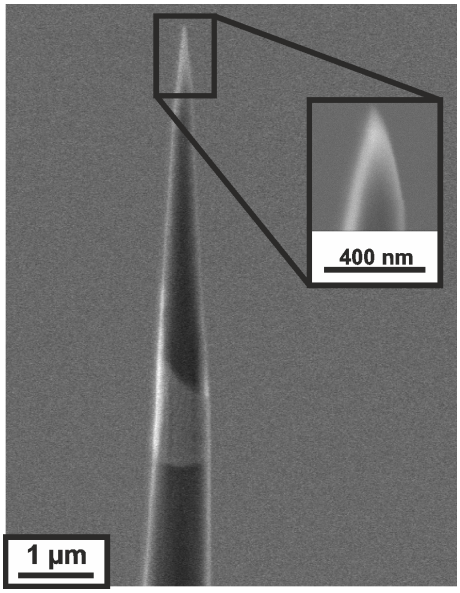

Figure 3.2: A secondary electron micrograph of a typical tip prepared for APT, in this case a tip prepared from a Nb-Al-O alloy. The inset is a magnified image of the apex. *Micrograph provided by M.K. Eusterholz (IAM-WK, KIT).*

In APT, these tip specimens are placed in vacuum with a remaining pressure of $1 \cdot 10^{-8}$ Pa or better. A high voltage of up to 10 kV is applied between the tip and the counter electrode, see also Fig. 3.3. Due to the sample geometry, large electric fields build up at the apex, leading to a high potential energy for atoms close to the tip surface. Using a laser pulse, the energy of these atoms is increased to overcome their bond energy, leading to an evaporation of the topmost atomic layer of the tip. These ionized atoms are projected onto a detector. The arrival location on the detector allows to reconstruct the tip location from which an ion was evaporated and the time between laser pulse and arrival allows to determine the mass-to-charge-ratio of each detected ion. By sequential evaporation of sample layers, a three-dimensional distribution of evaporated ions with near-atomic resolution can be obtained [73]. By comparing the data set to known atomic weights and ionic states of elements, the element distribution in the sample is obtained.
APT analyses were conducted in a LEAP 4000X HR (Cameca SAS, Gennevilliers, France). The device was operated in laser mode (UV laser with $\lambda = 355$ nm) at a pulse energy of 100 pJ and a pulse repetition rate of 100 or 125 kHz. The temperature was set to 50 K and the standing high voltage was controlled according to a detection rate of 0.3 or 0.5 %. APT data were reconstructed and analyzed by the IVAS 3.8.8 software (Cameca SAS, Gennevilliers, France). The chemical composition was determined using the peak deconvolution analysis of the software to take the possible overlap of peaks into account, especially the overlap of TiO^{2+} and $O_2{}^+$ at 32 $\frac{u}{e}$. Both Mo and Mo_2 ions were detected in APT and analyzed separately by the software. Results will be discussed for the dominant Mo ions only in Sec 4.3.
A frequency distribution analysis was performed by Dr. T. Boll (IAM-WK, KIT) to determine the homogeneity of element distribution. In this method, the detected atoms from a tip are randomly distributed into packages of 100 atoms. The frequency of atomic compositions of these packages is then compared to (perfectly random) binomial distributions using the so-called Pearson coefficient μ [75]. It quantifies the likelihood that the hypothesis *The solute is distributed randomly* must be rejected based on the frequency distribution of packages. Thus, $\mu = 0$ indicates a perfectly random distribution, while $\mu = 1$ indicates a perfectly ordered structure.

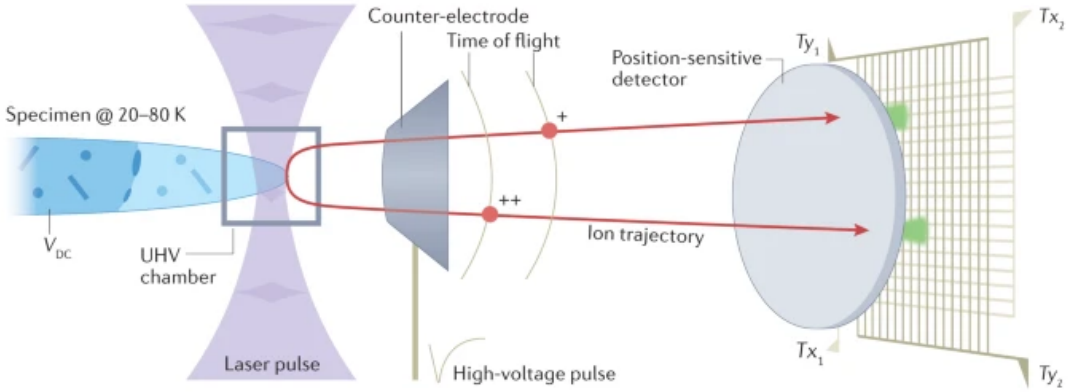

Figure 3.3: Working principle of APT. A high voltage V_{DC} is applied between tip and counter electrode. The laser pulse then evaporates the topmost atomic layer of the specimen. These ions are accelerated towards the position-sensitive detector, where, based on the detected signal position and time of flight, the original position and the mass-to-charge ratio are determined. *Reproduced with permission from Ref. [73].*

3.5 Microstructural Analysis

The microstructure was analyzed using an EVO50 SEM (Carl Zeiss AG, Oberkochen, Germany) operated at an acceleration voltage of 25 keV and equipped with a backscattered electron (BSE) detector. The samples were characterized with regard to grain size and dendrite formation. The average grain size was determined for Mo-Ti solid solutions following DIN ISO 643 [76]. On a representative BSE micrograph, five horizontal and five vertical lines are drawn. For each line of length L_{G}, the number k_{G} of completely crossed grains is counted. If a line ends in a grain, k_{G} is increased by 0.5. The grain size d_{G} is then calculated as $d_{\mathrm{G}} = L_{\mathrm{G}}/k_{\mathrm{G}}$ per line. For each composition, five BSE micrographs were evaluated this way and the results were averaged. The grain size in Mo-Nb solid solutions was not quantified.

3.6 X-ray Diffraction

In a crystal, lattice planes scatter incident X-rays. Based on constructive interference of these scattered X-rays, phase composition and the lattice parameter of the analyzed sample can be determined. When the crystal surface is irradiated at a specific angle Θ, the radiation scattered from adjacent lattice planes interferes constructively, leading to an increased X-ray intensity. This angle depends on the wavelength λ of the incident X-rays and the distance d_{hkl} of adjacent lattice planes. The mathematical description of this phenomenon is known as Bragg's law [77]:

$$2\, d_{hkl} \sin(\Theta_{hkl}) = \lambda \tag{3.1}$$

This equation is fulfilled for several plane families with their respective distances d_{hkl} and angles Θ_{hkl}, where hkl indicates the Laue indices of the respective plane family. Thus, for a constant X-ray wavelength, the interplanar distances d_{hkl} can be calculated when the respective angles of peak intensity are known. Combining this information with the relation between interplanar distance and the lattice parameter a in a cubic crystal, $d_{hkl} = a/\sqrt{h^2 + k^2 + l^2}$, the lattice parameter of the crystal can be calculated for each detected intensity peak with known indices. Based on the atom positions and the resulting electron distribution in a unit cell, additional restrictions for constructive interference arise. For a BCC unit cell, this so-called structure factor yields constructive interference only if $h+k+l$ is even, thus limiting the number of detectable peaks [77].

A D2 Phaser in Bragg-Brentano geometry (Bruker Corp., Billerica, MA, USA) was used with a Cu X-ray tube (wavelength $\lambda_{\mathrm{K}_{\alpha 1}}$ =1.5406 Å). Both the source and the detector each rotate by an angle Θ, leading to the total angle of $2\,\Theta$ between incident and scattered radiation. A range of $2\,\Theta = 10 \ldots 145°$ was covered in the measurements. The step size was $2\,\Theta = 0.01°$, and the intensity at each step was measured for 384 s. The sample was rotated during the measurement to increase the surface area covered by the X-ray beam. The background intensity was subtracted using the device software. The scattering of $\mathrm{K}_{\alpha 1}$ and $\mathrm{K}_{\alpha 2}$ radiation, two different X-ray wavelengths due to different spin orientations, leads to two distinct peaks per lattice plane family. For the lattice parameter determination, the position of $\mathrm{K}_{\alpha 1}$ was used whenever the peaks could be differentiated.
According to Ref. [78], errors in interplanar distance determination arise, for example, from a vertical displacement of the sample from the X-ray focal point or from a not perfectly flat sample surface. Accordingly, the resulting lattice parameter values deviate from the actual value. Thus, the results for d_{hkl}, and as a consequence a, need to be compensated for these errors. They scale as $\propto \cot^2(\Theta)$ and $\propto \cos(\Theta)\cot(\Theta)$, respectively [78]. The average of both scalings was suggested in Ref. [77] as a correction function f_{corr} to account for these errors.

$$f_{\mathrm{corr}}(\Theta) = 0.5\, \left(\cot^2(\Theta) + \cos(\Theta)\, \cot(\Theta)\right) \tag{3.2}$$

The calculated lattice parameters of all identified peaks are weighted by their respective value of $f_{\mathrm{corr}}(\Theta)$. The resulting set of data points is linearly extrapolated to $f_{\mathrm{corr}} = 0$ (equivalent to $\Theta = 90°$), where both error contributions reach their minimal value [77]. The lattice parameter at $f_{\mathrm{corr}} = 0$ is then considered as the lattice parameter of the alloy.

3.7 Mechanical Testing

In order to unambiguously determine substitutional solid solution strengthening, the impact of other strengthening contributions needs to be evaluated and accounted for. A multiscale approach was used for mechanical characterization to address this complication, bridging from the nano- to the macroscopic scale:

(i) Nanoindentation (up to $\approx 1\,\mu m$ depth) performed in the centers of individual grains is unaffected by grain boundary effects, for example grain size dependent strength [8] or a strengthening by oxide particles, which preferably form at grain boundaries [79].

(ii) Vickers hardness (around $100\,\mu m$ depth) is measured over many grains, yielding an average hardness value for the material, including effects by grain boundaries. Vickers hardness is correlated to the 8% offset yield strength $\sigma_{p8\%}$ [80], which allows for a comparison to macroscopic testing.

(iii) Macroscopic compression testing averages the strength over many grain orientations, but is also affected by grain boundary effects. The yield strength necessary for solid solution strengthening modelling can be obtained (or approximated) by compression testing results.

Combining all measurement methods, the impact of superimposed strengthening contributions can be assessed. Solid solution strengthening can thus be isolated and compared to the model-compatible descriptions of solid solution strengthening to identify the mechanisms of plastic deformation.

3.7.1 Nanoindentation

In NI, a tip is pushed into the sample surface. Based on the recorded data for applied load and indentation depth, together with information on the tip shape, hardness and indentation modulus of the indented sample can be determined [81]. This sets NI apart from conventional indentation testing, e.g., Vickers hardness testing as described below, where no depth-dependent data are acquired. Accordingly, only the hardness can be extracted, and only after the completion of the indentation [82]. The principle of a nanoindentation measurement cycle is shown in Fig. 3.4 a) for a measurement in Mo-10Ti, where the applied load is shown as a function of contact time between tip and sample surface. The corresponding load-displacement data are shown in Fig. 3.4 b). Different segments of the measurement cycle are indicated by the grey dashed lines in a) and are marked by their numbers in b). In segment 1, when contact is made between tip and sample, load P is increased according to the equation $\dot{P}/P = 0.05\,\mathrm{s}^{-1}$, i.e., a constant strain rate is maintained [83], until the maximum possible load or the maximum indentation depth is reached. At maximum, segment 2, the load is held for 10 s to account for any potentially time-dependent deformation behavior of the sample [84]. In segment 3, the tip is retracted to 10% of the maximum load. The tip is held at this load for 100 s to record information on thermal drift of the sample-tip system [85]. Afterwards, the tip is retracted fully from the sample, Segment 5, and the tip is moved to the next indentation position.

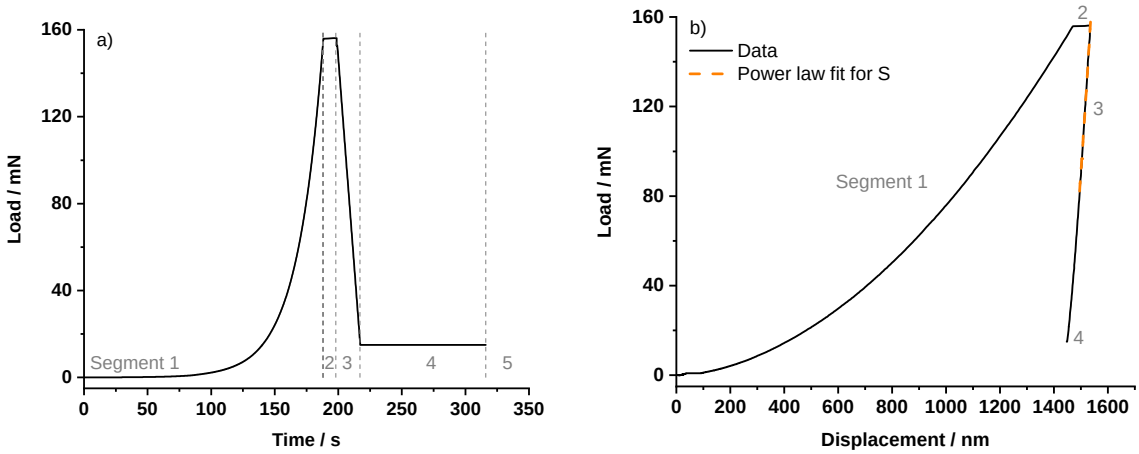

Figure 3.4: The measurement principle of nanoindentation, exemplary for an indent in Mo-10Ti. Load on the sample as a function of time in a) and the according load as a function of displacement data in b). The segments of an indentation cycle are marked with the grey dashed lines in a) and are explained in the body text. The grey numbers in b) indicate the same segments in the load-displacement data. Marked as orange dashed line in b) is a power law fit to the onset of unloading, after the transition from segment 2 to 3. The slope of this function can be used to calculate the contact stiffness S, which is required in the analysis after Oliver and Pharr [86, 87].

Using the tip area calibration, the projected contact area A can be determined based on the displacement data. Together with the applied load P, the nanohardness nH can be calculated as [81, 86]

$$nH = \frac{P}{A} \tag{3.3}$$

To determine the contact depth, the actual displacement into the sample, several processes need to be considered, which all lead to an overall change of measured tip displacement:

(i) An elastic deformation of the sample surface around the indentation, the so-called "sink-in".

(ii) The elastic deformation of the tip during indentation.

(iii) The elastic deformation of the device.

(iv) Elastic and plastic deformation of the sample below the indent.

These values will be determined following the analysis after Oliver and Pharr [86, 87]. While alternative analysis methods exist, for example a comparison of elastic and plastic deformation work [88, 89], the Oliver-Pharr method is the most established one and was used for all analyses here (assuming $\nu = 0.3$ for all alloys).
According to Ref. [86], the sink-in depth h_s can be estimated as

$$h_\mathrm{s} = 0.75\,\frac{P}{S} \tag{3.4}$$

where S is the contact stiffness, which will be explained below. The contact depth h_c is then the indentation depth minus the sink-in depth, $h_\mathrm{c} = h_\mathrm{ind} - h_\mathrm{s}$. The relevant quantities are schematically shown in Fig. 3.5.

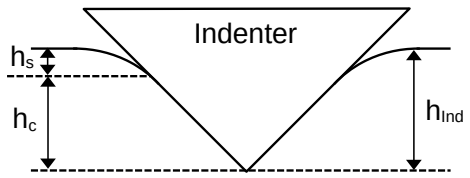

Figure 3.5: A sketch of the relevant dimensions used in NI: The indentation depth h_Ind as measured from the undistorted surface, the sink-in depth h_s as elastic deformation of the sample surface surrounding the indent and the actual contact depth h_c between indenter and sample.

The contact stiffness is defined in two ways, linking the experimental data to a theoretical description [86]. The experimental definition is using the derivative of the load-displacement data at the onset of unloading, i.e., immediately after the transition from segment 2 to 3 in Fig. 3.4 b) [86]:

$$S = (\mathrm{d}P/\mathrm{d}h)_{\text{at unloading}} \tag{3.5}$$

In the Oliver-Pharr analysis, segment 3 of the load-displacement data in Fig. 3.4 b) is fitted to a power law function. The corresponding fit is indicated as orange dashed

line in Fig. 3.4 b) and was found to be $P = 0.58\,\mathrm{mN/nm^{1.22}}\ (h - 1437\,\mathrm{nm})^{1.22}$ for this measurement. This calculates to $S = 1900\,\mathrm{kN/m}$ for the experimental contact stiffness. The theoretical description of S models the elastic contact of a Berkovich indenter and surface as [86]

$$\frac{1}{S} = \frac{\sqrt{\pi}}{2}\frac{1}{E_\mathrm{r}\sqrt{A}} + \frac{1}{S_\mathrm{device}} \tag{3.6}$$

where the compliance of the measurement setup, $1/S_\mathrm{device}$ is included. E_r, the reduced modulus combines the elastic properties of sample and tip [86] to

$$\frac{1}{E_\mathrm{red}} = \frac{1-\nu_\mathrm{tip}^2}{E_\mathrm{tip}} + \frac{1-\nu_\mathrm{sample}^2}{E_\mathrm{sample}} \tag{3.7}$$

with E_sample and ν_sample being the indentation modulus and Poisson's ratio of the sample, respectively. For the diamond tip, $E_\mathrm{tip} = 1141\,\mathrm{GPa}$ and $\nu_\mathrm{tip} = 0.07$ were used [87]. The tip area function and the frame stiffness are obtained via calibration measurements in a material with known mechanical properties [87]. Here, fused quartz with $E_\mathrm{FQ} = 74.4\,\mathrm{GPa}$, $\nu_\mathrm{FQ} = 0.17$ and $nH_\mathrm{FQ} = 10\,\mathrm{GPa}$ was used. The indentation modulus as determined in the Oliver-Pharr method assumes isotropic elastic properties of the indented material, which is not true in practical small scale experiments [90]. The value noted above for fused quartz is the value for the macroscopic Young's modulus, which has been suggested by Oliver and Pharr as substitute value for the theoretical indentation modulus [87]. In the discussion below, the indentation modulus data will also be compared to Young's modulus data of the alloys.
Based on the load-displacement data shown in Fig. 3.4 b), a single value is obtained for the contact stiffness S, at the transition from segment 2 to 3. Thus, all therefrom derived values can only be calculated precisely at that depth. This problem can be solved by using the continuous stiffness measurement method [86]. A small, vertical oscillation of the tip is superimposed on the load signal during the loading part of the indentation (segment 1 in Fig. 3.4 b)), see Fig. 3.6. During each of the oscillation cycles, unloading is performed, and a contact stiffness value can be calculated [91]. Using this depth-dependent contact stiffness data, depth-dependent hardness and modulus values can be calculated according to the method described above.

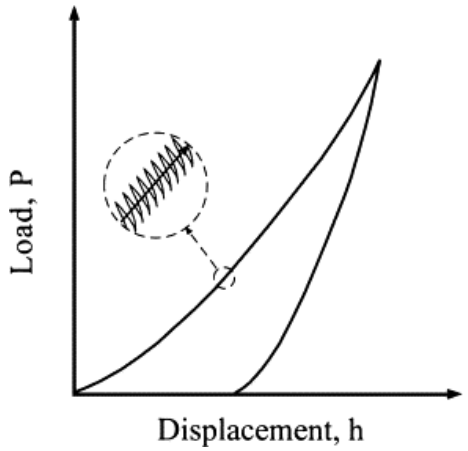

Figure 3.6: A sketch of the continuous stiffness measurement method. A small oscillation is superimposed on the load signal. During each oscillation cycle, unloading is performed, allowing to determine a contact stiffness S during each cycle. *Reproduced with permission from Ref. [91]*

NI measurements of Mo-Ti solid solutions were performed using a Nanoindenter XP (MTS, Eden Prairie, Minnesota, USA), while Mo-Nb solid solutions were measured using a FT-NMT04 (Femtotools, Buchs, Switzerland) mounted in a Supra 50VP SEM (Carl Zeiss AG, Oberkochen, Germany). Both devices used a diamond tip in Berkovich geometry. The tip area function and device compliance were calibrated using at least 10 indents in fused quartz to a depth of 2 µm. All samples were measured at room temperature and were indented to a maximum depth of 1.5 µm. A distance of at least 20 µm was kept between indents. This follows the suggestion of maintaining a distance of at least 10 times indentation depth between indents to avoid dislocation-dislocation interactions [92]. The same distance was also kept to grain boundaries to avoid grain boundary effects. Mo-Ti solid solutions containing $x_{\mathrm{Ti}} = 40\,\mathrm{at\%}$ and more showed a dendritic microstructure in the as-cast state, which can have an impact on the hardness detected in NI due to the small indentation depth. Thus, homogenized samples were tested, using the method described in Sec. 3.2.

At least 10 indents per sample were analyzed using the continuous stiffness measurement method. In the MTS nanoindenter, an oscillation amplitude and frequency of 2 nm and 45 Hz were used, in the Femtotools nanoindenter, 3 nm and a frequency of 200 Hz were used. For the MTS data, hardness and indentation modulus data were averaged between 1.1 and 1.3 µm. For the Femtotools data, hardness data were averaged from 1.2 to 1.4 µm depth, except for Mo-50Nb, where hardness data were averaged between 1 and 1.2 µm. The indentation modulus was averaged for all samples between 0.4 and 0.8 µm in the Femtotools indenter.

3.7.2 Vickers Hardness Testing

The Vickers hardness H_V of a material is defined in DIN6507 [82]. It is calculated as the load F_kgf with $[F_\mathrm{kgf}] = \mathrm{kgf}$, which is applied to a quadrilateral diamond pyramid indenter, divided by the projected surface area A_V of the indent left in the sample after indentation,

$$A_\mathrm{V} = \frac{d_\mathrm{avg}^2}{2\,\sin\left(\alpha_\mathrm{V}/2\right)} \tag{3.8}$$

where d_avg is the average length of the indent diagonals using $[d_\mathrm{avg}] = \mathrm{mm}$ and $\alpha_\mathrm{V} = 136°$ the angle between opposite faces of the Vickers pyramid. The Vickers hardness is then

$$\begin{aligned} H_\mathrm{V} &= \frac{F_\mathrm{kgf}}{A_\mathrm{V}} \\ &= \frac{2\,\sin\left(\alpha_\mathrm{V}/2\right)\,F_\mathrm{kgf}}{d_\mathrm{avg}^2} \\ &= 1.8544\,\frac{F_\mathrm{kgf}}{d_\mathrm{avg}^2} \end{aligned} \tag{3.9}$$

An exemplary Vickers indent is shown in Fig. 3.7 for the indentation of Nb.

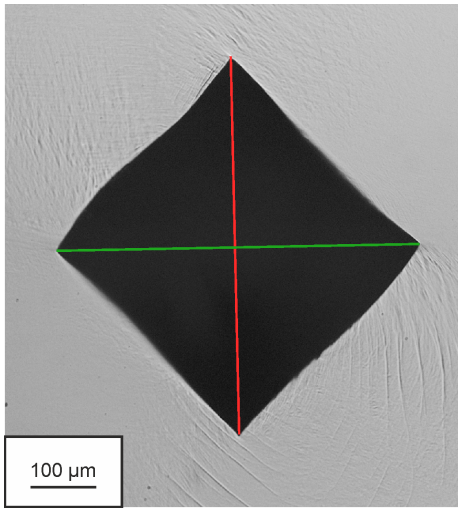

Figure 3.7: A Vickers indent in Nb, imaged in an optical microscope. The red vertical and green horizontal lines indicate the diagonals required for determining the Vickers hardness. With $d_\mathrm{horizontal} = 575\,\mu\mathrm{m}$ and $d_\mathrm{vertical} = 552\,\mu\mathrm{m}$, values of $H_\mathrm{V} = 58\,\mathrm{HV}$ and $H = 0.57\,\mathrm{GPa}$ are calculated.

When the load F_kgf is replaced by F_N with $[F_\mathrm{N}] = \mathrm{N}$ and d_avg is given using $[d_\mathrm{avg}] = \mathrm{m}$, the definition 3.9 then yields

$$H = 1.8544\,\frac{F_\mathrm{N}}{d_\mathrm{avg}^2} \tag{3.10}$$

where H is then the hardness in Pa. In the following, all hardness values denoted with H are always given in SI units.

For all Mo-Ti and Mo-Nb solid solutions, room temperature Vickers hardness measurements were performed according to DIN6507 on a QA10+ device (QATM, Mammelzen, Germany). A load of $F_\mathrm{N} = 10\,\mathrm{kg} \cdot g = 98\,\mathrm{N}$ was used with a holding time of 10 s at maximum load. Here, $g = 9.81\,\mathrm{m\,s^{-2}}$, gravitational acceleration, converts the load from kgf to N. A distance of three times the average diagonal was kept between indents and the sample boundary in agreement with Ref. [82]. The diagonals of at least ten indents per alloy were analyzed using the camera system of the device. For Nb, the indent diagonals were evaluated using a calibrated Leica Aristomet optical microscope (Ernst Leitz Wetzlar GmbH, Wetzlar, Germany; now Leica Microsystems), as the indents were larger than the field of view of the QA10+ camera system.

3.7.3 Compression Testing

Macroscopic compression testing was performed on a universal testing machine 1478 (ZwickRoell, Ulm, Germany) at room temperature. The cross-head speed was set to 0.03 mm/min to obtain an initial nominal strain rate of $\dot{\varepsilon} = 10^{-4}\,\mathrm{s^{-1}}$ for samples with an initial height of $l_0 \approx 5\,\mathrm{mm}$. The dimensions of each sample were measured three times with 1 µm resolution and averaged before testing using a digital indicator (Sylvac SA, Yverdon-les-Bains, Switzerland). The ground sample faces were coated with hexagonal BN to reduce friction between the faces and the punch contacts, which in turn reduces barrelling of the sample during compression testing. At least three compression tests per composition were analyzed. The displacement was measured using a capacitive sensor connected to the punch contacts. In contrast to a position measurement of the entire cross-head, the impact of device compliance on the displacement is thus minimized, and the measured displacement can be considered the actual change in sample height Δl. The engineering strain is then calculated as

$$\varepsilon_\mathrm{E} = \frac{|\Delta l|}{l_0} \tag{3.11}$$

In compression testing, displacements and strains are negative, as the final sample height is smaller than the initial one. For simplicity, the absolute value for the displacement and thus positive values for the strain are used throughout this work. Using the applied force F and the initial sample area A_0, the engineering stress σ_E is given as

$$\sigma_\mathrm{E} = \frac{F}{A_0} \tag{3.12}$$

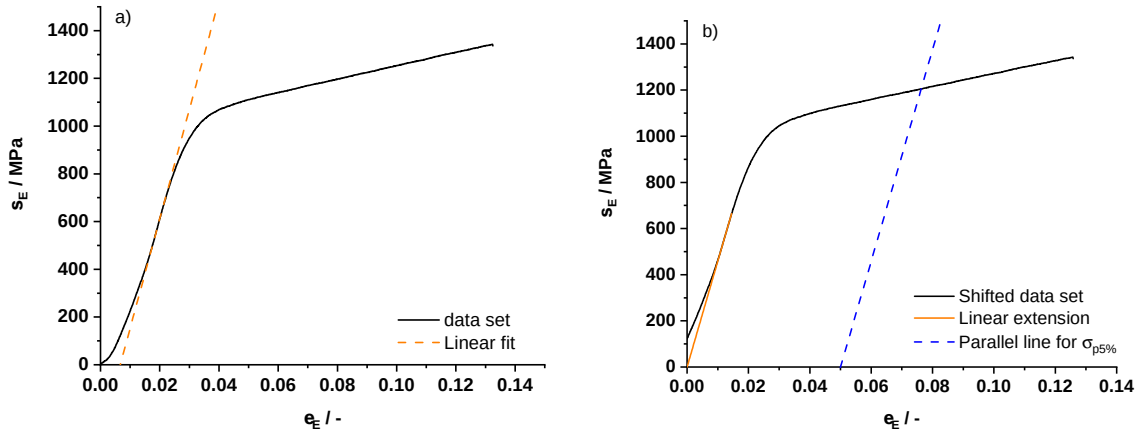

Figure 3.8: The analysis principle, which has been automated using MATLAB for this work, using a compression testing measurement of Mo-50Ti as example. a) The original engineering stress-strain data set (black solid line) and a linear function fit around the maximum slope (orange dashed line). b) Using the fit parameters from the linear fit, the non-linear initial part of the compression test data (black solid line) is replaced by the linear function (orange solid line), and this combined function is shifted to start in the origin. The blue dashed line indicates the 5% offset yield strength, using the slope of the linear function.

The resulting stress-strain data sets were evaluated automatically using a MATLAB script, the principle of which is shown in Fig. 3.8 for a measurement of Mo-50Ti. Imperfect alignment of sample faces and punch contacts as well as the application of a $\approx 50\,\mathrm{N}$ pre-measurement force lead to a non-linear initial slope of the stress-strain data set. To correct for these deviations, the data set is extrapolated and shifted horizontally towards the origin. A linear function is fitted to a small region around the largest slope of the stress-strain data set (orange dashed and black solid lines in Fig. 3.8 a). The linear function fit and the original data set are then combined by replacing the initial non-linear slope part of the stress-strain data set with the linear function (orange and black solid lines in Fig. 3.8 b). The combined curve is then shifted horizontally into the origin.
The slope of the linear fit, the "modulus of compression", is then used to determine the respective offset yield strength values, shown for $\sigma_{\mathrm{p5\%}}$ in Fig. 3.8 b) as blue dashed line with an value of $\sigma_{\mathrm{p5\%}} = 1205\,\mathrm{MPa}$. This automated approach allows to analyze a larger number of data sets in a short time compared to a manual analysis, especially when more than one value, e.g., 0.2% and 5% offset yield strength, need to be extracted. While this approach reduces human bias during the analysis, errors like device malfunctions might go undetected. Thus, intermediate analysis steps were exported as graphs and inspected. All data sets analyzed this way are compiled in Sec. 7.1 for the measurements used in this work.
As a distinct yield point was not observed in any sample, the 0.2% offset yield strength $\sigma_{\mathrm{p0.2\%}}$ was determined for all alloys as comparison value for the modelled yield strength σ_{y} in Secs 5.3 to 5.5.3. $\sigma_{\mathrm{p5\%}}$ was determined for all alloys to correlate compression and Vickers hardness testing, see Sec. 4.7.3. The suggested value of $\sigma_{\mathrm{p8\%}}$ [80] was not reached in some alloys due to intergranular fracture, thus $\sigma_{\mathrm{p5\%}}$ was used instead.

4 Experimental Results and Discussion

In this chapter, the experimental results will be presented and discussed. First, the quality of the synthesized alloys needs to be evaluated with respect to the microstructure and crystal structure as well as the alloy compositions including interstitial contaminations. The lattice parameter and indentation modulus will be discussed in detail as these values are required for the modelling of solid solution strengthening. The last section describes the mechanical properties obtained from nanoindentation, Vickers hardness testing and compression testing; including a correlation analysis to estimate the impact of other strengthening contributions besides solid solution strengthening.

4.1 Microstructure

Representative microstructures of all solid solutions are shown in Figs. 4.1 for Mo-Nb and 4.2 for Mo-Ti solid solutions. In these figures as well as throughout the chapter, all results for Mo-Nb solid solutions are indicated in orange colors, all results for Mo-Ti are indicated in blue. For solid solutions with at least 40 at% Ti, the microstructures after HT are shown. All Mo-Ti solid solutions show consistently a large grain size of at least 200 µm, which increased during homogenization treatment. The grain size of Mo-Nb solid solutions appears generally higher than the one for Mo-Ti, but was not quantified. Some alloys showed minor pore formation from casting, visible as black spots in Figs. 4.1 and 4.2. The white spots in high-Ti solid solutions in Fig. 4.2 were found to be La_2O_3 particles where the origin could not be identified. While La_2O_3 is typically added to W arc melting electrodes, the arc melter used for the synthesis works with a pure W electrode. Thus, the particles were likely already contained in the raw material.

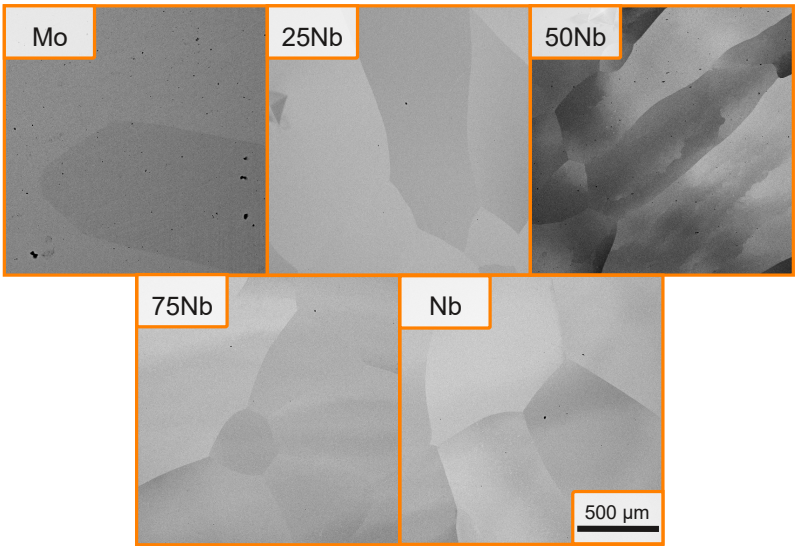

Figure 4.1: BSE images of the microstructures of Mo-Nb solid solutions. The scale bar is for all images. For all samples, a large grain size was obtained. Some pores from the casting process can be seen as black spots.

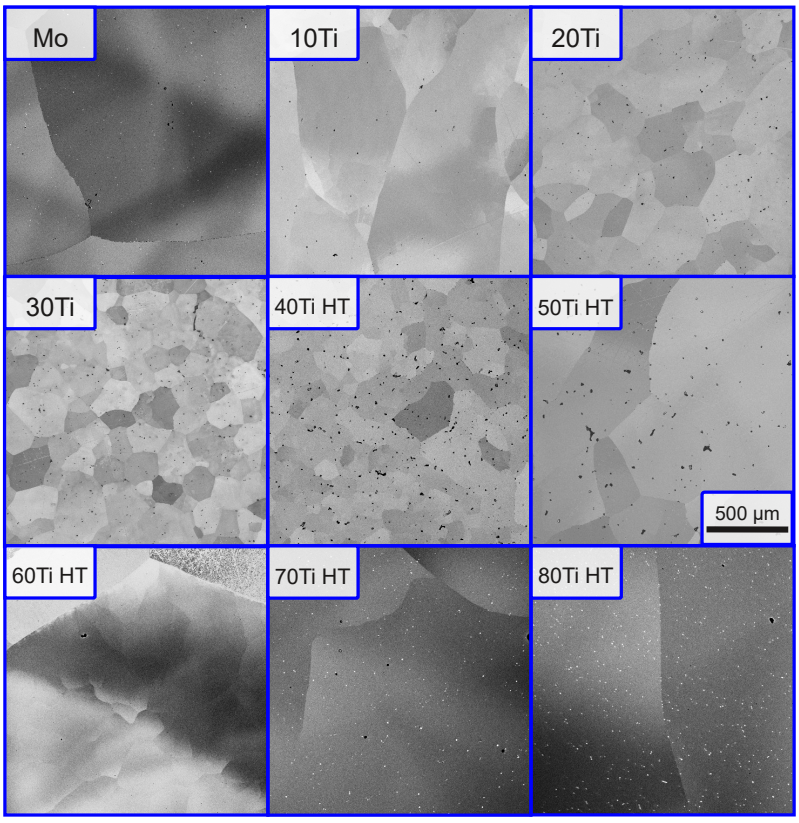

Figure 4.2: BSE images of the microstructures of Mo-Ti solid solutions. The scale bar is for all images. Alloys with at least 40 at% Ti are shown after HT. For all samples, a large grain size was obtained. The dark spots are pores formed during the casting process, while for high-Ti solid solutions, La_2O_3 particles were found in the alloys, which show as bright spots in the images.

4.2 Crystal Structure

All X-ray diffraction patterns revealed a BCC structure (Strukturbericht A2, W prototype, space group no. 229), see Fig. 4.3 a) for Mo-Ti solid solutions and 4.3 b) for Mo-Nb solid solutions. All intensities are normalized to the maximum value of the respective measurement. The graphs are offset vertically with increasing solute content for better visibility. The small peak observed at $2\Theta \approx 35°$ is the (110)-peak from Cu K_β radiation due to incomplete monochromatization. The peaks that are allowed according to the structure factor selection rules are indicated at the top of each graph. In Mo-Nb solid solutions, Fig. 4.3 b), fewer peaks were observed than in Mo-Ti solid solutions (Fig. 4.3 a)). As the probed total area is identical in all measurements, fewer grains are probed in samples with larger grain size, leading to fewer observed diffraction peaks. The varying intensity of the peaks also results from the large grain size. Depending on the area fraction probed per grain orientation by the X-ray beam, the intensity of the respective peak varies. The (222)-peak was not observed in the Mo-Nb solid solutions. The slight shift of the peaks towards smaller diffraction angles with increasing solute content is a result of the increasing lattice parameter, see Eq. 3.1. All solid solutions show peaks consistent with single-phase BCC structures.

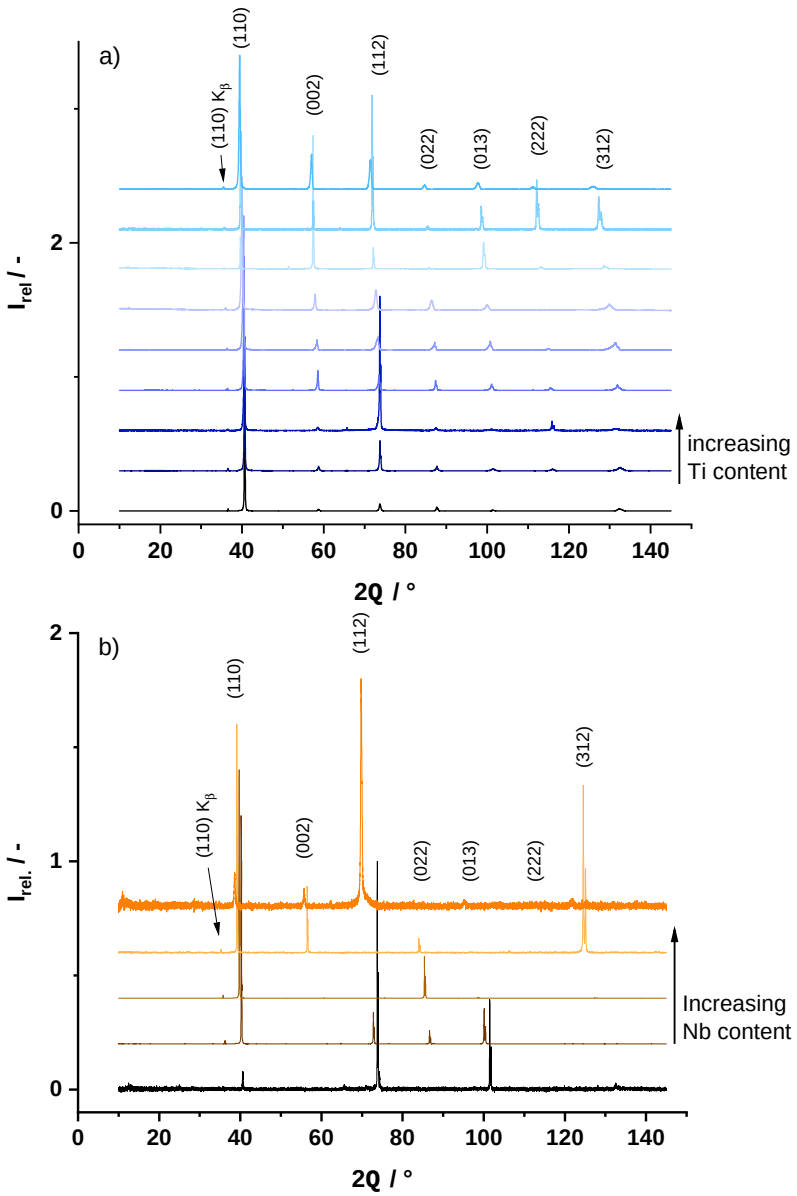

Figure 4.3: The diffraction patterns for a) the Mo-Ti (blue) and b) the Mo-Nb (orange) solid solutions. Solid solutions with increasing solute content are offset vertically. The peaks that are allowed according to the structure factor are indicated at the top. The arrow denoted with (110)K_β indicates the (110)-peak position due to scattering of Cu K_β radiation. All alloys showed a single-phase BCC structure and increasing lattice parameter with increasing solute content.

For Mo-Nb solid solutions, only a fully miscible BCC phase has been reported [93]. For Mo-Ti, the equilibrium phase diagram, Fig. 4.4, shows a miscibility gap and a monotectoid reaction in the range of studied Mo-Ti solid solutions [94]. Necessary annealing durations to achieve equilibrium were for example 650 h at 600 °C [95] or 120 h at 750 °C [96]. Here, due to the fast cooling rates in the water-cooled Cu crucible after arc melting as well as after HT during furnace cooling, no indications for either of the two reactions were observed. This agrees with earlier reports on arc melted Mo-Ti alloys [97]. Additionally, martensitic transformation and the formation of ω phase have been reported [94]. However, they were not observed in the solid solutions studied here, consistent with reported concentration limits of $x_{\mathrm{Mo,mart}} < 6\,\mathrm{at\%}$ [98] and $x_{\mathrm{Mo},\omega} < 15\,\mathrm{at\%}$ [99].

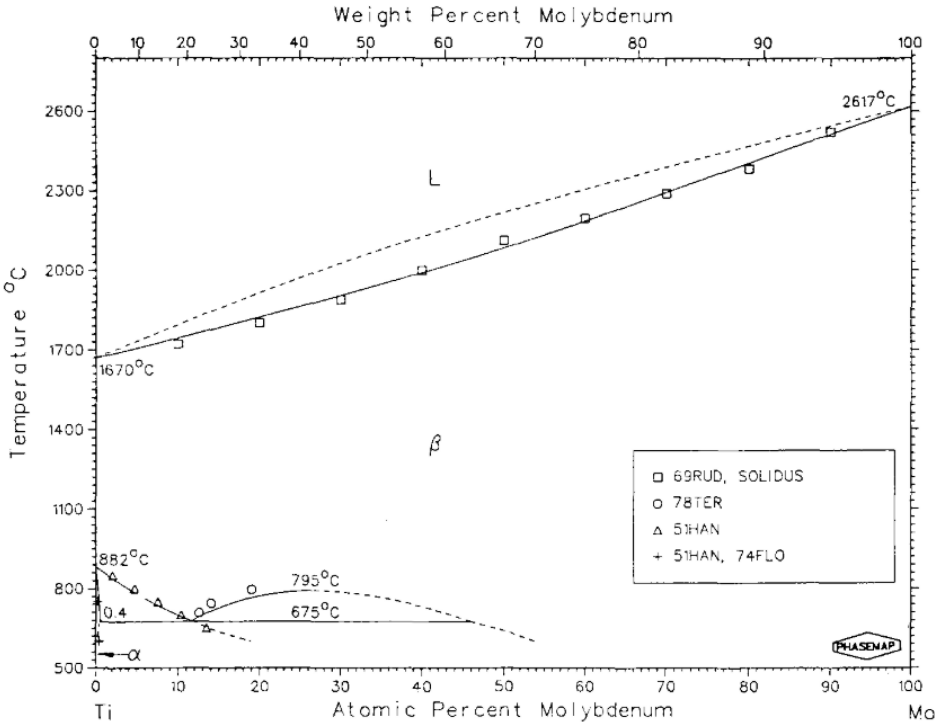

Figure 4.4: The Ti-Mo phase diagram. Note that the horizontal axis denotes increasing Mo content. α indicates the hexagonally-closed packed (HCP), β the BCC solid solutions. Data from Refs. [95] (Triangles, crosses), [96] (circles), [100] (squares) and [101] (crosses) were considered. All alloys up to 80 at% Ti showed a single-phase BCC structure due to fast cooling, contrary to the predicted phase separation at high Ti contents. *Reproduced with permission from Ref. [94].*

The Pearson correlation coefficient was determined for Mo-10Ti and Mo-80Ti via APT to determine if Mo and Ti are distributed randomly. The value for Ti remained almost constant between Mo-10Ti and Mo-80Ti with 0.02 and 0.03, respectively. The coefficient of Mo increased from 0.02 to 0.15. Still, both values are close to zero and thus indicate a random distribution. An additional nearest-neighbor analysis in Mo-80Ti revealed a slightly smaller average distance between Mo atoms than in randomized data, $(658 \pm 3)\,\mathrm{pm}$ compared to $(673 \pm 2)\,\mathrm{pm}$. While this might be a first indication of beginning ordering of Mo, the shift is not sufficient to perform a meaningful cluster analysis. Thus, both Mo and Ti can be considered randomly distributed in the investigated alloy.

4.3 Composition

4.3.1 Substitutional Element Contents

All Mo-Ti and Mo-Nb solid solutions showed good agreement between the compositional analysis by EDS measurements and the desired composition, as can be seen in Tab. 4.1. For Mo-Ti, the largest deviation between desired composition and EDS was detected in Mo-40Ti with 1.5 at%. A reference measurement by ICP-OES yielded 28.5 at% Ti in Mo-30Ti compared to 29 at% Ti determined by EDS. In APT, the Mo-10Ti sample revealed an average Ti content of 10.1 at% after peak deconvolution, which confirms the EDS results for this sample of 9.4 at% within the resolutions of the techniques. The APT analysis of Mo-80Ti revealed a slightly lower Ti content after peak deconvolution (76.5 at%) than in the EDS measurements.
In Mo-Nb, EDS analyses resulted in consistently about 2-3 at% higher Nb contents than the desired compositions for all solid solutions. However, a reference measurement by ICP-OES revealed 49.8 at% Nb compared to the EDS average of 52.9 at% for Mo-50Nb. This difference is probably due to an inaccurate estimate of the ZAF factor, which corrects for atomic number (Z), absorption (A) and fluorescence (F) effects, in the software for two neighboring elements of the periodic table of elements. Detailed results of all compositional analyses are found in Tab. 4.1.

Table 4.1: Chemical composition of the Mo alloys studied. For both alloy systems, EDS, ICP-OES and HCGE data is presented. For Mo-Ti, additional data was obtained using APT. Balance is Mo. Values marked with [a] were below detection limit. Errors in APT measurements are below the given decimal places and therefore omitted. For EDS, a conservative estimate of error is given based on the maximum observed error among all measurements.

desired	x_{Ti}/at%			x_O / at-ppm		x_N / at-ppm	
x_{Ti}/at%	EDS	ICP-OES	APT	HCGE	APT	HCGE	APT
0	-	-	-	965 ± 296	-	-	-
10	9.4 ± 0.5	-	10.1	496 ± 0[a]	0[a]	104 ± 0[a]	0[a]
20	19.6 ± 0.5	-	-	955 ± 577	-	123 ± 44	-
30	29.0 ± 0.5	28.5 ± 1.3	-	617 ± 113	-	111 ± 41	-
40	38.5 ± 0.5	-	-	959 ± 187	-	137 ± 59	-
50	50.0 ± 0.5	-	-	1232 ± 372	-	113 ± 10	-
60	60.3 ± 0.5	-	-	3268 ± 690	-	110 ± 36	-
70	70.0 ± 0.5	-	-	4316 ± 924	-	133 ± 42	-
80	80.0 ± 0.5	-	76.5	3626 ± 787	3300	185 ± 58	< 100
x_{Nb}/at%	x_{Nb}/at%			x_O / at-ppm		x_N / at-ppm	
0	-	-	-	360 ± 0[a]	-	102 ± 0[a]	-
25	26.7 ± 0.5	-	-	357 ± 0[a]	-	102 ± 0[a]	-
50	52.9 ± 0.5	49.8 ± 1.4	-	354 ± 0[a]	-	101 ± 0[a]	-
75	77.4 ± 0.5	-	-	351 ± 0[a]	-	100 ± 0[a]	-
100	-	-	-	575 ± 125	-	239 ± 80	-

4.3.2 Interstitial Element Contents

The Mo-Ti alloys show a significant increase in O content with increasing Ti content, see Tab. 4.1. Samples up to $x_{\mathrm{Ti}} = 50\,\mathrm{at\%}$ contained O of up to 0.1 at%; for higher Ti the O contents increased strongly to at least 0.3 at% O. In Mo-10Ti, the results for O were below the detection limit of 0.05 at%. N content was below 0.02 at% for all alloys. The Mo-Nb alloys showed O contents below the detection limit of 0.04 at%, except for Nb, where 0.06 at% O was detected. Similarly, N content was below 0.01 at% for all Mo-Nb alloys except Nb, where 0.02 at% N was detected. Both O and N data are listed in detail in Tab. 4.1. The O data are also presented in Fig. 4.5. These data correlate well with the O contents of the raw materials, which are also included in Fig. 4.5, where 0.02, 0.08 and 0.31 at% O were found for Mo, Nb and Ti, respectively. N contents were below 0.02 at% in the raw materials. The impact of the low N contents will not be considered further.

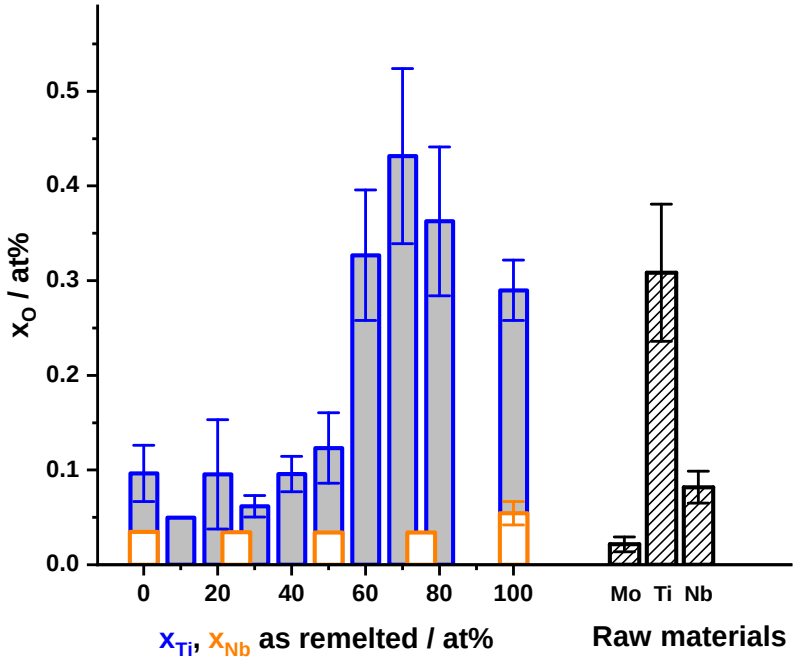

Figure 4.5: O contents of remelted alloys and raw materials. Mo-Ti solid solutions are shown as blue columns, Mo-Nb solid solutions as orange columns. The raw material analyses are shown as black columns. O content of columns without error bars were smaller than the detection limit, so this limit is shown as upper limit of O content. The Mo-Ti solid solutions show a significant increase in O content for concentrations of at least 60 at% Ti compared to lower Ti concentrations, which is consistent with the concentrations found in raw and remelted Ti. Mo-Nb solid solutions showed consistently low O contents below the detection limit.

Results acquired in APT are consistent with the data acquired by HCGE. In Mo-10Ti no significant O content was detected within the detection limits. In Mo-80Ti, an O content of 0.33 at% was determined. Due to the large number of ions detected, the statistical error is by several orders of magnitude smaller than the indicated two decimal places and therefore omitted. This is consistent with the HCGE value of (0.36±0.07) at% O. As the tips for APT were extracted from grain centers, the entire O, within the margins of error, is found dissolved in the grains. The impact of the detected La_2O_3 particles on the detected O content is thus small.

Mo does not dissolve significant amounts of O. Ref. [102] for example reports 4 at-ppm at 1700 °C. By contrast, Ti dissolves up to 33 at% O in the HCP phase and up to 8 at% in the BCC phase at around 1700 °C [103]. Thus, an increase of O solubility in Mo-Ti solid solutions is expected for increasing Ti content. Comparison data is scarce in literature; diffusion experiments in Ti-rich alloys yielded 2 at% O in BCC grains with 16 at% Mo, while the HCP matrix contained up to 19 at% O [104]. One model describes a qualitative correlation between the number of valence electrons per atom, e_A, and interstitial solubility of O for refractory metals and solid solutions [105]. When a threshold of $e_A = 5.7$ is exceeded, no dissolved O is detected. While later data contradict the determined O solubility values [106], models based on the electron density of states confirm the threshold [107, 108]. The APT results for Mo-10Ti and Mo-80Ti also agree with the suggested threshold; Assuming six and four valence electrons per atom for Mo and Ti [109], the electron per atom ratios are $(e_A)_{\text{Mo-10Ti}} = 5.8$ and $(e_A)_{\text{Mo-80Ti}} = 4.4$.

HCGE of raw Ti revealed an O content of 0.30±0.07 at% O, which is similar to the values found in Ti-rich Mo-Ti solid solutions. For reference, Ti was remelted and 0.29±0.03 at% O was found here as well. For raw Mo supplied by EvoChem, HCGE yielded a large range of O contents depending on the lot. Values between 0.02 at% and 0.72 at% were found, which indicates quality problems of the raw Mo. The unintentional incorporation of La_2O_3 in varying amounts in the raw Mo might contribute to the range of O contents detected. Albeit Mo from a lot with a detected amount of 0.02 at% O was used for the synthesis of the Ti-rich Mo-Ti solid solutions, it cannot be ruled out that the raw Mo is the source of the La_2O_3 as the distribution of La_2O_3 in the Mo foil is unknown. Consequently, the raw Mo might also contribute to the global O contents in high-Ti solid solutions The lot used for the solid solutions up to Mo-50Ti was not analyzed. For Mo-Nb solid solutions, Mo supplied by Plansee was used, where HCGE revealed an O content of ≤0.02 at%. Raw Nb contained 0.08 at% O, remelted Nb 0.05 at% O. In line with the low O contents of the raw and remelted elements, O content in the Mo-Nb solid solutions was ≤0.04 at%, below the detection limit.

Nb can dissolve up to 5 at% O at 1700 °C [110], which is similar to the value for BCC Ti. Therefore, an increase in O solubility is also expected for Mo-Nb solid solutions with increasing Nb content. The e_A-threshold proposed in Ref. [105] is reached at $x_{Nb} = 30$ at%. However, the Mo-50Nb and Mo-75Nb solid solutions do not show an O content above the detection limit. The combined results of the Mo-Ti and Mo-Nb alloys indicate that the arc melting process does not contribute significantly to the O content of the alloys, but the interstitial content of the raw materials is the main source for interstitial contamination of the remelted alloys.

4.4 Lattice Parameter

The lattice parameters for Mo-Ti and Mo-Nb are presented in Fig. 4.6, with Mo-Ti data as blue triangles and Mo-Nb as orange diamonds. For both solid solution series, good agreement with literature data is found (grey symbols, taken from Refs. [95, 100] for Mo-Ti and Refs. [111, 112] for Mo-Nb). The experimental lattice parameter of Nb, 3.30 Å, and the extrapolated value for BCC Ti, 3.28 Å, are similar. However, while the lattice parameters of Mo-Nb solid solutions change only with a small deviation from a linear rule-of-mixture, the lattice parameters of Mo-Ti solid solutions increase strongly non-linearly as a function of composition: The lattice parameter remains almost constant up to around Mo-20Ti. Between 30 at% and 50 at%, the curvature changes strongly and, for higher Ti contents, an almost linear increase of lattice parameter is observed. The same trend is also found in W-Ti solid solutions [113].

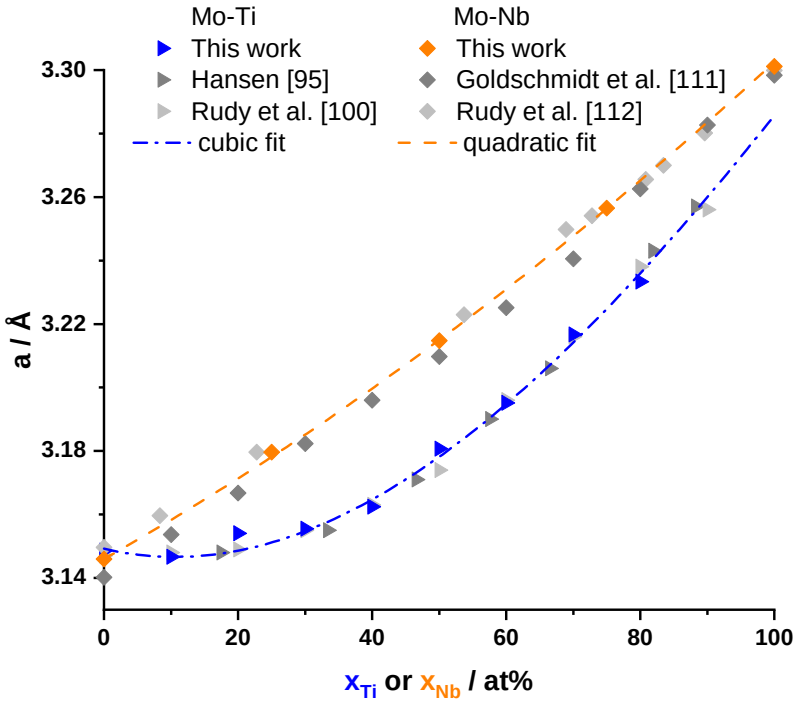

Figure 4.6: Results for the lattice parameter measurements of Mo-Ti (blue triangles) and Mo-Nb (orange diamonds) solid solutions. For each system, literature data are given as grey symbols of the same shape [95, 100, 111, 112]. The fits used in solid solution strengthening modelling are shown as dashed lines. A good agreement with literature data is obtained. A quadratic fit can describe the lattice parameter values of Mo-Nb solid solutions, while a cubic fit is necessary to capture the non-linearity of Mo-Ti solid solution lattice parameters.

For the modelling of solid solution strengthening, polynomial functions are fitted to the data of the lattice parameter. For Mo-Nb, a second order polynomial was used. Due to the strong non-linearity of Mo-Ti, a third order polynomial was fitted for this system. The results for both fits are also presented in Fig. 4.6 as dashed lines and the corresponding functions for the lattice parameter a are:

$$a_{\text{Mo-Ti}} = (-0.0572\, x_{\text{Ti}}^3 + 0.2430\, x_{\text{Ti}}^2 - 0.0493\, x_{\text{Ti}} + 3.1492)\,\text{Å} \tag{4.1}$$

$$a_{\text{Mo-Nb}} = (0.0373\, x_{\text{Nb}}^2 + 0.1192\, x_{\text{Nb}} + 3.1460)\,\text{Å} \tag{4.2}$$

with x being the atomic concentrations of Ti and Nb, respectively. Both fits correlate very well to the experimental data with $R^2_{\text{adj}} = 0.996$ for Mo-Ti and $R^2_{\text{adj}} = 0.999$ for Mo-Nb, respectively. According to the fit function for Mo-Ti, the lattice parameter for Mo is larger than for Mo-10Ti and than the experimental results. This is a modelling artefact; due to the almost constant lattice parameter at low Ti contents, the local minimum of the cubic function is fitted to approximate this plateau. This results in the slight increase of the lattice parameter for Mo compared to the minimum value. However, this artefact would impact only the modelling of dilute solid solutions, which are not the focus of this work.

4.5 Misfit Parameter

The Fleischer [48] and Labusch [35] models use the Fleischer misfit parameter $\delta_{\text{F}} = \frac{1}{a}\frac{\text{d}a}{\text{d}x}$ to quantify the lattice strain due to differently sized solutes in a solid solution. Using the polynomial fits in Eq. 4.1, the misfit values can thus be calculated for both systems (see Fig. 4.7 a). The misfit of Ti-lean solid solutions is negative, $\delta_{\text{F,Mo}} = -0.015$ for the smallest Ti concentrations, due to the decrease in lattice parameter modelled by Eq. 4.1. It increases monotonously and reaches approximately $\delta_{\text{F}} = 0.07$ for Mo-80Ti with the axis intercept, $\delta_{\text{F}} = 0$, at approximately Mo-10Ti. The misfit of Mo-Nb solid solution remains almost constant, rising from approximately 0.04 to 0.05 from Mo to Nb. This corresponds to the almost linear increase in lattice parameter with increasing Nb content.

The Maresca-Curtin model [11] for edge dislocation strengthening includes a volumetric misfit parameter due to different atomic volumes. In a binary system, this parameter can be calculated similar to the Fleischer parameter. According to Eq. 2.34, $\delta = \sqrt{x \cdot (1-x)}\,\frac{1}{a}\frac{\text{d}a}{\text{d}x}$. The resulting misfit values for Mo-Ti and Mo-Nb are presented in Fig. 4.7 b. Due to the factor $\sqrt{x \cdot (1-x)}$, the misfit values are 0 in pure metals. For Mo-Ti solid solutions, $\delta = 0$ is again modelled for Mo-10Ti with a small concave part between 0 and 10 at% Ti, which is due to the modelling artefact of the lattice parameter fit function. The maximum value of the misfit is reached at Mo-72Ti with 0.03 and decreases again for higher Ti contents.
The Mo-Nb solid solutions show an almost symmetrical misfit, peaking at Mo-60Nb with 0.025. While the term $\sqrt{x \cdot (1-x)}$ is symmetrical around 50 at%, the small increase of δ_{F} with increasing Nb content results in a peak shift towards Nb-rich solid solutions.

A correlation analysis between Vickers hardness data from Ref. [41] and the edge dislocation strengthening model revealed a threshold value $\delta_{\mathrm{th}} = 0.035$, where alloy strength is expected to be controlled by edge dislocation motion, which is included in Fig. 4.7 b) as black dashed line. No similar considerations have been made for the Fleischer misfit. In the latter, the strengthening for both dislocation types is included via the weighting factor α.

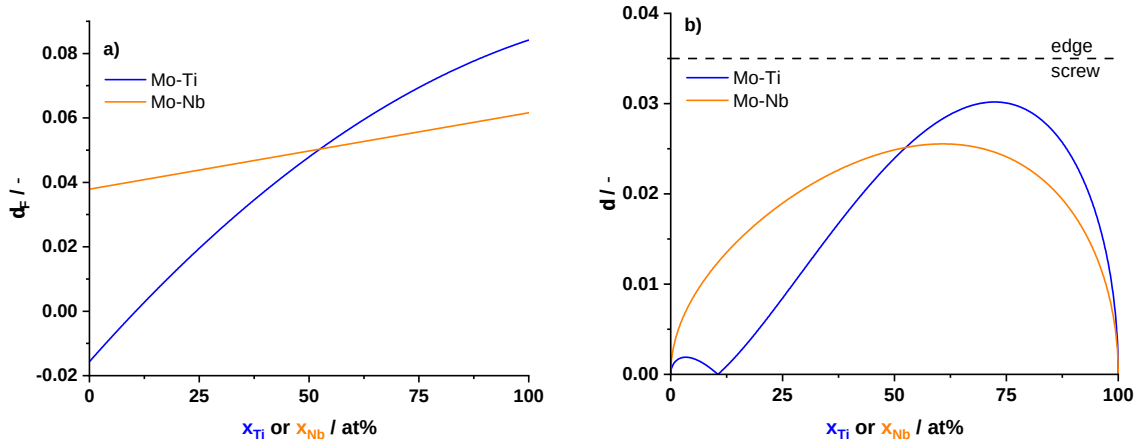

Figure 4.7: The misfit parameter after Fleischer [48] in a) used in the Fleischer [48] and Labusch [35] models and the misfit parameter after Varvenne [61] used in the Maresca-Curtin [11] model in b). The black dashed line in b) presents an estimated misfit threshold, above which edge dislocation motion controls alloy strength. There is no similar threshold available for the Fleischer misfit.

The Ti-rich Mo-Ti solid solutions show a large misfit, with a maximum of 0.030 or 85% of the proposed threshold; thus the strength by edge dislocations might be of a similar fraction compared to the strength based on screw dislocation motion. However, these alloys are still below the threshold, so screw dislocation-controlled strength is expected. Also for Mo-Nb solid solutions, with misfits up to 0.025, and the Ti-lean Mo-Ti solid solutions, where the misfit is close to 0, screw dislocations are expected to control the strength.

4.6 Indentation Modulus

Indentation modulus data were obtained for all solid solutions and the results are shown in Fig. 4.8. Mo-Ti solid solutions are shown as blue symbols, Mo-Nb solid solutions as orange symbols. Measurement errors smaller than their respective symbol size were omitted. Note that the horizontal axis is flipped for Mo-Nb for better visibility. The moduli of both solid solution series decrease approximately linearly with increasing Ti or Nb content, ranging from $E_{\text{Mo-0Ti,exp}} = (332 \pm 3)\,\text{GPa}$ to $E_{\text{Mo-80Ti,exp}} = (130 \pm 1)\,\text{GPa}$, and from $E_{\text{Mo-0Nb,exp}} = (348 \pm 9)\,\text{GPa}$ to $E_{\text{Nb,exp}} = (115 \pm 2)\,\text{GPa}$. For comparison, Young's modulus data for Nb and Mo have been reported as $E_{\text{Nb,lit}} = 106\,\text{GPa}$ [114] and $E_{\text{Mo,lit}} = 330\,\text{GPa}$ [115], respectively. The latter values are close, but slightly lower than the moduli obtained in NI. For concentrated solid solutions, deviations from the linear decrease become apparent; compared to the respective linear trends in both systems, Mo-40Ti and Mo-50Ti show moduli slightly below the linear trend, while Mo-50Nb exhibits a modulus value that is too high.

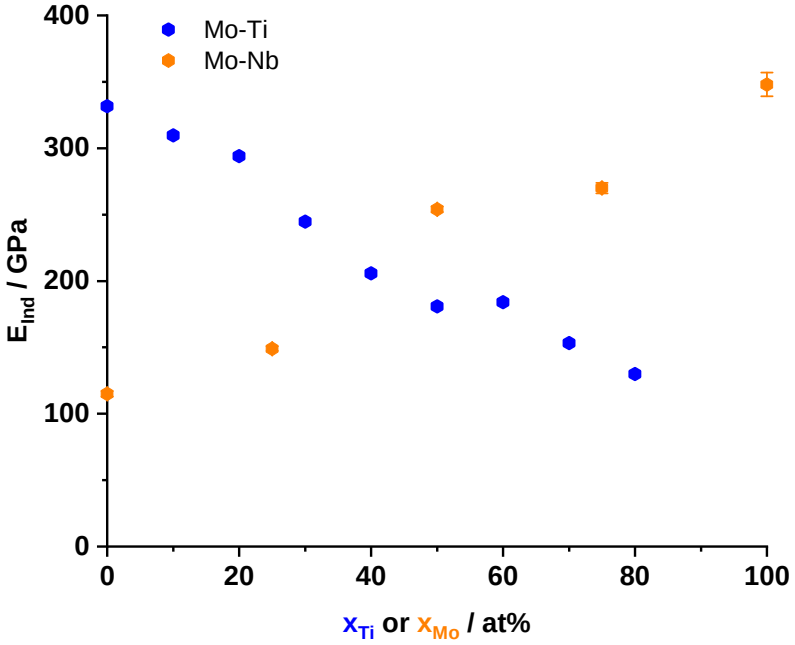

Figure 4.8: Indentation modulus data E_{Ind} for Mo-Ti (blue) and Mo-Nb (orange). Note that the horizontal axis is flipped for Mo-Nb compared to the normal depiction for better visibility. Error bars smaller than the symbol size were omitted. An approximately linear decrease is detected for both solid solution series with decreasing Mo content.

4.7 Mechanical Properties

4.7.1 Hardness

Results of Vickers hardness testing and nanohardness measurements are presented in Fig 4.9 for Mo-Ti solid solutions. Vickers hardness data are shown as blue squares, nanohardness as blue triangles. Values for Mo were determined as $H_{\text{Mo, Mo-Ti}} = 1.8\,\text{GPa}$ and $nH_{\text{Mo, Mo-Ti}} = (3.2 \pm 0.1)\,\text{GPa}$. Values in this section without given error showed standard deviation values smaller than the number of significant decimal places. Both data sets show an increase in hardness with increasing Ti content, with a slight convexity at low Ti contents. The peak in hardness is reached at 30 or 40 at% Ti for both data sets, where both compositions show similar hardness values (within the experimental errors) with $H_{\text{peak}} = (4.1 \pm 0.1)\,\text{GPa}$ for both alloys or $nH_{\text{Mo-30Ti}} = (5.8 \pm 0.2)\,\text{GPa}$ and $nH_{\text{Mo-40Ti}} = (5.7 \pm 0.2)\,\text{GPa}$. For higher Ti contents, both data sets decrease approximately linearly. Mo-50Ti shows a nanohardness slightly smaller than the linear trend of other high-Ti solid solutions. At 80 at% Ti, values of $H_{\text{Mo-80Ti}} = 2.7\,\text{GPa}$ and $nH_{\text{Mo-80Ti}} = 4.1\,\text{GPa}$ are obtained. In Fig. 4.9, Vickers hardness data from literature [41] are also included as grey squares. These values are uniformly higher than the values measured in this work. As the interstitial contamination of the alloys was not reported in Ref. [41], a higher interstitial content might lead to the difference in hardness values.

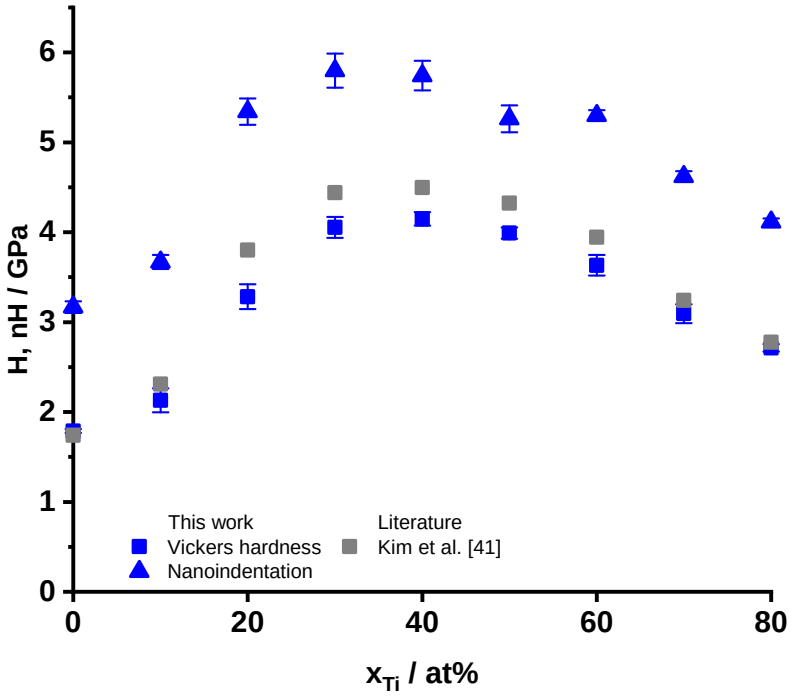

Figure 4.9: Vickers hardness (squares) and nanohardness (triangles) for Mo-Ti solid solutions (blue symbols). Error bars indicate the standard deviation of measurements. The grey symbols are taken from Ref. [41]. The maximum in hardness and nanohardness is detected for 30 or 40 at% Ti, where the values are similar.

The hardness and nanohardness data for Mo-Nb solid solutions are presented in Fig. 4.10 as orange symbols, with Vickers hardness data shown as squares and nanoindentation data as triangles. The hardness of this Mo sample shows good agreement with the value of the one measured for the Mo-Ti solid solution series with $H_{\text{Mo, Mo-Nb}} = 1.7\,\text{GPa}$. Nanohardness, however, is slightly smaller with $nH_{\text{Mo, Mo-Nb}} = 2.9\,\text{GPa}$. Both data sets increase with increasing Nb content and the maximum is reached for Mo-50Nb with $H_{\text{peak}} = (3.9 \pm 0.1)\,\text{GPa}$ and $nH_{\text{peak}} = (5.3 \pm 0.1)\,\text{GPa}$. The values decrease with larger Nb contents, until $H_{\text{Nb}} = 0.6\,\text{GPa}$ and $nH_{\text{Nb}} = 1.1\,\text{GPa}$ are reached. Vickers hardness data from literature [41] indicates an almost linear increase with increasing Nb content until the peak at 50 at% is reached, followed by an approximately linear decrease with steeper slope for larger Nb contents. Similar to the data for Mo-Ti solid solutions, the literature values are uniformly higher.

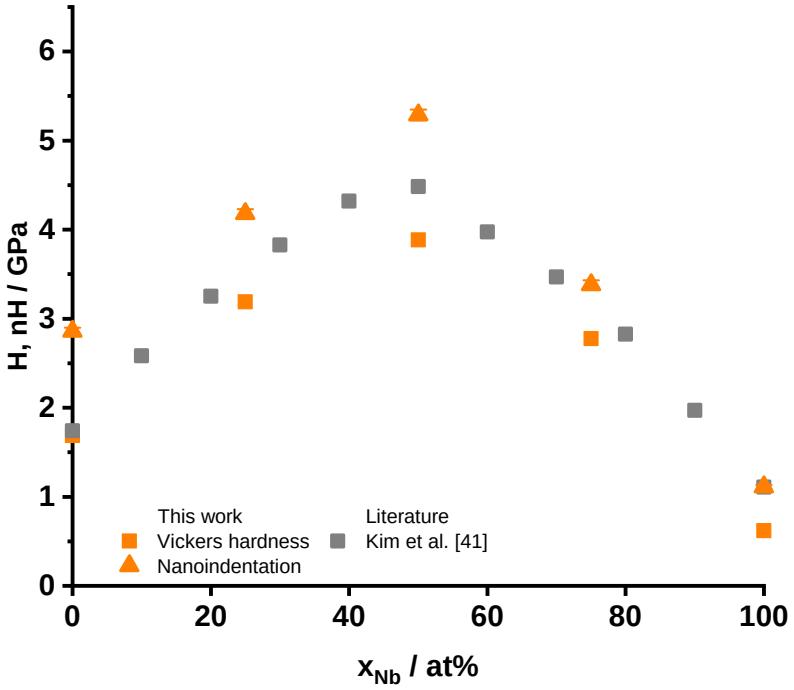

Figure 4.10: Vickers hardness (squares) and nanohardness (triangles) for Mo-Nb solid solutions (orange symbols). The error bars indicate the experimental standard deviation. The grey symbols are taken from Ref. [41]. The maximum hardness is obtained for Mo-50Nb in both measurements as well as the literature data.

4.7.2 Offset Yield Strength

No alloy showed a distinct yield phenomenon in the compression tests, thus the 0.2% offset yield strength $\sigma_{\mathrm{p0.2\%}}$ is presented for all alloys in Figs. 4.11 and 4.12. All corresponding stress-strain data are presented in Sec. 7.1. For the rest of this section, the 0.2% offset yield strength is abbreviated as "strength" of the investigated alloys.

The strength of Mo-Ti solid solutions is presented in Fig. 4.11 as filled circles together with the 5% offset yield strength data as open circles. The strength increases approximately linearly from (170±20) MPa for Mo up to 40 at% Ti. While the average value is higher for Mo-40Ti, the strength of Mo-40Ti and Mo-50Ti must be considered equal within the margins of error with $\sigma_{\mathrm{p0.2\%,Mo\text{-}40Ti}} = (967 \pm 42)$ MPa and $\sigma_{\mathrm{p0.2\%,Mo\text{-}50Ti}} = (873 \pm 55)$ MPa. For higher Ti contents, the strength decreases again approximately linearly, until a strength of (644±30) MPa is detected for 80 at% Ti. The fact that the peak strength is offset from 50% towards lower Ti contents is consistent with the hardness data presented before. It can be rationalized in the framework of the Maresca-Curtin models and will be discussed in Sec. 5.5. No literature data is available for comparison.

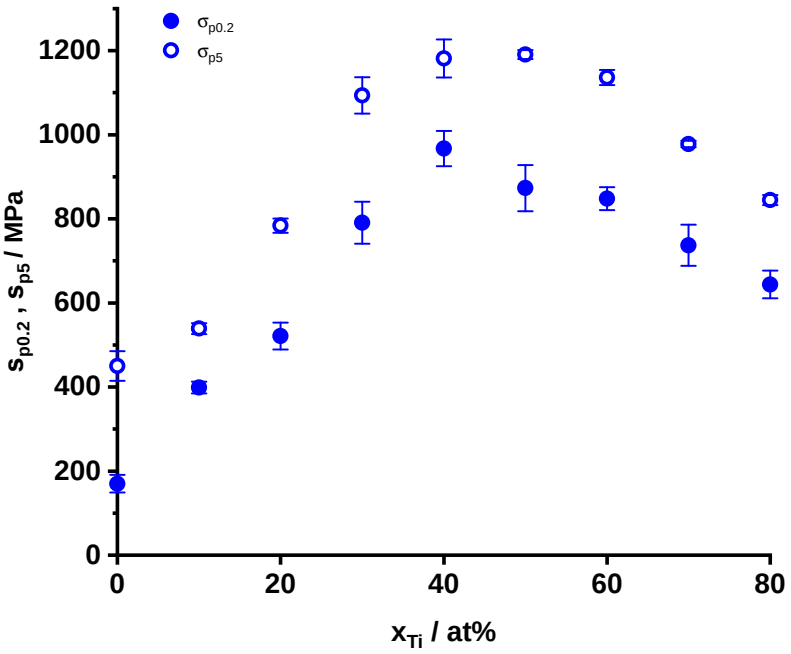

Figure 4.11: 0.2% (filled symbols) and 5% offset yield strength (open symbols) in Mo-Ti. No literature data are available for comparison. Similar to the hardness data, the maximum strength is obtained for Mo-40Ti.

In Mo-Nb, the increase in strength with increasing solute content is larger on the Nb-rich side than on the Mo-rich side, leading to a slightly asymmetrical shape leaning towards Nb-rich solid solutions, see Fig. 4.12. Strengths of Mo and Nb were detected to be $\sigma_{\mathrm{p0.2\%,Mo}} = (219 \pm 10)\,\mathrm{MPa}$ and $\sigma_{\mathrm{p0.2\%,Nb}} = (54 \pm 3)\,\mathrm{MPa}$, respectively. The maximum strength is obtained at $x_{\mathrm{Nb}} = 50\,\mathrm{at\%}$ with $\sigma_{\mathrm{p0.2\%,Mo\text{-}50Nb}} = (930 \pm 44)\,\mathrm{MPa}$, which is consistent with the results obtained in hardness measurements presented above.

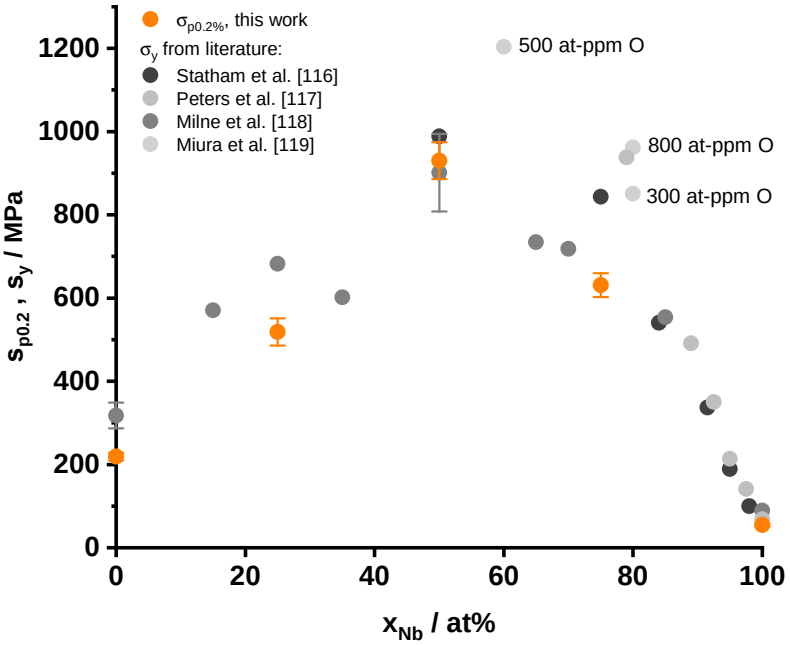

Figure 4.12: The 0.2% offset yield strength measured in polycrystalline Mo-Nb samples (orange symbols) agree well with available single crystal data from literature (grey symbols, from Refs. [116, 117, 118, 119]), recalculated according to the body text. The small numbers indicate detected O contents in at-ppm in Ref. [119]. These values might indicate that other, unexpectedly high yield strength data around 80 at% Nb are due to undetected O uptake during synthesis.

In contrast to Mo-Ti solid solutions, literature data are available for Mo-Nb solid solutions, which have all been obtained in single crystals [116, 117, 118, 119]. In order to compare the literature data for critical stress with the polycrystalline data obtained in this work, several experimental parameters were considered:

(i) All literature data were obtained in single crystals. Therefore, the values for critical stress were multiplied by a Taylor factor of 2.74 for the corresponding yield strength σ_{y} in polycrystalline samples [60].

(ii) Assuming a linear change of strain rate sensitivity m for Mo-Nb solid solutions ($m_{\mathrm{Mo}} \approx 0.04$ [120] and $m_{\mathrm{Nb}} \approx 0.11$ [121]), the data (original strain rates $\dot{\varepsilon} = 1 \ldots 6 \cdot 10^{-4}\,\mathrm{s}^{-1}$) were recalculated to a strain rate of $\dot{\varepsilon} = 1 \cdot 10^{-4}\,\mathrm{s}^{-1}$.

(iii) Ref. [117] reported no difference in critical stress for compression and tensile testing, thus results for both loading directions are shown.

(iv) Ref. [116] does not report interstitial content of the tested samples. Ref. [117] presents "typical" analysis results for O and N contents, Ref. [118] gives an

"estimated" content of O and N. These values are similar to the values presented in this work. As samples for all three publications were synthesized by electron-beam float zone melting, the interstitial contents are assumed to be similar for samples in these works. Ref. [119] investigated the impact of interstitial O and thus oxidized the samples before compression testing. Their reported O values are included as small numbers in Fig. 4.12.

In Ref. [118], samples of different crystal orientations were tested. The results for the critical stress projected on the $[110]\langle 111\rangle$ slip system showed a large scatter, which results in the error bars for the literature data at Mo-50Nb in Fig. 4.12. However, a good agreement is obtained between the average value of the single crystal data and the polycrystalline results of this work.
The values between 75 and 80 at% Nb show a large scatter, between (630±30) MPa obtained in this work and 940 MPa [117] and 960 MPa [119]. The latter value was obtained in intentionally oxidized samples with 800 at-ppm O (see also the small number noted in Fig. 4.12). Thus, an undetected increase of interstitial contaminants might be an explanation also for the high strength values reported in Refs. [117] and [116]. However, this cannot be verified.

4.7.3 Correlation Analyses

Nanohardness and Vickers hardness as well as Vickers hardness and offset yield strength are correlated to investigate the impact of grain size and oxides as well as the grain orientation. Nanohardness is not affected by grain boundaries or oxides at grain boundaries, since the experiments are performed in the centers of a single or a few grains, while macroscopic compression testing is affected and averages over different grain orientations. Vickers hardness testing and nanoindentation both are indentation methods, where the sample is deformed to similar strain states, but the impact of the indentation size effect (ISE) needs to be considered [122]. Vickers hardness and offset yield strength of a material are correlated by the Tabor relation $\sigma_{\mathrm{p8\%}} = 0.33\,H$ [80]. As some of the samples investigated in this work failed before 8% plastic strain was reached, $\sigma_{\mathrm{p5\%}}$ is used in the correlation investigations.
The correlation investigations for Mo-Ti solid solutions are shown in Fig. 4.13. Hardness and nanohardness data sets can be correlated as $nH = 1.07\,H + 1.36\,\mathrm{GPa}$, with a very good correlation coefficient $R^2_{\mathrm{adj}} = 0.93$ (blue line and symbols, right axis). The offset between both data sets is attributed to the ISE. A correlation investigation in steels yields also the slope 1.07 between nH and H, and reports different offset values depending on the maximum load [123]. The correlation of offset yield strength and Vickers hardness yields the equation $\sigma_{\mathrm{p5\%}} = 0.285H$ with a good correlation coefficient $R^2_{\mathrm{adj}} = 0.84$ (black line and symbols, left axis). As the offset yield strength at 5% instead of 8% strain has been used, the value of 0.33 is not reached. However, 0.285 is close to the expected value.

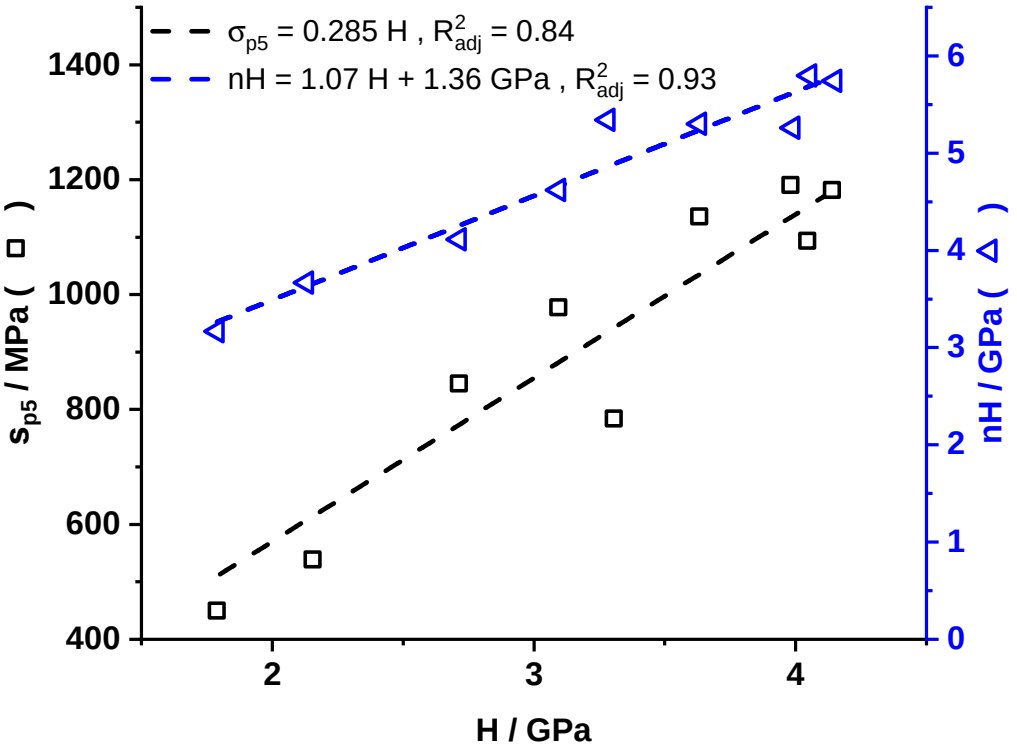

Figure 4.13: Good correlations have been obtained between Vickers hardness H and 5% offset yield strength σ_{p5} (black, left axis) as well as H and nanohardness nH (blue, right axis) for the investigated Mo-Ti solid solutions.

The correlation graphs for Mo-Nb solid solutions are shown in Fig. 4.14. The correlation between hardness and nanohardness is shown as orange symbols and line using the vertical axis on the right. Note that this axis has been offset for better visibility. The correlation between hardness and 5% offset yield strength is shown as black symbols and line using the vertical axis on the left. For the correlation between H and nH, the equation $nH = 1.22\,H + 0.4\,\mathrm{GPa}$ was found, with a very good $R^2_{\mathrm{adj}} = 0.97$ between both data sets. The correlation slope of 1.22 is larger than the one observed in Mo-Ti, but is consistent with a study of Ni-based alloys and steels [124], while the offset is much smaller. Offset yield strength and hardness can be correlated by $\sigma_{\mathrm{p5\%}} = 0.273\,H$ with $R^2_{\mathrm{adj}} = 0.99$. Similar to the results in Mo-Ti solid solutions, this value is slightly below, but close to the expected value of 0.33.

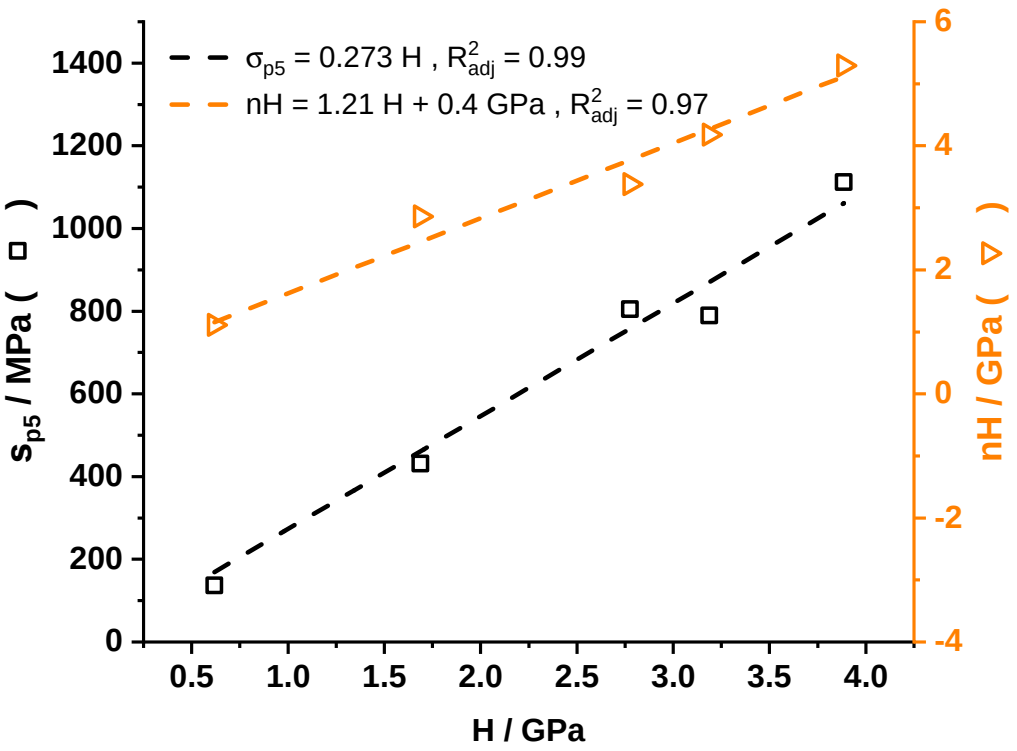

Figure 4.14: Correlation graphs between 5% offset yield strength σ_{p5} and H (black, left axis) and nanohardness nH and Vickers hardness H (orange, right axis). Note the offset on the right axis for better visibility of the data set. Very good correlations are found for the mechanical properties of Mo-Nb solid solutions.

Albeit predicted to be small [125], the difference in indenter shape between Vickers hardness testing and nanoindentation might impact the correlation functions between hardness and nanohardness. A systematic comparison of H and nH in the solid solution series, which encompasses different strain rates and maximum loads, a thorough analysis of the ISE and other parameters is outside the scope of this work. The good correlations with $R^2_{adj} \geq 0.84$ show that neither grain boundary effects nor grain orientation have a significant impact on the hardness of the solid solutions investigated here, and, consequently, also on the offset yield strength required for modelling. So far, this is only known for Mo, which shows only a weak grain size dependency for the hardness [43]. It is assumed to be true for several dilute Mo-based solid solutions, but is not experimentally confirmed in Ref. [43]. Nanohardness measurements in Mo yield only an approximately 3% deviation between different grain orientations [126], but again, data for Mo-based solid solutions have not been reported.

5 Modelling Results and Discussion

In order to identify the contributions by screw and edge dislocations to the yield strength, the experimental data have to be compared to the respective model predictions. Before a detailed discussion of the modelling results, the shear modulus determination is discussed in Sec. 5.1. The shear modulus G is required for the modelling after Labusch [35] and for the Maresca-Curtin model for edge dislocation-controlled strengthening [11]. As experimental data are not readily available for the solid solutions, the approach of the shear modulus calculation needs to be justified, including the assumption of linearly changing single crystal stiffnesses.
Then in Sec. 5.2, the expected impact of interstitial O on the yield strength is evaluated. While strengthening by O contamination can be neglected for Mo-Nb solid solutions, the O values are significantly larger in Mo-Ti. Accordingly, methods are presented and discussed to quantify and correct for interstitial strengthening by O in Mo-Ti solid solutions.
Using the corrected data, the results for modelling of substitutional solid solution strengthening are then discussed in the framework of several models:
In Sec. 5.3, the Labusch model [35] is applied to Mo-Ti solid solutions, while in Sec. 5.4, the Suzuki model [54] is applied to both solid solution systems, including recently suggested changes that are relevant for room temperature measurements [45].
In Sec. 5.5, both models developed by Maresca and Curtin [11, 40] are applied to both alloy systems. As the models for screw dislocation-controlled strength include conceptually similar key energy parameters, the values obtained for Mo-Ti and Mo-Nb solid solutions are compared in Sec. 5.6.
Sec. 5.7 then discusses the strength-controlling dislocation types for the alloys based on the modelling results. Continuing this discussion, a mathematical relationship is derived in Sec. 5.8 to predict the strength-controlling dislocation type for arbitrary BCC solid solutions.

5.1 Shear Modulus Modelling

The elastic properties of the solid solutions are required in the models, however, the data are not known for all compositions tested here. The single crystal stiffnesses, which can be used to calculate the shear modulus G and the bulk modulus B, can be obtained experimentally, e.g., from ultrasonic phase spectroscopy (UPS). Using G and B, Poisson's ratio ν and, consequently, Young's modulus E can be derived [8, 127]:

$$B = (C_{11} + 2\,C_{12})/3 \tag{5.1}$$

$$\nu = \frac{3\,B - 2\,G}{2\,(3\,B + G)} \tag{5.2}$$

$$E = 2\,G\,(1 + \nu) \tag{5.3}$$

The calculated Young's modulus can then be compared to the experimental indentation modulus to verify the calculated values, see also Sec. 4.6. Several different methods have been suggested in literature to calculate the shear modulus G from the single crystal stiffnesses C_{ij} or compliances S_{ij} in Voigt notation.

One common method is the Voigt-Reuss-Hill method: Voigt [128] and Reuss [129] both developed models to average the elastic response of polycrystalline material based on single crystal properties. Voigt considers a state of uniform strain, Reuss one of uniform stress across grains [27]. Hill recognized that both calculations represent boundary cases for the true state in a polycrystalline material, and suggests to average both values [127]. The resulting method of calculating the shear modulus is thus sometimes called the Voigt-Reuss-Hill (VRH) method [127]:

$$5\,G_{\mathrm{V}} = (C_{11} - C_{12}) + 3\,C_{44} \tag{5.4}$$

$$5\,G_{\mathrm{R}}^{-1} = 4\,(S_{11} - S_{12}) + 3\,S_{44} \tag{5.5}$$

$$G_{\mathrm{H}} = 0.5\,(G_{\mathrm{V}} + G_{\mathrm{R}}) \tag{5.6}$$

where the subscripts are used for the respective models of Voigt, Reuss and Hill.

An approach used by, e.g., Hirth and Lothe [130] and Foreman [131] yields equations for an effective shear modulus. Elastic energy is stored in the stress field of a dislocation. When the dislocation is deformed, for example, a pinned dislocation segment under applied stress, the energy increases, leading to a force counteracting the deformation. This results in the concept of a dislocation as a flexible string [27]. In an isotropic medium, the stored energy per dislocation line segment, the line tension Γ, scales as $\Gamma_{\mathrm{iso}} \propto G\,b^2$ with G the shear modulus and b the length of the Burgers vector [27]. However, real metals are not isotropic, and the dislocation line tension depends on the Burgers vector and dislocation line directions, as well as the single crystal stiffnesses to account for the material anisotropy. Mathematically, the anisotropic line tension can be described analogous to the isotropic one, with $\Gamma_{\mathrm{ani}} \propto K\,b^2$. K, called the "energy factor" [130, 131], replaces the isotropic shear modulus and has to be calculated for each combination of Burgers vector and dislocation line direction as a function of the stiffnesses. Thus, this energy factor can be considered an effective shear modulus in anisotropic media for a specific dislocation configuration.

Foreman [131] performed the calculations for dislocations in cubic crystals with Burgers vector and dislocation line directions along [101], i.e. screw dislocations in FCC metals, as

$$K_{[101],[101]} = \sqrt{0.5\, C_{44}\ (C_{11} - C_{12})} \equiv G_{\mathrm{F}} \tag{5.7}$$

Hirth and Lothe [130] calculated K for Burgers vector and dislocation line directions along [111], $K_{[111],[111]}$, for cubic crystals. This results in the effective shear modulus for a screw dislocation in BCC metals. The resulting formula can easily be calculated as a function of C_{ij} using computer assistance. However, it extends across several lines when written out and is not shown here for the sake of clarity. A formula provided by Kocks et al. [132] yields a good approximation to the exact formula. However, no derivation for this approximation is given:

$$G_{\mathrm{Kocks}} = \frac{1}{3}\ (C_{11} - C_{12} + C_{44}) \approx K_{[111],[111]} \tag{5.8}$$

Table 5.1: The single crystal stiffnesses for Mo, Ti and Nb used in the calculations for Young's modulus. Note that the single crystal stiffnesses of BCC Ti were acquired at 1000 °C.

Element	C_{11} / GPa	C_{12} / GPa	C_{44} / GPa
Mo [133]	463	158	109
Ti (1000 °C) [134]	134	110	36
Nb [135]	245	138	29

In Fig. 5.1, results for the discussed calculation methods are compared for the Mo-Ti system. Results for the energy factors after Foreman [131] and Hirth-Lothe [130] are shown as red and purple dashed lines, respectively. The approximation by Kocks et al. [132] to the latter is shown as grey dashed line. Results based on the shear modulus after Hill [127] are shown as green solid line, where the light green area indicates the range of the results using the Voigt [128] and Reuss [129] moduli. For each method, the concentration-weighted single crystal stiffnesses given in Tab. 5.1 were used. Note that the single crystal stiffnesses of BCC Ti were acquired at 1000 °C, but are used for room temperature modelling here. Using Eqs. 5.1 to 5.3, Young's modulus is calculated for each method and compared to the experimental indentation modulus values, shown as blue symbols in Fig. 5.1.

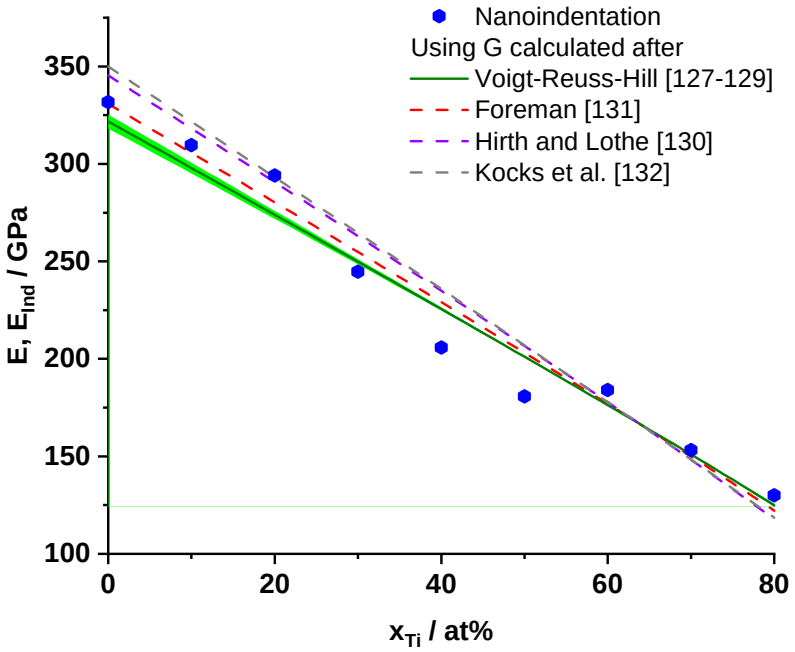

Figure 5.1: The results for the indentation modulus in Mo-Ti, E_{Ind} (also shown in Fig. 4.8). Young's modulus E calculated using the energy factors after Foreman [131] and Hirth and Lothe [130] are shown as red and purple dashed lines, respectively. The approximation to the latter suggested by Kocks et al. [132] is shown as grey dashed line. The Hill shear modulus [127] was used to calculate the solid dark green line. The light green area around the Hill calculations indicates the boundaries set by the Voigt [128] and Reuss [129] moduli. The moduli after Hirth and Lothe [130] and the approximation after Kocks et al. [132] result in too high moduli, while the VRH [127, 128, 129] and the Foreman [131] method yield similar results and close to the experimental data.

The overall differences between the different methods are small. The largest difference between the experimental data and the modelling methods are largest in Mo-50Ti with $\approx 20\,\mathrm{GPa}$ when compared to the VRH and Foreman methods and $\approx 30\,\mathrm{GPa}$ when compared to the Hirth-Lothe and Kocks methods. This deviation might be explained by deviations from a simple linear change in single crystal stiffnesses in these concentrated solid solutions. In order to remain consistent with published literature on the Maresca-Curtin models [11, 12, 13, 58], the effective modulus after Foreman, G_{F}, will be used in all solid solution strengthening modelling.

The calculations of elastic properties presented here assume a simple, linear concentration-weighted average of single crystal stiffnesses. While the good agreement of experimental indentation and modelled Young's moduli in Mo-Ti is a strong indication, it might be coincidence. In Ref. [136], the values for single crystal stiffnesses in Mo-Nb solid solutions were determined using UPS. Their experimental results together with linear functions based on the weighted pure element values are presented in Fig. 5.2. Deviations up to $\approx 20\,\mathrm{GPa}$ can be seen, for example between the calculated and measured value of C_{44} in the Mo-66Nb sample.

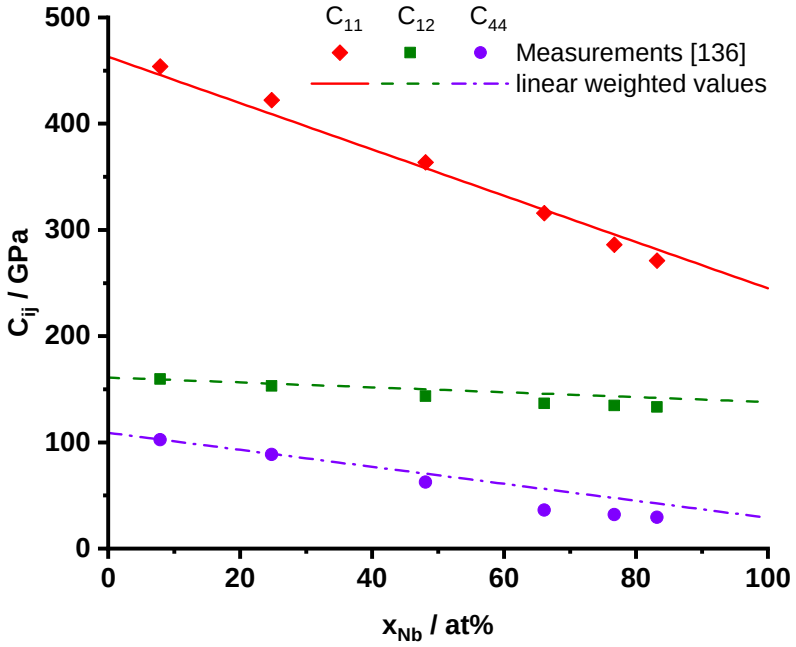

Figure 5.2: Measured single crystal stiffnesses of Mo-Nb solid solutions [136]: C_{11} as red diamonds, C_{12} as green squares and C_{44} as purple circles. Functions for linearly weighted data of pure elements are shown in the same colors as solid, dashed and dash-dotted lines, respectively. The assumption of linearly changing single crystal stiffnesses describes the overall trend very well.

To investigate the impact of these deviations further, G_F is used to calculate Young's modulus using the experimental data from Ref. [136] and the linear rule-of-mixture using the data from Refs. [133, 135]. These results are compared to the data obtained in this work by nanoindentation, see Fig. 5.3. For Mo-rich solid solutions, all data sets show good agreement. The deviation at Mo-50Nb of ≈30 GPa between the measured and the modelled value also remains compared to the literature data point at Mo-48Nb.
Similar to the difference in experimental and modelled single crystal stiffnesses, a deviation of ≈ 30 GPa is found for the Mo-66Nb sample compared to the linear rule-of-mixture. The indentation modulus at 75 at% Nb also shows a smaller value than the modelled Young's modulus with a difference of ≈ 15 GPa. Based on these results, the too large modulus at 50 at% Nb cannot be explained by the differences between experimental single crystal stiffnesses and the approximated linear rule-of-mixture. The source of error in the experimental result of Mo-50Nb remains currently unknown.

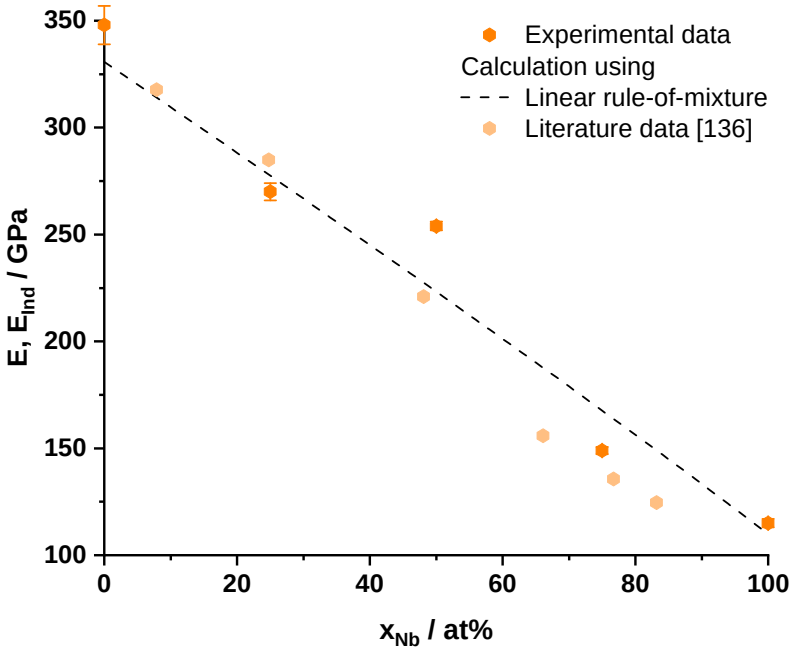

Figure 5.3: The results for the indentation modulus E_{Ind} in Mo-Nb (dark orange dots), shown in Fig. 4.8. For comparison, Young's modulus E was calculated using G_F and single crystal stiffnesses obtained in Ref. [136] (light orange dots) and a linear rule-of-mixture of the elemental data from Tab. 5.1 and Refs. [133, 135] (black dashed line). Overall, good agreement is found between both experimental data sets and the modelling using a linear rule-of mixture.

To conclude this section, the modelling results using G_F are compared to the experimental data in Fig. 5.4 for both solid solution series in a single figure. The results of the modelling are presented as dashed lines in their respective colours. For Mo and Nb, $E_{Nb,model} = 110\,GPa$ and $E_{Mo,model} = 331\,GPa$ are modelled, close to the experimental indentation modulus values of $E_{Nb,exp} = (115 \pm 2)\,GPa$ as well as $E_{Mo\text{-}0Ti,exp} = (332 \pm 3)\,GPa$ and $E_{Mo\text{-}0Nb,exp} = (348 \pm 9)\,GPa$, respectively. For both systems, the approximately linear trend is also reproduced. The largest deviations from the experimental values are found for Mo-40Ti and Mo-50Ti with 20 GPa each and for Mo-50Nb with approximately 30 GPa. Overall, a good agreement between modelling and experiments is obtained.

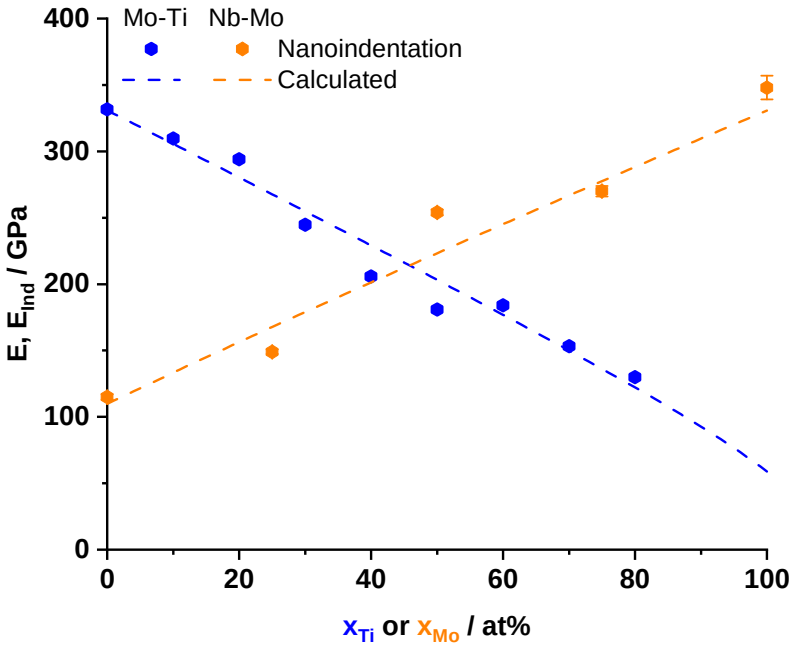

Figure 5.4: Results for indentation moduli for Mo-Ti (blue) and Mo-Nb (orange) and the modelled Young's moduli using G_F and a linear rule-of-mixture of the single crystal stiffnesses. Note that the horizontal axis is flipped for Mo-Nb compared to the normal depiction for better visibility. Error bars smaller than the symbol size are omitted. An approximately linear trend is detected for both solid solution series and in agreement with the modelling.

5.2 Interstitial Strengthening

While the Mo-Nb solid solutions contained only small O contents below 0.05 at%, the Mo-Ti solid solutions show comparatively large O contents up to 0.4 at% O, as has been shown in Fig. 4.5. These might have a significant impact on mechanical properties, similar to observations in the refractory metals Ta [137], Nb [138] or V [139]. The potential impact of interstitial O on solid solutions has been discussed in Sec. 4.7.2 for literature data for Mo-Nb. In Ref. [140], an increase in Vickers hardness of quenched Ti-9Mo solid solutions was detected for O contents up to 1.6 at% O. Thus, a method is required to account for interstitial strengthening contributions.

The impact of interstitial strengthening is modelled in two ways: A correction based on the Labusch model, which has been published in Ref. [58], and the already described interstitial correction within the Maresca-Curtin models, see Sec. 2.6.3. For both approaches, the data from Ref. [140] are used. In order to apply the models, it is assumed that the hardness ratio of O-containing and O-free alloys is equal to the ratio of offset yield strengths, $(H_{\text{O-rich}}/H_{\text{O-free}})_{\text{Ref. [140]}} = (\sigma_{\text{O-rich}}/\sigma_{\text{O-free}})_{\text{this work}}$. According to the threshold based on the electron-per-atom ratio [105], only solid solutions with ≥ 20 at% Ti are corrected.
While the original Labusch model includes contributions from G and ε_{L}, which both vary with solute concentration, a simplified approach is used here,

$$H_{\text{O-rich}} = A \cdot x_{\text{O}}^{2/3} + H_{\text{O-free}} \tag{5.9}$$

where the parameter A subsumes all numerical constants as well as G and ε_{L}. When the latter two are assumed to be constant over the investigated concentration range, A also remains constant. This simplified model then contains two free fit parameters, A and $H_{\text{O-free}}$.
For the Maresca-Curtin-consistent approach, Eq. 2.46 is used, $H_{\text{O-rich}} = H_{\text{O-free}} \cdot (1 + K_{\text{O}}\, x_{\text{O}})^{2/3}$, with K_{O}, which quantifies the strengthening by O, and $H_{\text{O-free}}$ as free fit parameters.
For both approaches, the equations are fitted to the published data to obtain values for the free parameters, see Fig. 5.5. The experimental data from Ref. [140] are shown as black squares. The simplified Labusch model is shown as red solid line, while the Maresca-Curtin-consistent approach is shown as green dashed line. The top axis shows the O content in wt% for comparison. Both the single and double-hatched areas indicate the concentration range for O in the Mo-Ti solid solutions: In the double-hatched area, the impact of O on the hardness is interpolated from the literature data. The single hatched area indicates the concentration range in which the O impact is extrapolated to lower O concentrations.

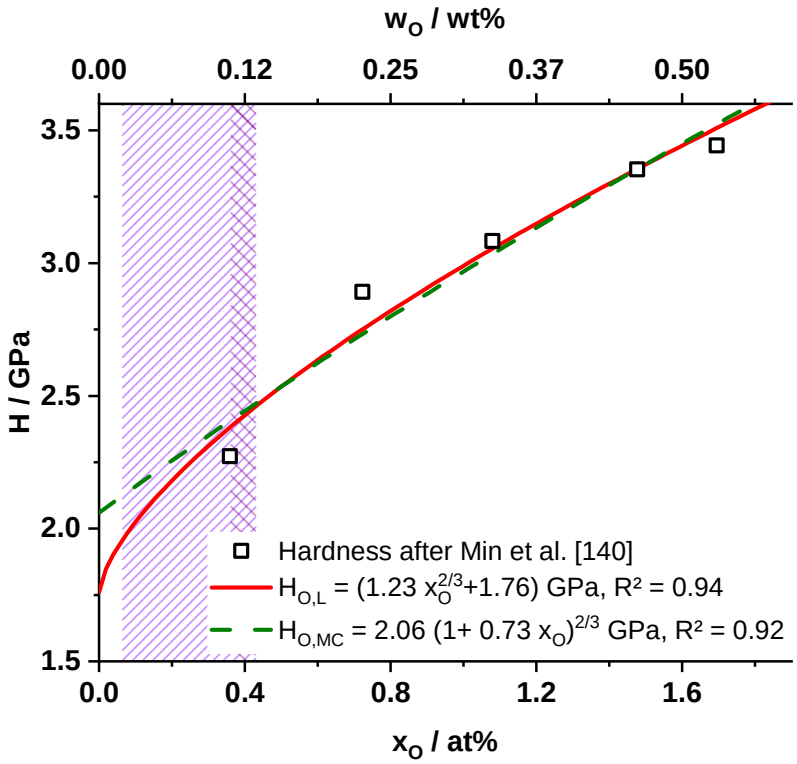

Figure 5.5: Vickers hardness in quenched Ti-9Mo solid solutions as a function of O content from Ref. [140]. At the top, the O contents are presented in wt% for comparison. The solid red and dashed green lines show fits to the data using a Labusch- and a Maresca-Curtin-consistent approach, respectively. The purple hatched area shows the O content in Mo-Ti solid solutions determined by HCGE, where the double hatched area shows interpolated and the single hatched area extrapolated O contents. Both models show good correlation to the data, and both indicate an approximately linear increase in hardness for large O contents. At smaller O concentrations, like the ones measured in Mo-Ti solid solutions, the differences in modelled O strengthening become more pronounced.

The fitted functions are

$$H_{\mathrm{O,Labusch}} = \left(1.23 \cdot x_{\mathrm{O}}^{2/3} + 1.76\right) \mathrm{GPa} \tag{5.10}$$

$$H_{\mathrm{O,MC}} = 2.06 \cdot \left(1 + 0.73\, x_{\mathrm{O}}\right)^{2/3} \mathrm{GPa} \tag{5.11}$$

Both fitted functions yield similarly good correlations, with $R^2_{\mathrm{adj}} = 0.94$ for the simplified Labusch fit and $R^2_{\mathrm{adj}} = 0.92$ for the fit according to the Maresca-Curtin model. Both modellings result in an approximately linear increase in hardness for large O contents. However, in the O range of Mo-Ti alloys studied here, the difference between both approaches is more pronounced. This is also reflected in the extrapolated hardnesses for an O-free alloy, $H_{\text{O-free, L}} = 1.76\,\mathrm{GPa}$ and $H_{\text{O-free, MC}} = 2.06\,\mathrm{GPa}$, respectively. Accordingly, the Maresca-Curtin model predicts a smaller impact of interstitial O than the Labusch approach.

Using the respective O contents determined by HCGE (Fig. 4.5 and Tab. 4.1), the increase in strength is calculated for each Mo-Ti solid solution and corrected for according to the fit functions. The measured $\sigma_{\mathrm{p0.2\%}}$ values together with corrected values are shown in Fig. 5.6, where the blue circles show the measured offset yield strength. The red filled circles are used for the correction following the Labusch approach and the green diamonds are for the Maresca-Curtin approach.
For the high-Ti solid solutions, where the O contents are above 0.3 at%, a correction for interstitial O is necessary. Here the corrected values are significantly smaller, approximately 200 MPa, than the uncorrected values. However, both models yield corrected values within one experimental standard deviation of each other. Thus, both approaches indicate the relevance of correction, but yield too similar results within the limits of the presented experiments for a clear distinction.

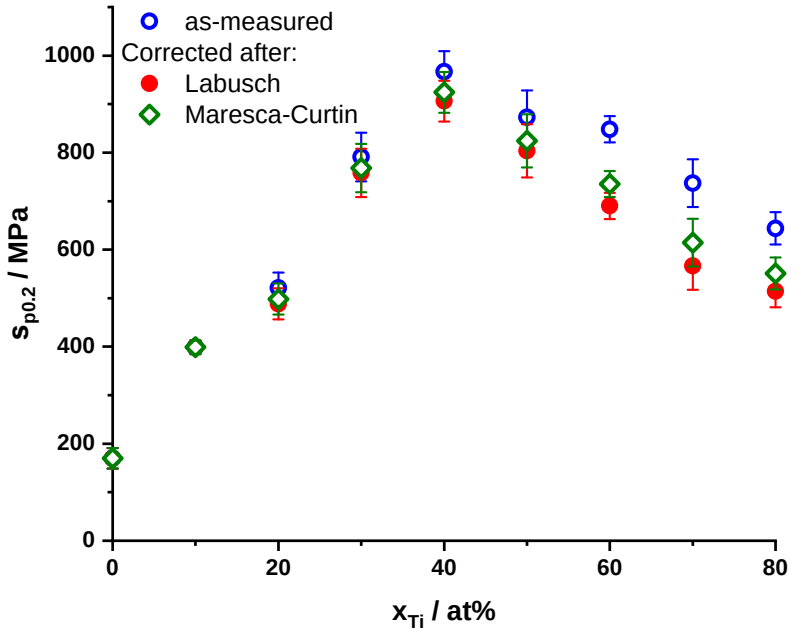

Figure 5.6: 0.2% offset yield strength of Mo-Ti solid solutions (blue open circles) and corrected for interstitial O values using both approaches. The red filled circles show a correction using the simplified Labusch model, the green diamonds a correction using a Maresca-Curtin-consistent approach. While both models indicate the necessity of correction for interstitial O, the corrections according both models are too similar to each other to make a clear decision.

Reports on interstitial strengthening by O in the refractory metals Nb, Ta and V indicate a concentration dependency for small O concentrations consistent with the Labusch model [137, 138, 139]. These results contradict the approximately linear increase as modelled in the Maresca-Curtin approach. However, this modelling includes the substitutional misfit volumes in the denominator of the strengthening parameter K_O. As there is no volume misfit in pure metals, it cannot be applied in these systems, but must be restricted to solid solutions only.
Available literature data on solid solutions are not suitable to clarify the applicability of either modellings in solid solutions: Either an insufficient number of data points is given in the desired concentration range [119], too large O contents are probed, where Labusch and Maresca-Curtin approaches show similar trends [141], or the precipitation of oxides is described [142]. Thus, more data is required to make a comprehensively informed decision. Here, the conservative approach after Labusch is used to correct the results for interstitial strengthening. This way, the results are also consistent with the published corrections from Ref. [58]. As the Mo-Nb solid solutions contain only O below the detection limit, no correction is necessary.

5.3 Labusch Model

The Labusch model [35] is only fitted to the data on Mo-Ti solid solutions, where a larger data set is available, see Sec. 4.7.2. It does not include new results made after its publication in 1970. However, it is still used today [41, 43]. The increase in yield strength in a solid solution compared to the base element is calculated as

$$\Delta\sigma_{\mathrm{p0.2}} = D'\, G\, \varepsilon_{\mathrm{L}}^{4/3}\, x^{2/3}$$

which includes the strengthening parameter $\varepsilon_{\mathrm{L}} = \sqrt{\eta'^2 + \alpha^2\delta_{\mathrm{F}}^2}$. The values for δ_{F} have been calculated using the polynomial fits to the lattice parameter, see Eq. 4.1, and have been presented in Fig. 4.7 a). η', which is based on the change in shear modulus with solute concentration, is calculated using G_{F} and the single crystal stiffnesses presented in Tab. 5.1 in the previous section, assuming a linear rule-of-mixture.

Both $D' = 2.74\,D$, which accounts for polycrystalline samples, and α remain as free parameters. Agreement between model and experimental data can be achieved for many combinations of D' and α as they are interdependent: For a high value of α, a correspondingly small D' can be found, and vice versa. If the factor D' was known for Mo solid solutions, α could be obtained by fitting. However, D' is only known for Cu solid solutions. Thus, the method of Ref [41] is adopted: Fitting of D' is performed for pre-set values of α between $\alpha = 1$ and a reasonable upper limit of $\alpha = 30$ in increments of 1. The quality of each fit is evaluated using R^2_{adj}. The highest value of R^2_{adj} then determines the best value of α to describe the data and, as a consequence, the dislocation type controlling the strength [41]. A fundamental assumption in this method is that the factor D' remains constant across the entire fitted concentration range. If the value of Cu solid solutions is used as a reference, as was in Ref. [43], a value of D' between 0.004 and 0.006 is expected.

The Labusch model distinguishes between solvent and solute atoms, and thus one fit for Mo-based solid solutions containing between 10 and 40 at% Ti and one for Ti-based solid solutions with at least 50 at% Ti are made. As the data shows a decrease in strength between 40 and 50 at% Ti, which is not captured by the Labusch model, this concentration range is not included in either fit. $\sigma_{\mathrm{p0.2\%}}$ of pure Mo is used as reference value for this part. For Ti-based fits, $\sigma_{\mathrm{p0.2\%}}$ for BCC Ti at room temperature is required as reference value, which cannot be obtained. Thus, a second free parameter is included, $\sigma_{\mathrm{BCC\text{-}Ti}}$. As the slope of the model function is only determined by D', while $\sigma_{\mathrm{BCC\text{-}Ti}}$ represents a constant offset, the parameters are not interdependent like α and D' would be.

The results of the fitting procedures are presented in Fig. 5.7. The fits with the highest R^2_{adj} are shown as purple dashed lines for both fit regimes as a function of Ti content. The colored areas indicate the ranges of modelled strengths between $\alpha = 1$ and the best fit α (green checkered area) and between the best fit α and $\alpha = 30$ (red hatched area). The experimental data are shown as blue symbols.
For the Mo-based alloys, $\alpha = 16$ is found as the best value, with $R^2_{\text{adj}} = 0.99$, which decreases to $R^2_{\text{adj}} = 0.91$ for both limit values. In the Ti-based alloys, $\alpha = 1$ is found as best value, with $R^2_{\text{adj}} = 0.95$. This value decreases to $R^2_{\text{adj}} = 0.86$ for $\alpha = 30$. For $\sigma_{\text{BCC-Ti}}$, values between 210 and 240 MPa are extrapolated by the fittings, which is higher as for pure Mo (170 MPa). The obtained values for D' are 0.017 and 0.015 for the best α-values in the Mo-rich and Ti-rich solid solutions, respectively. Compared to the data on Cu, these values are higher by a factor of $\approx 3 - 4$.

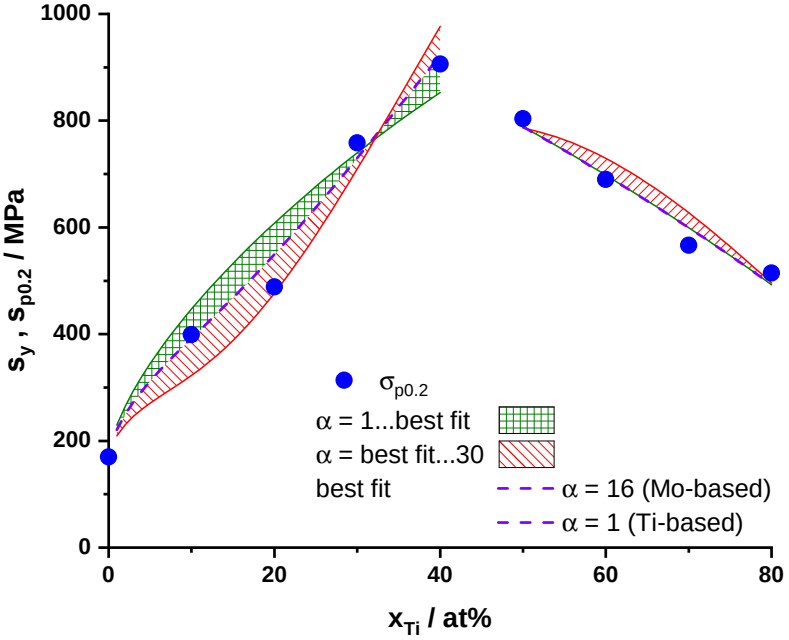

Figure 5.7: 0.2% offset yield strength of Mo-Ti solid solutions in comparison to the results of fitting procedures for the Labusch model. Two seperate procedures are made for Mo-based and Ti-based solid solutions. The strengths using the best fit values for α are 16 and 1 for Mo-based and Ti-based solid solutions, respectively, shown as purple line. The green checkered and red hatched areas depict the ranges of strength between the best fit value and the borders of the tested α values between 1 and 30. All modelled values are close to the experimental ones.

The obtained best fit values indicate a transition from edge (between 10 to 40 at% Ti) to screw dislocation-controlled deformation between 50 and 80 at% Ti as the value for the optimal α changes from 16 to 1. However, the values for R^2_{adj} are consistently high for all values of α in both data sets. Small differences in the experimental data might lead to different results of the fit quality and the resulting best fit α. Thus, the identification of the strength-controlling dislocation type is ambiguous at best. The high values for D' might indicate that the values for FCC Cu solid solutions cannot easily be used for BCC Mo solid solutions, questioning its application in Ref. [43]. In Ref. [42], the strengthening after the Labusch model in Mo-Si solid solutions underestimates the measured increase in yield strength by a factor of ≈ 5 when using $D' = 0.006$, supporting the results obtained here. However, the validity of the higher values for D' is based on the fundamental assumption that the Labusch model can be applied to BCC solid solutions.

Two problems in application of the Labusch model become apparent here:

(i) Due to the large difference in critical stress for screw and edge dislocations in BCC metals, the reference stress in the pure base element is always controlled by screw dislocation motion. This leads to an intrinsic contradiction of apparently identifying edge dislocation-controlled strength by using the screw dislocation-controlled base element value.

(ii) The fit to the Ti-based solid solutions results in values for $\sigma_{\text{BCC Ti}}$ between 210 to 240 MPa compared to $\sigma_{\text{Mo}} = 170$ MPa. Both the calculated shear moduli ($G_{\text{Mo}} \approx 6\, G_{\text{BCC-Ti}}$) and the experimental Vickers hardness values ($H_{\text{Mo}} \approx 1.5\, H_{\text{HCP-Ti}}$) do not indicate a higher yield strength for the hypothetical BCC Ti.

While the application of the model is attractive due to its simplicity, the problems show that the Labusch model is not suitable to identify the strength-controlling dislocation type in BCC substitutional solid solutions. However, the model can capture the correct order of magnitude for the strengthening. As shown in Fig. 5.7 by the green and red areas, all values of α between 1 and 30 and their corresponding values of D' provide a strengthening similar to the experimental data. Similarly, the estimate of interstitial strengthening is probably also of the correct magnitude, justifying the simplified Labusch approach to estimate the strengthening by O in Mo-Ti solid solutions.

5.4 Suzuki-Rao Model

The assumptions of the Suzuki model [36, 54, 55] are briefly repeated here:

(i) Only the closest neighbouring solutes interact with a screw dislocation.

(ii) These interactions increase the energy barrier for kink glide, which has to be overcome by thermal assistance.

(iii) The waiting time for thermal activation is much larger than the kink pair formation time, thus the latter effect is neglected.

(iv) Cross-kinks form when two gliding kinks on different glide planes meet. These cross-kinks are insurmountable barriers against further kink glide.

(v) These cross-kinks are overcome either by a Orowan-like bow-out of the dislocation between cross-kinks (Suzuki's assumption) or by breaking away, leading to the formation of a self-interstitial-vacancy pair (assumption by Rao et al. [45]).

The resulting equations are then:

$$\frac{\sqrt{2\,\pi}\,b}{3\,L\,x\,(1-x)} = \int_{\kappa_\mathrm{t}}^{\infty} \exp(-0.5\,y^2)\mathrm{d}y \tag{5.12}$$

$$\tag{5.13}$$

which links the average kink glide distance L to the probability of finding an insurmountably high energy barrier, quantified by the dimensionless parameter κ_t;

$$0 = \tau_\mathrm{k}^4 + S \cdot \tau_\mathrm{k} - R \tag{5.14}$$

$$\tag{5.15}$$

An equation to calculate the stress τ_k required to move kinks. S and R both are abbreviations, which have been described in Sec. 2.5;

$$\tau_\mathrm{xk} = 0.707\,\frac{E_\mathrm{SI} + E_\mathrm{V}}{4\,b^2\,L} \tag{5.16}$$

$$\tag{5.17}$$

A formula derived by Rao et al. [45] to calculate cross-kink breaking by self-interstitial-vacancy dipole formation;

$$\sigma_\mathrm{y} = 2.74\ (\tau_\mathrm{k} + \tau_\mathrm{xk}) \quad \text{at } L_0 \tag{5.18}$$

The yield strength is defined as the sum of both strength contributions at a specific glide distance L_0. The stress to move kinks increases with increasing glide distance L, the stress required to overcome cross-kinks increases with decreasing L. L_0 is the glide distance, where the minimum of the function is found. This minimization process also yields the equation:

$$0 = \kappa_\mathrm{t}^2 - \ln\left(\kappa_\mathrm{t}^2\right) - 2\ln\left(\frac{3\,G\,x\,(1-x)}{4\,\sqrt{2\,\pi}\,\tau_\mathrm{k}\,Q}\right) \tag{5.19}$$

$$\tag{5.20}$$

The definitions for all abbreviations and input parameters have been presented in Sec. 2.5.

For the modelling, several composition dependent parameters are required. Unless stated otherwise, a linear change of the respective parameters with concentration is assumed. DFT calculated values for the formation energies for vacancies, E_{V}, and self-interstitials, E_{SI}, of the elements are used [143, 144]. For Ti, the HCP values are used [144, 145] as there are no value for the BCC phase available. These values are listed in Tab. 5.2. The shear modulus is calculated using $G_{\mathrm{F}} = \sqrt{0.5\,C_{44}\,(C_{11} - C_{12})}$ and the single crystal stiffnesses presented before in Tab. 5.1. The values are repeated in Tab. 5.2 for convenience. Tab. 5.2 also presents the Debye temperature values to determine the Debye frequency and, as a consequence, estimate the kink dwell time to overcome energy barriers.

Table 5.2: Single crystal stiffnesses C_{ij} for Mo [133], Ti (BCC, at 1000 °C) [134] and Nb [135], the self-interstitial and vacancy formation energies E_{SI} [143, 145] and E_{V} [144] as well as the Debye temperatures Θ_{D} [134, 146, 147] used in the Suzuki modelling.

Quantity	C_{11}	C_{12}	C_{44}	E_{SI}	E_{V}	Θ_{D}
Units	GPa			eV		K
Mo	463	158	109	7.42	2.9	370
Ti	134	110	36	2.45	1.55	272
Nb	245	138	29	5.25	2.85	285

The length of the Burgers vector $b = \sqrt{\frac{3}{4}} \cdot a$ [40] and the distance between Peierls valleys $a_{\mathrm{P}} = \sqrt{\frac{2}{3}} \cdot a$ [40] both depend on the lattice parameter a. For the modelling, the polynomial functions described in Eq. 4.1 are used for the lattice parameter.

In Ref. [46], dislocation-solute interaction energy values are reported for a variety of solute-matrix atoms combinations, which are all determined using DFT calculations. These values are calculated using an extension of Eq. 2.18 for the four closest neighbouring atom columns surrounding the dislocation. The values relevant for the modelling here are presented in Tab. 5.3.

Table 5.3: Solute-dislocation interaction energies used in the Suzuki model implementation here, obtained via DFT calculations [46].

$E_{\mathrm{Ti\ in\ Mo}}$	41 meV
$E_{\mathrm{Nb\ in\ Mo}}$	39 meV
$E_{\mathrm{Mo\ in\ Nb}}$	123 meV

For Mo-Ti, the single value $E_{\mathrm{Ti\ in\ Mo}}$ was used for the entire system as there is no value available for strengthening by solutes in Ti. For Mo-Nb solid solutions, both values are used and combined according to the method proposed in Ref. [45], $E^2_{\mathrm{Mo\text{-}Nb}} = x_{\mathrm{Nb}}\,E^2_{\mathrm{Nb\ in\ Mo}} + x_{\mathrm{Mo}}\,E^2_{\mathrm{Mo\ in\ Nb}}$.

Solving Eqs. 5.12 to 5.18 is not trivial due to the interdependencies. Here, an iterative procedure is developed to solve the set of equations. In increments of 1 at%, the following steps are performed:

(i) Using $\kappa_t = 2.23$ from solutes in Fe [44] as a starting seed, L is calculated using Eq. 5.12.

(ii) This allows to solve Eq. 5.14 numerically, as then only τ_k is left as variable.

(iii) With τ_k, Eq. 5.19 can be solved for an improved value for κ_t, which then is used again for an improved calculation of L.

20 of these cycles are used to ensure reliability of the results. This method is free of any fit parameters when the relevant energy values are known, e.g., by DFT calculations. However, this also means that the modelling results depend critically on correct values of these input values.

Two important limitations must be noted: (i) Although the results settle to a fixed value after ≈ 10 cycles, and deviations continue decreasing for up to 50 cycles, there is no mathematically strict proof for convergence. There are also no boundary conditions or ranges of material parameters known for such convergence. (ii) The "converged" values might not be actually the physically correct ones, as Eq. 5.14 yields up to four solutions when $S = S(\tau_k)$ is not taken into account, and Eq. 5.19 up to two. The process for numerical solving gives only the solution closest to the starting seed. For Eqs. 5.14 and 5.19 these are kept constant as $\tau_{k,start} = 10^9$ GPa and $\kappa_{t,start} = 2$ for all modellings.

Results for the Suzuki-Rao modelling are shown in Figs. 5.8 and 5.9 as red solid lines for the Mo-Ti and Mo-Nb solid solutions, respectively. As the model does not apply to dilute solid solutions, the modelling results are not shown below 5 at%. The experimental offset yield strength values are shown as blue (Mo-Ti) and orange (Mo-Nb) symbols, respectively. Literature values for Mo-Nb solid solutions [116, 117, 118, 119] are shown as grey symbols.

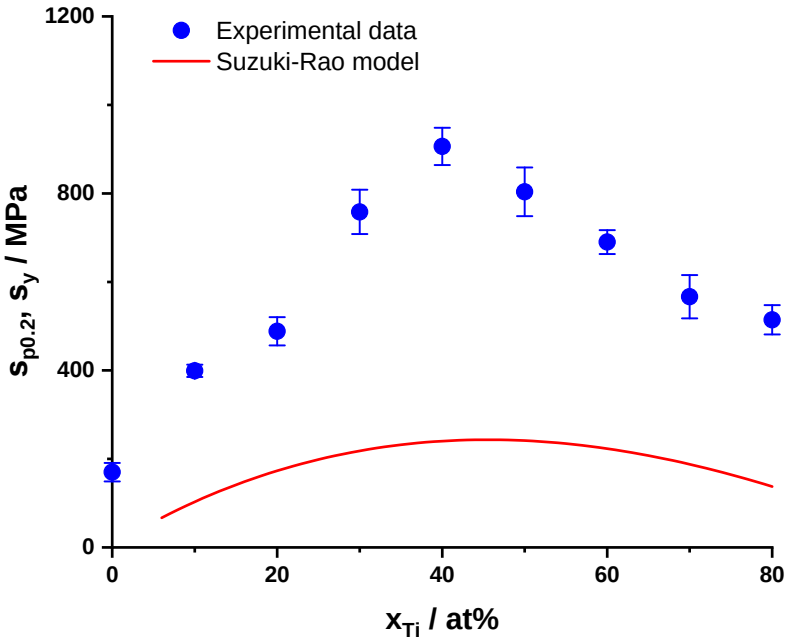

Figure 5.8: 0.2% offset yield strength of Mo-Ti (blue symbols) in comparison to the results of the Suzuki-Rao model (red solid line). As the Suzuki-Rao model does not apply to dilute solid solutions, values below 5 at% solute content are not shown. The modelled yield strength is much lower than the experimental values across the entire system.

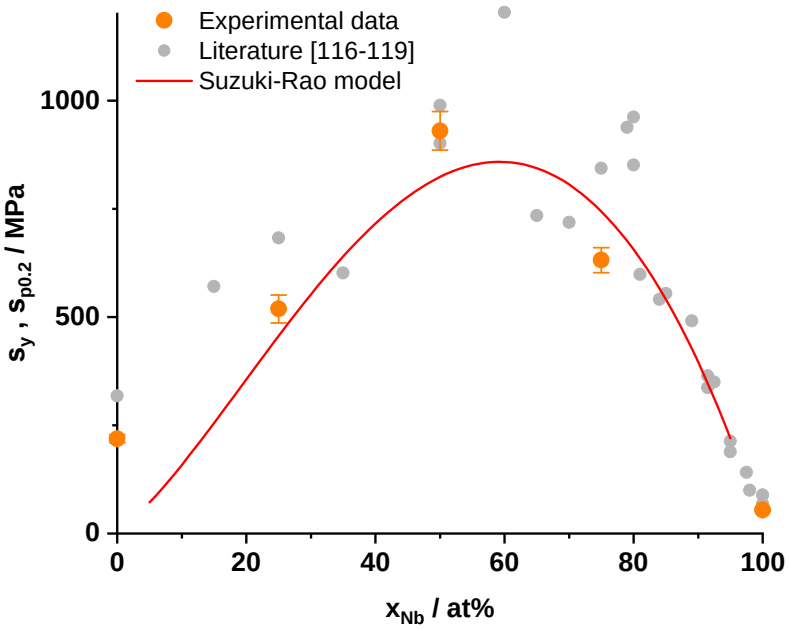

Figure 5.9: 0.2% offset yield strength of Mo-Nb (orange) and literature data on yield strength (grey) in comparison to the results of the Suzuki-Rao model (red solid line). All literature data [116, 117, 118, 119] are shown in a single color and symbol for clarity (see Fig. 4.12 for a detailed overview). As the Suzuki-Rao model does not apply to dilute solid solutions, values below 5 at% solute content are not shown. The experimental values of the entire system are well-captured by the modelling.

The strength in Mo-Ti solid solutions is underestimated in the model. While the maximum strength is reached at $x_{\mathrm{Ti}} = 45\,\mathrm{at\%}$, similar to the experimental maximum at $\approx 40\,\mathrm{at\%}$, the modlled strength is only 240 MPa compared to the experimentally obtained 900 MPa. The correlation of experimental and modelling results yields $R^2_{\mathrm{adj}} = 0.99$. However, the modelled strength is only 30% of the experimental one across the entire system. By contrast, the strength in the Mo-Nb system is well-modelled by the implementation. For the correlation investigation, own data and data published by Milne et al. [118] are compared to the modelling results in order to increase the number of data points. Both data sets contain results over the entire solid solution series and are obtained at the same strain rate, thus no assumption about the strain rate sensitivity is required. A correlation plot yielded $\sigma_{\mathrm{model}} = 0.93\,\sigma_{\mathrm{exp}}$ with a good $R^2_{\mathrm{adj}} = 0.95$. The model underestimates the strength only for Mo-rich solid solutions: At $x_{\mathrm{Nb}} = 15\,\mathrm{at\%}$, the model yields only about 45% of the experimental value.

Several problems arise in the application of the Suzuki model or its extension by Rao et al., both from a conceptual as well as a practical perspective, which need to be discussed. Ghafarollahi and Curtin describe fundamental problems in the Suzuki model in Ref. [47], which also hold true for the extension: (i) The enthalpy barrier for dislocation glide shows a singularity for $\tau \to 0$, i.e. at negligible applied stress, the barrier for kink motion is infinitely high. (ii) The activation volume is finite and nonzero for $T \to 0$, in contrast to theoretical [148] and experimental results [149]. Although these are valid points of criticism from a theoretical perspective, these limits are far off the practical experimental conditions investigated here.
The interdependent equations of the Suzuki-Rao model cannot be solved analytically but only numerically. Suzuki [55] only mentions "numerical methods" for solving the equations and Hattendorf and Büchner solve only a simplified version, which still requires numerical calculations [44]. Rao et al. describe their solving process as "numerical minimization with respect to κ_{t}" of Eq. 2.12 [45]. However, neither are further details, nor is their implementation code published. An independent analysis of their methods is thus not possible.

The only publicly available solving algorithm for the Suzuki-Rao model has been presented in Ref. [150]. For each atom species and for each concentration, the following steps are performed:

(i) A set of values for the energy barrier parameter κ_t is used to calculate the average glide length L. In their implementation, $\kappa_\mathrm{t} \in [1, 1.5, \ldots 4]$.

(ii) The cross-kink breaking stress τ_xk is calculated using E_SI and E_V for each κ_t.

(iii) Together with the solute-dislocation interaction energies $E_\mathrm{SD,i}$ from Ref. [46], a value for the kink glide stress τ_k is calculated by solving the equation $\tau_\mathrm{k}^4 + S\,\tau_\mathrm{k} - R = 0$ numerically for each κ_t.

(iv) $\tau_\mathrm{total} = \tau_\mathrm{xk} + \tau_\mathrm{k}$ is calculated for each κ_t and the resulting data set of κ_t and τ_total is fitted to a fourth order polynomial. The κ_t-value of the global minimum of this polynomial is then used to calculate the yield strength τ_y.

These calculation steps for the yield strength are performed for each atom species i independently and have to be added to obtain the total yield strength for a given composition, $\tau_\mathrm{y,\,total} = \sum_i \tau_\mathrm{y,i}$. This follows one of the suggestions for MSS from Ref. [45]. E.g., for each concentration in Mo-Nb solid solutions, the total yield strength is calculated as sum of strength contributions from Mo and Nb, $\tau_\mathrm{y,\,total} = \tau_\mathrm{y,Mo} + \tau_\mathrm{y,Mo}$.

Results for the different implementation methods are presented in Fig. 5.10. Rao et al. only published results for solid solutions with 8.5 at% and 19 at% Mo (blue triangles) [46]. A factor of 2.74 was included to account for polycrystalline samples and the published data is corrected for the strain rate as described in Sec. 4.7.2. The implementation after Ref. [150] is adapted to model at the correct strain rate; and the concentration dependency in the model is altered from x to $x\,(1-x)$ to remain consistent with the approach used here for concentrated solid solutions. Increments of $\Delta\,x_\mathrm{Nb} = 10\,\mathrm{at\%}$ are modelled. The strength at 8.5 at% and 19 at% Mo are also calculated, where the data from Rao et al. is available. The results are shown as green dashed line. Results for the implementation method presented here are shown as red solid line.

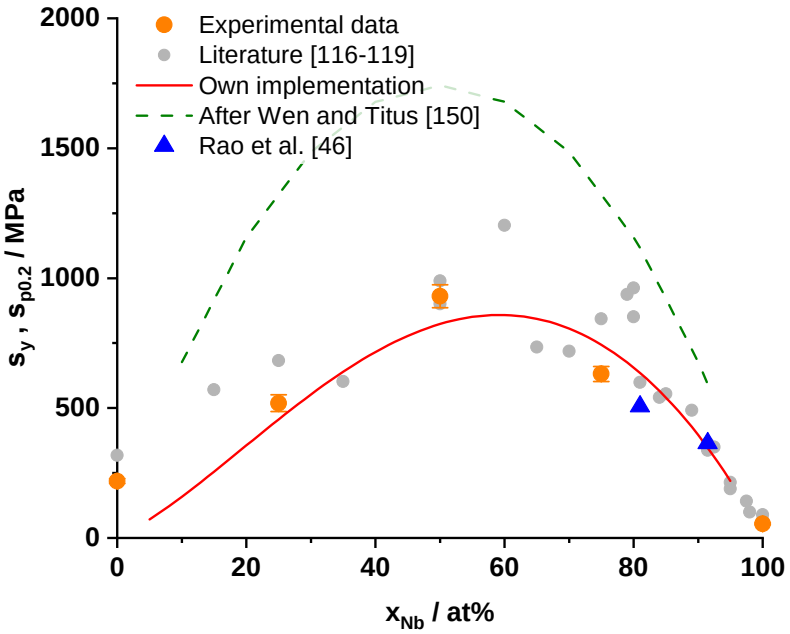

Figure 5.10: The yield strength of Mo-Nb solid solutions in the Suzuki-Rao model as implemented in Ref. [150] (green dashed line), Ref. [46] (blue triangles) and as presented here (solid red line) in comparison to experimental results. Own data are shown as orange circles, literature data as grey circles [116, 117, 118, 119]. The here presented model implementation and the modelling results from Ref. [46] agree well with experimental data. The implementation presented in Ref. [150] overestimates the strength significantly.

The available results of Rao et al. [46] show a similar strength as the implementation introduced here, which both agree with experimental data. The implementation after Ref. [150], however, predicts a too large strength for all concentrations. For example for Mo-50Nb, about twice the experimental strength is modelled. The implementation of the Suzuki-Rao model presented here yields results similar to the implementation by Rao and co-workers, who are the leading proponents of this model. Additionally, good agreement with experimental data is achieved, further supporting the validity of the implementation. In contrast to the implementation by Rao et al. [46], the code used here is publicly available [151]. This allows everyone to apply and adapt the code according to their needs.

While the implementation from Ref. [150] is also publicly available, the results indicate issues in modelling binary solid solutions. The original implementation from Ref. [150] uses the linear concentration term x and yields an approximately linear increase in strength with increasing Nb concentration from 500 MPa at 10 at% Nb to 1300 GPa at 90 at% Nb (not shown here). As independent strength contributions of the Mo-based and Nb-based solid solutions are added in this implementation, the predicted strength is dominated by the strength of the Nb-based solid solutions due to the larger interaction energy with $E_{\text{Mo in Nb}}/E_{\text{Nb in Mo}} \approx 3$. When the parabolic concentration dependency $x\,(1-x)$ for concentrated solid solutions is used, the parabolic strength shown in Fig. 5.10 is obtained, which is also too high.

The implementation from Ref. [150] is also tried for modelling the strength in Mo-Ti solid solutions, using the parabolic concentration dependency and the correct experimental strain rate. As in the own implementation, $E_{\mathrm{Ti\ in\ Mo}} = 41\,\mathrm{meV}$ was used for the entire system. The results are shown in Fig. 5.11 as green dashed line. For comparison, the implementation as developed here is shown as red solid line, while the experimental data are shown as blue dots. Similar to the results in Mo-Nb the implementation after Ref. [150] results in approximately twice as large predicted strengths, however the experimental data are still not reproduced.

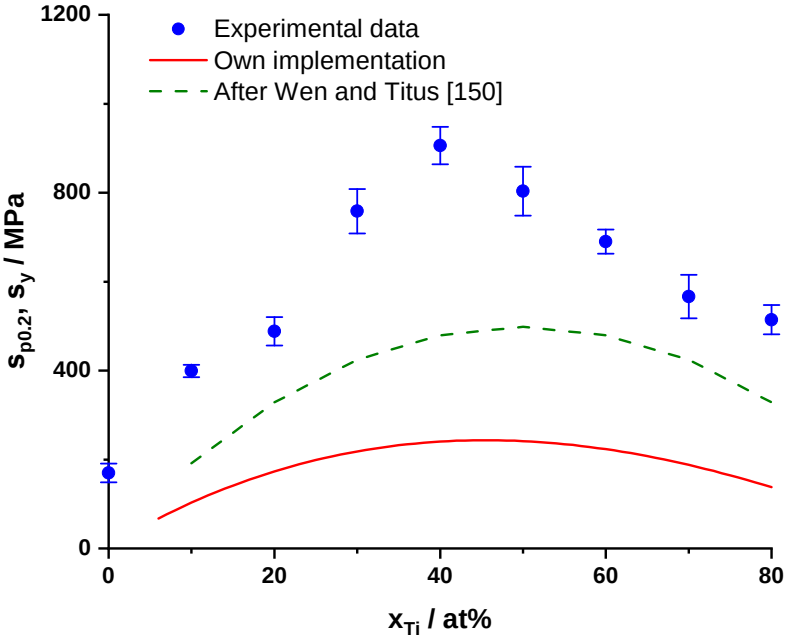

Figure 5.11: The yield strength of Mo-Nb solid solutions in the Suzuki-Rao model as implemented in Ref. [150] (green dashed line) and as presented here (solid red line) in comparison to experimental results (blue symbols). The here presented model implementation, as well as the implementation from Ref. [150] both underestimate the strength of Mo-Ti solid solutions when the available interaction energy is used. Similar to Mo-Nb solid solutions, the implementation after Wen and Titus predicts approximately twice the strength of the implementation presented here.

Several assumptions in the implementation of Ref. [150] might contribute to the large deviation from the implementation presented here. The coarse increment step size of κ_t of 0.5 can be ruled out. For an increment size of 0.01, a plausible increment based on the results of the presented implementation, the approximately twice as high yield strength is still predicted. Remaining sources for the large deviation are then:

- The use of a fourth order polynomial for finding the minimum value of κ_t. It is not explained in the publication nor can it be derived from the Suzuki-Rao equations.
- The addition of species-specific strength contributions to the total alloy strength. It is suggested by Rao et al. [45] as one option to calculate the strength in MSS. This approach assumes that there are several independent kink glide processes, one for each atom species, and the results of these processes can simply be added. Thus, dislocation motion would be hindered independently by each atom species. As the energy landscape encountered for each kink is always a combination of interactions with all atom species, the use of an effective interaction energy, which combines contributions of all species, is more plausible.

Only the interaction energy for Ti solutes in Mo has been reported, $E_{\text{Ti in Mo}} = 41$ meV [46], and this value is used to model the strength of the entire system. While this might explain deviations for Ti-rich solid solutions, the strength for small Ti contents should be predicted reasonably well, similar to Mo solutes in Nb. Still, at 10 at% Ti, the model yields 100 MPa, while the experimental value is 400 MPa. Based on the results in Mo-Nb solid solutions, the model implementation can yield plausible results for the strength in BCC solid solutions. The dislocation-solute interaction energies are obtained by model-independent DFT simulations and, as such, should provide a robust estimate for strengthening. This seems to be true for Mo solutes in Nb-rich solid solutions with $E_{\text{Mo in Nb}} = 123$ meV [46], but the strengthening by solutes in Mo is underestimated. While there is only a slight underestimation for Nb in Mo ($E_{\text{Nb in Mo}} = 39$ meV) [46], the predicted strength for Ti in Mo ($E_{\text{Ti in Mo}} = 41$ meV) [46] is underestimated drastically.

According to Ref. [46], these interaction energies are among the smallest calculated energies for solutes in Mo, even smaller than for W in Mo ($E_{\text{W in Mo}} = 47$ meV). Based on the interaction energies, strengthening by W, Ti and Nb should be similar in Mo, with W showing the largest strengthening. However, experimental results in literature do not correlate to these energy values: In Ref. [152], tensile testing reveals an almost 20 times as large increase in strength in Mo-1Ti and Mo-1Nb compared to Mo-1W. Similarly, Ref. [43] reports an increase in Vickers hardness of 7 HV per 1 at% Ti compared to 1 HV per 1 at% W in dilute Mo solid solutions. These underestimations underline the need for correct interaction energy values in order to model the strength correctly. However, based on the modelling results discussed here and the trends in literature, the interaction energies published for Ti and Nb in Mo need to be considered wrong.

In Ref. [153], DFT simulations for Ti in W showed a strong contribution by solutes at fifth nearest neighboring sites. As the calculations in Ref. [46] are only performed up to the fourth nearest neighbors, any potentially large impact of farther sites is not captured. Due to the chemical similarity of Mo and W, it is reasonable to assume a similar situation for Ti in Mo, and, as a consequence of the modelling results here, probably also for Nb in Mo.

In order to determine the optimal interaction parameter for the Mo-Ti system, a least squares algorithm was applied to the Suzuki implementation. $E_{\text{Ti in Mo}} = 91\,\text{meV}$ was found by the algorithm, see Fig. 5.12. The experimental data is shown as blue symbols. The modelling result using the DFT calculated value is shown as red solid line, the modelling using the optimized value is shown as green dashed line. A good agreement is obtained between the model and the experimental data. This value is similar to ones that have been calculated by DFT for Ti solutes in Nb (90 meV) and Zr solutes in Mo (99 meV) [46].

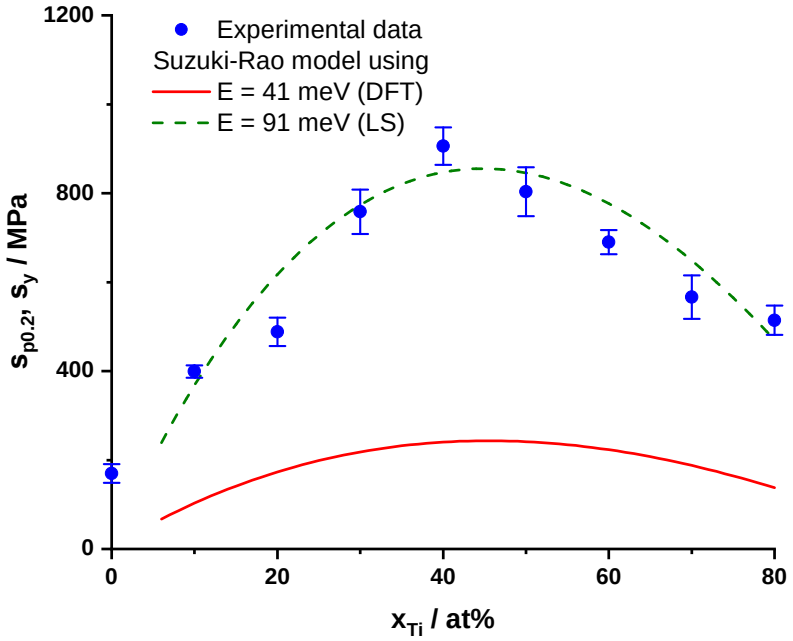

Figure 5.12: The yield strength of Mo-Ti solid solutions is not reproduced by the Suzuki-Rao model when the DFT calculated energy parameter $E_{\text{Ti in Mo,DFT}} = 41\,\text{meV}$ is used (red solid line). A least squares (LS) fitting algorithm found $E_{\text{Ti in Mo,LS}} = 91\,\text{meV}$ as best parameter to describe the experimental data (symbols).

5.5 Maresca-Curtin Models

The fundamental assumptions for the Maresca-Curtin models are briefly repeated:

(i) Local energy fluctuations due to different solute concentrations lead to a non-straight dislocation line in its lowest energy state.

(ii) Applied stress is required to advance the dislocation to the closest solute configuration with low energy in an average distance w_c.

(iii) For edge dislocations, this glide distance arises naturally from the calculations. Due to the high energy barrier, this distance is limited to $w_\mathrm{c} = a_\mathrm{P}$ for screw dislocation advancement.

(iv) The energy barrier arising from the local solute fluctuation is quantified by the energy parameter $\Delta\tilde{E}_\mathrm{p}(w_\mathrm{c})$.

5.5.1 Edge Dislocation Model

For edge dislocations with long-range pressure field, the energy parameter can be approximated using elastic theory. This includes the local lattice deformation quantified by the misfit volume of each constituent element n as ΔV_n and the alloy's shear modulus G and Poisson ratio ν. Remaining free parameters of the model are derived in Ref. [11] using a comparison of full-scale simulations and the elastic approximation. The results for Mo-Ti are published in Ref. [58]. The resulting equations are then

$$\tau_{\mathrm{y0,edge}} = 0.04\,\xi^{-1/3}\,G\left(\frac{1+\nu}{1-\nu}\right)^{4/3}\left[\frac{\sum_n x_n\,\Delta V_n^2}{b^6}\right]^{2/3} \tag{5.21}$$

$$\Delta E_\mathrm{b} = 2\,\xi^{1/3}\;G\,b^3\left(\frac{1+\nu}{1-\nu}\right)^{2/3}\left[\frac{\sum_n x_n\,\Delta V_n^2}{b^6}\right]^{1/3} \tag{5.22}$$

$$\sigma_{\mathrm{y,edge}}(T,\dot{\varepsilon}) = 3.06\,\tau_{\mathrm{y0,edge}}\,\exp\left(-\frac{1}{0.55}\left(\frac{kT}{\Delta E_\mathrm{b}}\ln\left(\frac{\dot{\varepsilon}_0}{\dot{\varepsilon}}\right)\right)^{0.91}\right) \tag{5.23}$$

The modelling of edge dislocation-controlled strength is identical for both alloy systems, except for the respective material-dependent inputs. The lattice parameter as a function of solute content is included via the two polynomial fits presented in Sec. 4.1. The shear modulus is calculated from the single crystal stiffnesses of the constituent elements, assuming a linear change with solute concentration. To calculate the shear modulus, $G_\mathrm{F} = \sqrt{0.5\,C_{44}\,(C_{11}-C_{12})}$ is used. The volume misfit, the difference in atomic volume between the actual alloy and a hypothetical average alloy, is calculated using the polynomial fits to the lattice parameter and the formulae for the volume misfits in binary systems, $\Delta V_1 = 1.5(1-x_1)\,a^2\,\frac{\mathrm{d}\,a}{\mathrm{d}\,x_1}$ and $\Delta V_2 = -x_1\,\Delta V_1/x_2$, where x_i describes the concentrations of Mo and Ti or Mo and Nb, respectively. A line tension parameter $\xi = 1/8$ is used.

The strength of Mo-Nb solid solutions is well described across the entire concentration range, see Fig. 5.13. The results of the edge dislocation model are shown as red solid line. The results of the screw dislocation model (green dashed line) will be discussed below. Experimental data are shown as symbols: Own data are shown in dark orange, the data by Milne et al. [118], measured at the same strain rate, is shown as light orange symbols. Other literature data, corrected for the strain rate, are shown in grey [116, 117, 119]. A correlation plot reveals overall a slight underestimation of the values, $\sigma_{\mathrm{model}} = 0.88\,\sigma_{\mathrm{exp}}$, but good correlation ($R^2_{\mathrm{adj}} = 0.97$). The underestimation becomes more pronounced for Nb-rich solid solutions. This underestimation can occur for example from slight deviations in the implemented single crystal stiffnesses compared to actual values, for example in Mo-50Nb, or from the selection of the line tension parameter $\xi = 1/8$. For example, recently, $\xi = 1/6$ was reported to improve the correlation to experimental data of W-Ta solid solutions compared to 1/8 [13].

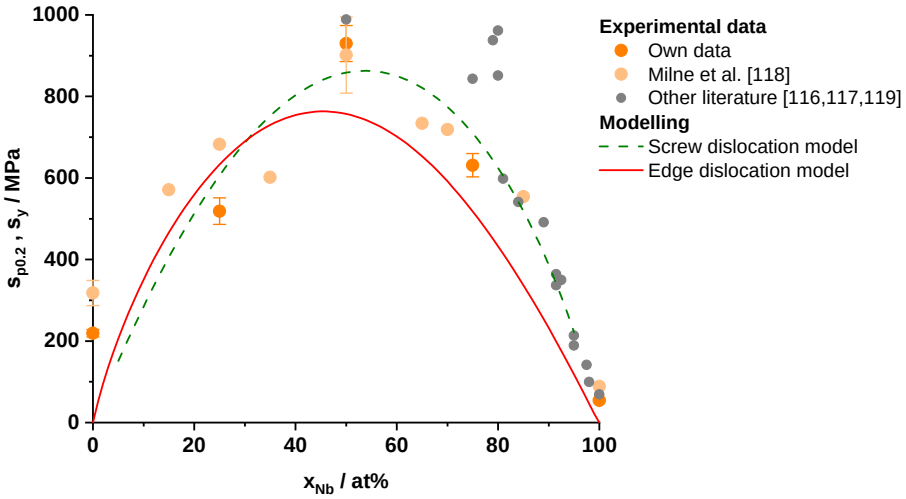

Figure 5.13: 0.2% offset yield strength of Mo-Nb (dark orange symbols) together with literature data in comparison to the results for the Maresca-Curtin screw dislocation model with two independent interaction parameters (green dashed line) and the edge dislocation model (red solid line). The light orange symbols show the data by Milne et al. [118], which were also used for fitting the screw dislocation model. All other literature data [117, 116, 119] were not used for fitting (shown in a single grey color). As the screw dislocation models do not apply to dilute solid solutions, values below 5 at% solute content are not shown. Both models can describe the experimental data over the entire system.

The strength of Mo-Ti solid solutions is matched only in high-Ti solid solutions with 60 at% Ti and more as shown in Fig. 5.14. The edge dislocation model is shown as red solid line, while the screw dislocation model (green dashed line) will be discussed below. Experimental 0.2% offset yield strength is shown as symbols. $\sigma_{\text{edge model}} = 0.63\,\sigma_{\text{exp}}$ with $R^2_{\text{adj}} = 0.78$ is found as correlation over the entire system, while the correlation plot yielded $\sigma_{\text{edge model}} = 0.99\,\sigma_{\text{exp}}$ with $R^2_{\text{adj}} = 0.99$ when only the high-Ti solid solutions are considered.

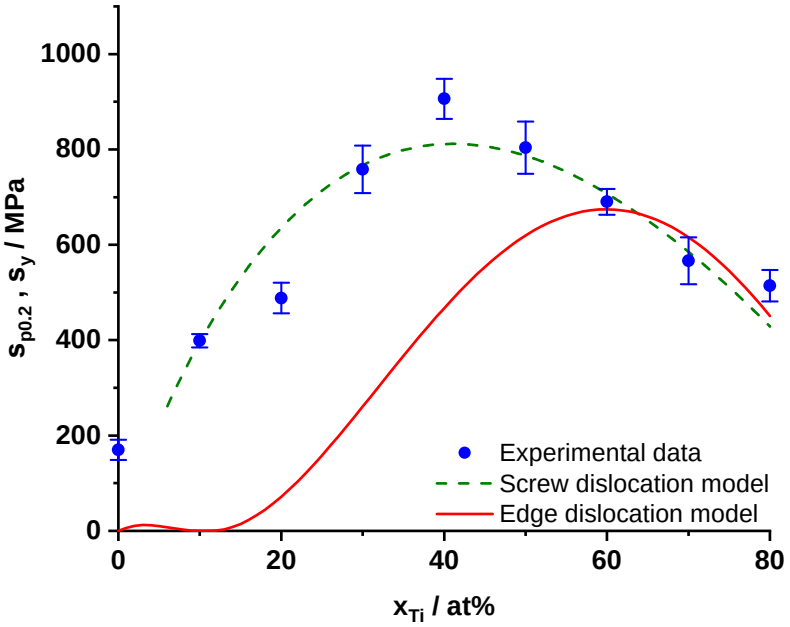

Figure 5.14: 0.2% offset yield strength of Mo-Ti (blue symbols) in comparison to the yield strength results of the Maresca-Curtin models. The red solid line shows results for the edge dislocation model, the green dashed line the fitted screw dislocation model. As the screw dislocation model does not apply to dilute solid solutions, values below 5 at% solute content are not shown. While the single-parameter screw dislocation model is able to describe the entire Mo-Ti system, the edge dislocation model shows good agreement for Ti-rich solid solutions.

The edge dislocation model does not require any fitting, but only relies on material properties which can be obtained from independent experimental analyses. In Mo-Nb solid solutions, the yield strength of the entire system can be described by this model with a slight underestimation of 12%. In Mo-Ti, only the high-Ti solid solutions with at least 60 at% Ti showed good agreement, while the strength is strongly underestimated in solid solutions with a lower Ti content. In both systems, the shape of the edge dislocation strengthening model is strongly influenced by the shape of the misfit function that has been described in Sec. 4.5. The second major contributing factor in the model is the shear modulus. As the shear modulus of Mo is larger than the moduli of both Ti and Nb, the peaks as observed in the misfit function are shifted towards the Mo-richer solid solutions.

5.5.2 Screw Dislocation Modelling in Mo-Ti

For screw dislocations, no elastic approximation is available. The solute-dislocation interaction energy $\Delta\tilde{E}_\mathrm{p}(w_\mathrm{c})$ remains as parameter that needs to be determined e.g. by DFT calculations. As these are not within the scope of this work, $\Delta\tilde{E}_\mathrm{p}(w_\mathrm{c})$ is treated as a fit parameter to the data. By leaving a free fit parameter, the resulting modelling might reproduce the experimental data although the fitted parameter might not represent the physical reality. Thus, the obtained fitted values must be evaluated against known literature data to determine its plausibility. The results for Mo-Ti are published in Ref. [58].

The model applied here does not consider kink-pair formation as rate-limiting contribution to dislocation advancement. It is assumed that there is always a large number of kinks available along the dislocation line due to the local energy fluctuation. A model extension for dilute solid solutions was developed to include the impact of double-kink nucleation [154]. Within the framework of this model, double-kink formation contributes significantly to the total yield strength below 5 at% solute content [47]. Similar to the Suzuki-Rao model, cross-kink breaking is one of the strength determining processes in the Maresca-Curtin model. Thus, vacancy and self-interstitial formation energies, E_V and E_SI, are required. The same values as for the Suzuki-Rao model are used, see Tab. 5.4, and again a linear change with solute concentration is assumed. Additionally, the kink formation energy, E_kink, is needed. For the entire Mo-Ti system, the value for Mo, $E_\mathrm{kink} = 0.5$ eV [155], is used, as there is no data available for kink formation in BCC Ti. Tab. 5.4 also presents the data for Nb used in the modelling of Mo-Nb solid solutions.

Table 5.4: Self-interstitial, vacancy and kink formation energies for Mo, Nb and Ti [143, 144, 145].

Element	E_SI / eV	E_V / eV	E_kink / eV
Mo	7.42	2.9	0.5
Nb	5.25	2.85	0.64
Ti	2.45	1.55	0.5

The self-interstitial formation energies are larger for all elements, thus it is the strength-controlling contribution for cross-kink breaking and $\zeta_\mathrm{V/SI} = \zeta_\mathrm{SI} = 15\,\zeta_\mathrm{c}$. As in the Suzuki-Rao model, a kink width of $w_\mathrm{k} = 10\,b$ is used. The Peierls-like mechanism is only active at high stresses and/or low temperatures, thus it is not considered here. For example for Mo-Nb solid solutions, the Peierls-like mechanisms has been modelled to be active below 100 K at a strain rate of 0.001 1/s [40, 47].

In order to obtain values for $\Delta\tilde{E}_{\mathrm{p}}(w_{\mathrm{c}})$, the interaction energies $\Delta U^{\text{Ti in Mo}}$ and $\Delta U^{\text{Mo in Ti}}$ are required, which have to be calculated for each position (i, j) relative to the dislocation line before and after dislocation glide. For the simplification required for fitting, it is assumed that:
(i) The position-dependent solute-dislocation energy can be subsumed in a single, *collective* interaction energy value for each type of solute,

$$(\Delta U_{\text{Ti in Mo}})^2 = \sum_{i,j} \left(\Delta U^{\text{Ti in Mo}}(i,j)\right)^2 \tag{5.24}$$

$$(\Delta U_{\text{Mo in Ti}})^2 = \sum_{i,j} \left(\Delta U^{\text{Mo in Ti}}(i,j)\right)^2 \tag{5.25}$$

(ii) These values scale linearly with solute concentration,

$$\Delta U_{\text{Ti-Mo}} = x_{\text{Mo}}\, \Delta U_{\text{Ti in Mo}} \quad \text{and} \quad \Delta U_{\text{Mo-Ti}} = x_{\text{Ti}}\, \Delta U_{\text{Mo in Ti}} \tag{5.26}$$

(iii) The dilute interaction energies are identical,

$$\Delta U_{\text{Ti in Mo}} = \Delta U_{\text{Mo in Ti}} \tag{5.27}$$

then, $\Delta\tilde{E}_{\mathrm{p}}$ can be written as

$$\Delta\tilde{E}_{\mathrm{p}} = \Delta U_{\text{Ti in Mo}} \sqrt{x_{\text{Ti}}\ (1 - x_{\text{Ti}})} \tag{5.28}$$

And only $\Delta U_{\text{Ti in Mo}}$ remains as single free fit parameter in Eqs. 2.42 and 2.44.
When fitting the equation of the total yield strength to the O-corrected data of Mo-Ti solid solutions, a $\Delta U_{\text{Ti in Mo}} = 151$ meV is obtained. This matches the experimental data for the entire system well, a correlation plot yielded $\sigma_{\text{model}} = 0.99\,\sigma_{\text{exp}}$ with $R^2_{\text{adj}} = 0.99$. The experimental and modelling results are presented in Fig. 5.14 in the previous section, where the fitted screw dislocation model is shown as green dashed line, the edge dislocation model as red solid line and the experimental data as symbols.

5.5.3 Screw Dislocation Modelling in Mo-Nb

The modelling of the Mo-Ti system assumes that the dilute interaction energies, $\Delta U_{\text{Ti in Mo}}$ and $\Delta U_{\text{Mo in Ti}}$, are identical. However, this is a simplification. DFT calculations show that interaction energies can differ by up to a factor of four when solute and matrix element are interchanged [46]. Thus, a more detailed modelling should allow for two distinct dilute interaction energies. Following the derivation in Sec. 5.5.2, but omitting the assumption (iii), a different term for $\Delta\tilde{E}_{\text{p}}$ is obtained [13]:

$$\Delta\tilde{E}_{\text{p}} = \sqrt{x_{\text{Nb}}\,(1-x_{\text{Nb}})} \cdot \sqrt{(x_{\text{Mo}}\,\Delta U^2_{\text{Nb in Mo}} + x_{\text{Nb}}\,\Delta U^2_{\text{Mo in Nb}})} \tag{5.29}$$

For Nb-rich solid solutions, $\Delta U_{\text{Mo in Nb}} = 190\,\text{meV}$ is found in Ref [40]. Then $\Delta U_{\text{Nb in Mo}}$ remains as single free parameter. For E_{V}, E_{SI} and E_{kink} in Mo, the same values are used as before, see Tab. 5.4. Again, self-interstitial energies are larger than vacancy formation energies. The resulting equations for screw dislocation-controlled strengthening are fitted to own data and the data published by Milne et al. [118] due to the identical strain rate. The fitting yields $\Delta U_{\text{Nb in Mo}} = 121\,\text{meV}$ for Nb solutes in Mo with $\sigma_{\text{model}} = 1\,\sigma_{\text{exp}}$ and $R^2_{\text{adj}} = 0.98$. The results for screw and edge dislocation modelling in Mo-Nb are shown in Fig. 5.13 as green dashed and red solid lines, respectively. Experimental data are presented as dark orange for own results, light orange for the data by Milne et al. [118], which is also used for fitting, and grey symbols [116, 117, 119].

In both systems, the fitted screw dislocation model was able to reproduce the experimental strength well. The asymmetry in strength for Mo-Ti solid solutions is obtained in the screw dislocation modelling. The large difference in self-interstitial energies ($E_{\text{SI,Mo}} = 7.24\,\text{eV}$ and $E_{\text{SI,Ti}} = 2.45\,\text{eV}$) results in a strong decrease in the cross-kink strength contribution with increasing Ti content, which causes the maximum strength to be shifted towards the Mo-rich alloys. In Mo-Nb, the self-interstitial energies are similar, and thus cannot explain the experimentally observed asymmetric shape. The different interaction energies, $\Delta U_{\text{Mo in Nb}} = 190$ meV [40] and $\Delta U_{\text{Nb in Mo}} = 121$ meV can explain this asymmetry. However, using $\Delta U_{\text{Nb in Mo}}$ as explanation must be done with reservations. As it is fitted to the experimental data, its value is found to describe the experimental data best, independent of a physical basis of the value for $\Delta U_{\text{Nb in Mo}}$. Here, an independent method of energy determination is necessary to clarify the question, which is not available except via DFT calculations.

As the Maresca-Curtin model has been only recently published, literature data is scarce for comparison. Similar values to the ones found in Mo-Ti and Mo-Nb are presented in Ref. [13]: $\Delta U_{\text{Ta in W}} = 137$ meV is determined by DFT simulations and $\Delta U_{\text{W in Ta}} = 194$ meV is calculated analytically. Also in Ref. [13], $\Delta\tilde{E}_\text{p}$ is calculated for W-50Ta and Nb-50Ti as 84 meV and 55 meV, respectively. Using Eqs. 5.28 and 5.29, $\Delta\tilde{E}_{\text{p,50Ti}} = 75$ meV and $\Delta\tilde{E}_{\text{p,50Nb}} = 80$ meV are found, respectively, similar to the DFT calculated values.
The similarity of the values supports the plausibility of the fit results. Qualitatively, all these values agree with the Vickers hardness data from Ref. [41]. A confirmation of the fitted results can only be obtained by DFT calculations. Rao et al. published a large database for interaction energies for the use in the Suzuki model [46], covering DFT calculations for 12 species of refractory and non-refractory atoms as solutes in four species of refractory atoms as matrix. A similar database for the Maresca-Curtin model is not available. The adaptation of the available energies from the Suzuki to the Maresca-Curtin model is not as straightforward as one would expect as will be discussed in the next section.

5.6 Comparison of Interaction Energy Parameters

While own DFT calculations are not within the scope of this work, values for the interaction energy between a dislocation and specific solutes in a given matrix are available in literature, e.g. in [13, 40, 46, 156]. These energies are the basis for the strength controlled by screw dislocation motion in the Suzuki-Rao and the Maresca-Curtin model. Due to the conceptual similarity of the energy parameters in both models, they can be correlated to each other [46, 153]: Both reduce solute-dislocation interactions into a collective energy and calculate this value as energy difference before and after dislocation glide. Accordingly, both parameters share a common mathematical formulation. The difference between both models is that the Suzuki-Rao model distributes the total energy among the six atoms closest to the dislocation, while the Maresca-Curtin model merges this energy into a single atom. Thus, the following relation is obtained:

$$6\,E_{\text{Rao}}^2 = \left(\Delta U_{\text{Maresca-Curtin,collective}}\right)^2 \tag{5.30}$$

Therefore, the relevant input values from both models can be compared directly. For the Suzuki-Rao model, $E_{\text{Mo in Nb}} = 123$ meV and $E_{\text{Nb in Mo}} = 39$ meV from Ref. [46] are used. These values calculate to $\Delta U_{\text{Mo in Nb,Rao}} = 301$ meV and $\Delta U_{\text{Nb in Mo,Rao}} = 96$ meV in the Maresca-Curtin models. For comparison, $\Delta U_{\text{Mo in Nb,fit}} = 190$ meV and $\Delta U_{\text{Nb in Mo,fit}} = 121$ meV are obtained by fitting the Maresca-Curtin model to the data. The results for Nb solutes in Mo agree, when a slight underestimation of $E_{\text{Nb in Mo}}$ is taken into account. For Mo in Nb, however, the recalculated value is more than 100 meV larger than the value obtained by fitting. For this parameter, a factor of $(\Delta U/E_{\text{SD}})_{\text{Mo in Nb}} = 190/123 \approx 1.55$ is required instead of $\sqrt{6} = 2.45$ to correlate both parameters.

For Mo-Ti, where a single parameter is used for the entire system, $E_{\text{Ti in Mo}} = 41$ meV does not yield plausible results in the Suzuki-Rao model, not even for dilute Mo-Ti solid solutions. If the fitted value from the Maresca-Curtin model is taken as reference, the respective Suzuki energy parameter should be $E_{\text{Ti in Mo}} = 151/\sqrt{6}$ meV= 61 meV, which is only 2/3 of the value obtained via fitting ($E_{\text{Ti in Mo}} = 91$ meV). Accordingly, for the interaction energy in the Mo-Ti system, a factor of $151/91 \approx 1.65$ is required instead of the value of $\sqrt{6}$, which has been proposed by proponents of both models [46, 153].

A factor of approximately 1.6 appears in both alloy systems between the fitted values from the Maresca-Curtin model and the values for the Suzuki-Rao model. In Mo-Ti solid solutions this value is obtained for the single interaction parameter in the entire system; for Mo-Nb solid solutions this factor is found for Mo solutes in Nb. However, there is currently no theoretical basis to explain this factor similar to $\sqrt{3} \approx 1.7$ and, based on the limited number of systems investigated here, it must be considered coincidence. For the W-Ta system, $\Delta U_{\text{Ta in W}} = 137$ meV and $\Delta U_{\text{W in Ta}} = 194$ meV are found for the application in the Maresca-Curtin models [13]. These are four and 1.3 times larger than the respective values calculated by DFT for the Suzuki model [46]. Again, the suggested factor of $\sqrt{6} \approx 2.45$ is not found.

The DFT calculated interaction energies between solutes and dislocation provide a model-independent quantity. As such they should be applicable in both the Suzuki-Rao and the Maresca-Curtin model, when the correct recalculation factor is taken into consideration. The proposed value of $\sqrt{6}$ to recalculate between both models does not seem to be a reliable method. There are three possible conclusions from the observation of these discrepancies:

(i) Either model (or even both models) implements correct DFT values in a wrong way, leading to the observed differences between fitted and DFT calculated values.

(ii) The currently available DFT calculations are too imprecise, because, e.g., farther locations have to be taken into consideration.

(iii) The alloys used for fitting might not all be suitable, e.g., their strength is controlled by edge dislocation motion instead.

In the extreme case, all possible conclusions might be true at the same time. Apparently correct modelling results thus might be a result of errors which cancel each other out. Based on the limited data available, neither conclusion can be excluded.

5.7 Deformation Mechanisms

Both, the presented solving method for the Suzuki model, as well as the Maresca-Curtin model for screw dislocation-controlled strengthening, are able to describe the experimentally observed yield strength of Mo-Ti and Mo-Nb solid solutions. DFT calculated values from literature [46] yield good agreement only for the Suzuki model applied to Mo-Nb solid solutions. In all other cases (Suzuki model applied to Mo-Ti, both applications of the Maresca-Curtin model), fitting procedures are required to obtain the energy parameters necessary for agreement with experimental data. The results are summarized in Fig. 5.15 as red solid (Suzuki-Rao) and green dashed (Maresca-Curtin) lines in a) for Mo-Ti and b) for Mo-Nb. In both systems, good correlations to the experimental data with $R^2_{\text{adj}} > 0.95$ are obtained.

In Mo-Ti, alloys containing 60 at% Ti and more show comparable strength as modelled by screw and edge dislocation models. In Mo-Nb, all three tested solid solutions, Mo-25Nb, Mo-50Nb and Mo-75Nb show comparable strengths with $R^2_{\text{adj}} > 0.97$ when tested against the models. The results are shown in Fig. 5.15 as purple dash-dotted lines in a) for Mo-Ti and in b) for Mo-Nb solid solutions. The respective experimental data are shown as blue and orange symbols, respectively. Values from literature are shown as grey symbols [116, 117, 118, 119].

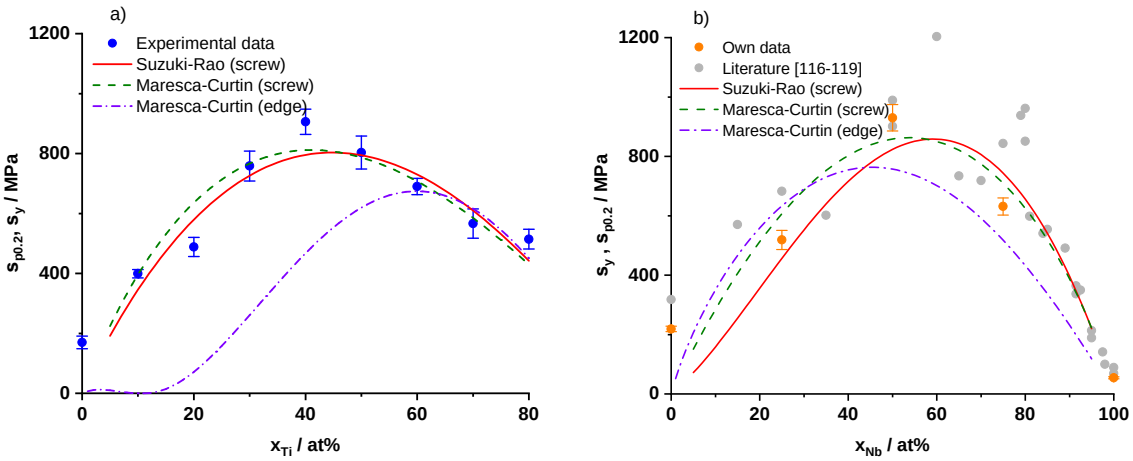

Figure 5.15: Experimental and modelling results for Mo-Ti solid solutions in a) and Mo-Nb solid solutions in b). Blue and orange circles indicate own experimental data, grey circles literature data [116, 117, 118, 119]. In both alloy systems, the results of the Suzuki-Rao model are shown as red solid line. The Maresca-Curtin models are shown as green dashed line for the screw dislocation model and as purple dash-dotted line for the edge dislocation model, respectively. Both screw dislocation models are able to model the strength in their respective systems when appropriate energy parameters are used. All three Mo-Nb and the Ti-rich solid solutions can also be modelled by the edge dislocation model.

Thus, strength in both solid solution series can be controlled by screw dislocations, which agrees with the established assumptions for BCC metals and alloys [7]. However, contrary to the traditional understanding, edge dislocation motion might also control the strength of solid solutions in both systems. Experimental verification of the strength controlling dislocation type is possible, e.g. by transmission electron microscopy (TEM) [10]. As this is not within the scope of this work, the models are evaluated against each other regarding their plausibility.

The edge dislocation model requires only readily available experimental values as input, the lattice parameter, Poisson's ratio and the shear modulus or single crystal stiffnesses. The yield strength can then be calculated using analytical equations with reproducible results. Both screw dislocation models share similar drawbacks, and thus are both inferior to the edge dislocation model regarding their reliability. Both rely on correct input values for the solute-dislocation interaction energy and self-interstitial and vacancy formation energies. If DFT calculations are not available to obtain these values, fitting or estimating these values is required. However, this process might result in an *apparently* good prediction of the yield strength. Even after comparison to similar available literature data, it is not clear if these values reflect the actual underlying physics of the system or if a wrong input value, combined with a wrong model, leads to good agreement with experimental results.

In a direct comparison of both screw dislocation strengthening models, the Maresca-Curtin model should be preferred over the Suzuki-Rao model. The yield strength predictions are very similar, as can be seen in Fig. 5.15. However, the Maresca-Curtin model uses a set of equations that can be solved analytically, and thus yields identical results for identical input parameters. By contrast, the Suzuki model requires numerical methods to obtain yield strength results. Not all implementation methods are publicly available [45, 150], thus a comprehensive, critical analysis of the different methods is not possible. Different algorithms thus might lead to different results without the possibility of independent verification. Until there is a singular, generally accepted implementation of this model, all results using this model have to be interpreted carefully.

Based on the above discussion, the yield strength of Mo-Ti solid solutions containing $x_{\mathrm{Ti}} \geq 60\,\mathrm{at\%}$ is likely edge dislocation-controlled. Below this concentration, only the screw dislocation models reproduce the experimental data; thus, these alloys must be considered screw dislocation-controlled. In Mo-Nb solid solutions, while there is a slight underestimation especially for dilute Nb-rich solid solutions, the overall trend of the data is well-captured by the edge dislocation model. Thus, the majority of Mo-Nb solid solutions shows also most likely edge dislocation-controlled yield strength. Both independent models for screw dislocation strengthening reproduced the yield strength for Ti-rich solid solutions and the entire Mo-Nb solid solution system. A strength contribution by screw dislocations can therefore not be ruled out for any of these alloys. These alloys can thus be considered as being of "competitive" strength (of both dislocation types) until the dislocation type has been identified conclusively in experiments.

A threshold for competitive strengthening by both dislocation types has been proposed recently based on the Maresca-Curtin models [13]. The authors in Ref. [13] correlate Vickers hardness measurements from Ref. [41] to the edge dislocation model and find $\delta_{\mathrm{th}} \geq 0.035$ as threshold misfit value for a good correlation parameter R^2_{adj} between hardness and model data. Neither the Mo-Ti nor the Mo-Nb solid solutions surpass this threshold. For Mo-Ti solid solutions, competitive strengthening is reached for alloys with at least 60 at% Ti or with a misfit of $\delta_{\mathrm{th,\ Mo\text{-}Ti}} \geq 0.028$. In Mo-Nb, competitive strengthening is observed for all three tested solid solutions with $\delta_{\mathrm{th,\ Mo\text{-}Nb}} \geq 0.019$. The threshold of $\delta_{\mathrm{th}} = 0.035$ is obtained as average value across all binary refractory solid solutions, and the impact of the shear modulus on the modelled strength is not considered. The shear modulus of Mo, $G_{\mathrm{Mo}} \approx 120\,\mathrm{GPa}$, is the second largest shear modulus from among all BCC metals [114]. Accordingly, edge dislocation-controlled strengthening can become competitive already for lower misfit values than the average threshold. The shear modulus for BCC Ti can be calculated from the single crystal stiffnesses in Tab. 5.1 to be $G_{\mathrm{Ti}} = 21\,\mathrm{GPa}$, which compares well to shear moduli of Ti-rich BCC solid solutions ($G_{\mathrm{Ti\text{-}rich\ BCC}} \approx 20 \ldots 30\,\mathrm{GPa}$) [157]. The shear modulus of Nb is experimentally available, $G_{\mathrm{Nb}} = 38\,\mathrm{GPa}$ [114]. As the shear modulus of Nb is larger than the one of BCC Ti, the threshold misfit for competitive strength is even smaller in Mo-Nb compared to Mo-Ti solid solutions.

5.8 Implications for Alloy Design

Based on these considerations, a correlation between misfit parameter and shear modulus is investigated with respect to the identified strength-controlling dislocation type, see Fig. 5.16. Misfit and shear modulus data for solid solutions from the Mo-Ti and the Mo-Nb systems investigated here (squares and upward triangles, respectively) as well as Nb-Ti (circle), W-Ta (downward triangle) and several MSS (star) from Ref. [13] are included. Alloys, which have been identified as having screw dislocation-controlled yield strength are shown in black, alloys with competitive strength in orange and alloys with edge dislocation-controlled strength in red.
Note that the misfit values published in Ref. [13] are obtained using the approximate formula $\Delta V_n = \sum_m x_m \, (V_n - V_{\text{alloy}})$, and thus might not be as precise as the ones calculated here using the exact formulae and the polynomial fits.
All shear moduli are calculated using $G_{\text{F}} = \sqrt{0.5\, C_{44}\, (C_{11} - C_{12})}$, and using concentration-weighted single crystal stiffnesses. All input values used for the data points in Fig. 5.16 are presented in Tabs. 5.5 and 5.6.

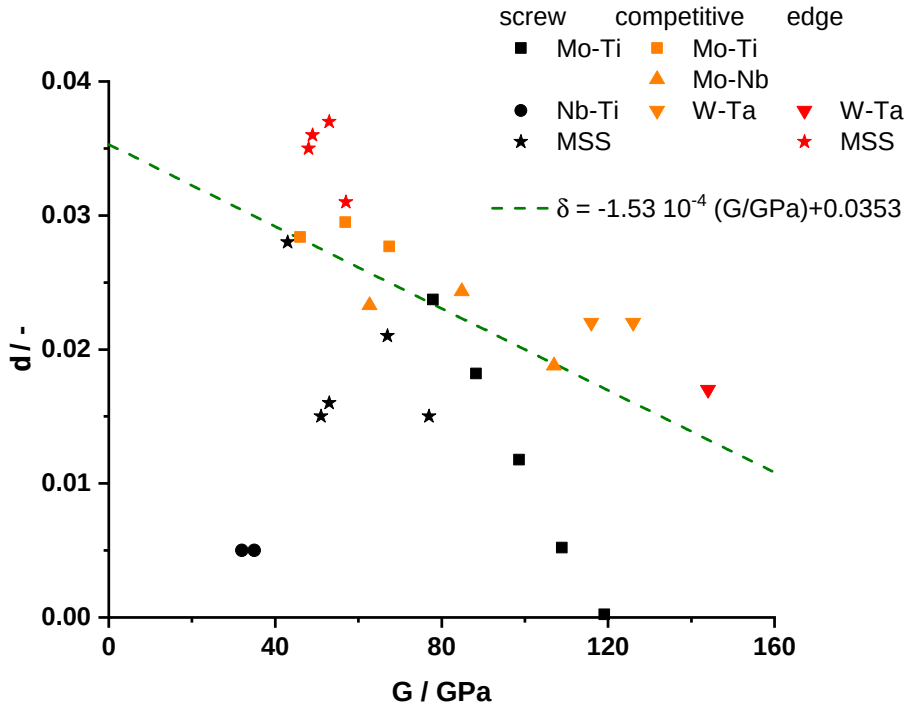

Figure 5.16: Misfit δ plotted over the shear modulus G for the solid solutions investigated here and in Ref. [13]. Different symbols indicate different alloy systems. Red symbols indicate solid solutions with clearly identified edge dislocation-controlled strength, orange symbols those with competitive strength from both dislocation types, black for clearly screw dislocation-controlled strength. The green dashed line indicates a proposed threshold function for competitive strength between both dislocation types.

The dashed green line in Fig. 5.16 indicates an estimated lower boundary for combinations of misfit δ and shear modulus G, above which edge dislocation strengthening becomes competitive. To determine this threshold, the alloys with lowest and highest shear modulus among own results, Mo-80Ti and Mo-25Nb, are used with $\delta_{\text{Mo-80Ti}} = 0.028$ and $G_{\text{Mo-80Ti}} = 46\,\text{GPa}$ and $\delta_{\text{Mo-25Nb}} = 0.019$ and $G_{\text{Mo-25Nb}} = 107\,\text{GPa}$, respectively. A linear function with

$$\delta = -1.53 \cdot 10^{-4}\,(G/\text{GPa}) + 0.0353 \tag{5.31}$$

is found. The reproduction of the already suggested threshold $\delta_{\text{th}} = 0.035$ as intercept of the function is coincidence. If Mo-75Nb was used as lower data point for the function instead, $\delta = 0.03$ would be obtained as intercept. The exact transition between screw and edge dislocation-controlled strength depends on several energy contributions in the screw dislocation model and elastic properties in the edge dislocation model. Thus, the phenomenological function presented here must be understood more as a guideline for competitive strengthening by edge dislocations than a strict transition value.

Table 5.5: The misfits δ and shear moduli G of all Mo-Ti and Mo-Nb solid solutions presented in this work, which are used in Fig. 5.16. The misfits are calculated using the polynomial fits for the lattice parameter in Eq. 4.1 and the exact formula given in Eq. 2.33. The shear moduli are calculated using the single crystal stiffnesses given in Tab. 5.1 and using Eq. 5.7. Note that the misfits are scaled by 1000 for better readability. The next row gives the solute-dislocation interaction energy parameter $\Delta\tilde{E}_{\text{p}}$, as calculated in the respective modellings. The final row indicates, if screw dislocations are predicted to control the strength ("S"), or if competitive strengthening by screw and edge dislocations was found ("C").

at% Ti	10	20	30	40	50	60	70	80
G / GPa	119	109	99	88	78	67	57	46
$1000\,\delta$ / -	0.2	5	12	18	24	28	30	28
$\Delta\tilde{E}_{\text{p}}$ / meV	45	60	69	74	75	74	69	60
strength	S	S	S	S	S	C	C	C
at% Nb	25	50	75					
G / GPa	107	85	63					
$1000\,\delta$ / -	19	25	23					
$\Delta\tilde{E}_{\text{p}}$ / meV	61	80	76					
strength	C	C	C					

Table 5.6: Alloy compositions, the misfits δ , the shear moduli G, and $\Delta\tilde{E}_\mathrm{p}$ for the alloys investigated in Ref. [13]. The final column indicates if the respective alloy was identified as being edge ("E") or screw dislocation-controlled ("S") or if competitive strength was found ("C"). The misfits are scaled by a factor of 1000 for better readability. The elemental inputs used are presented in Tab. 5.7.

Composition / at%	$1000\,\delta$ / -	G / GPa	$\Delta\tilde{E}_\mathrm{p}$ / meV	strength
W-50Ta	22	116	84	C
W-40Ta	22	126	79	C
W-20Ta	17	144	60	E
Ta-40Nb-18V	31	57	84	E
Ta-1Hf-9W	15	77	67	S
Nb-22.4Hf-5.9W	35	48	87	E
Nb-20Hf-6.4W-2.6Ta-2.6Zr	36	49	95	E
Nb-20Hf-9.2W-2.6Ta-2.6Zr	37	53	96	E
Nb-5.4Hf-2.6Ti-0.74Zr-0.26Ta-0.26W	28	43	56	S
Nb-50Ti	5	35	55	S
Nb-61Ti	5	32	65	S
Nb-18.1Ti-11.9Mo	15	51	83	S
Nb-18.1Ti-14.1Mo	16	53	87	S
Nb-32.5Ti-32.8Mo	21	67	108	S

Table 5.7: The BCC lattice parameters a and single crystal stiffnesses of the elements used in Ref. [13] to calculate the misfits δ using the linear approximation and the shear modulus using Eq. 5.7. Note that for Mo and Nb, different single crystal stiffnesses are used compared to the modelling in this work. The difference in G is $\approx 2 \ldots 3$ GPa for Mo and Nb. This data was originally compiled in Ref. [12] including Cr. Although none of the alloys contains Cr, it is shown here for the screening process described below.

Element	a / Å	C_{11} / GPa	C_{12} / GPa	C_{44} / GPa
W	3.16	533	205	163
Ta	3.3	266	158	87
Nb	3.3	253	133	31
V	3.03	232	119	46
Hf	3.56	131	103	45
Ti	3.26	134	110	36
Zr	3.58	104	93	38
Mo	3.14	450	173	125
Cr	2.91	350	68	100

Using Eq. 5.31, refractory metal alloys can be screened effectively for candidate systems with edge dislocation-controlled strength. Ref. [12] compiled data on the (partially extrapolated) BCC lattice parameters and single crystal stiffnesses for all nine stable elements of the fourth to sixth group of the periodic table (Ti, Zr, Hf, V, Nb, Ta, Cr, Mo, W). These values are presented in Tab. 5.7, as they are also used for the calculations in Ref. [13]. All $9 \cdot 8/2 = 36$ binary alloy systems are modelled using the edge dislocation model in increments of 10 at% using this data set.

For simplicity, alloy lattice parameters and misfits were calculated using the linear approximation for the volume misfit,

$$V_{\text{alloy}} = \sum_n x_n \, V_n \tag{5.32}$$

$$\Delta V_n = V_n - V_{\text{alloy}} \tag{5.33}$$

$$\delta = \frac{1}{3 \, V_{\text{alloy}}} \sqrt{\sum_n x_n \, (\Delta V_n)^2} \tag{5.34}$$

As this approach does not capture non-linear behavior of the lattice parameter, none of the Mo-Ti solid solutions would be considered edge dislocation-controlled in this simplified approach. Also, this screening does not consider the thermodynamically stable phases of the tested alloys.

Calculations for hard spheres predict solid solutions to form for misfit values $\delta_{\mathrm{BCC}} \leq 0.06$ [158]. This result can be confirmed for the refractory binary alloys using the SpringerMaterials database [159]. However, also below this threshold, each system needs to be analyzed individually. For example, Ti-Zr solid solutions fulfil the predicted misfit range for edge dislocation-controlled BCC solid solutions, but form HCP solid solutions at room temperature [160]. As this is true for all alloys from among the fourth group elements Ti, Zr and Hf, these combinations are excluded from the screening. For other systems, such a clear decision cannot be made. For example in Mo-Cr solid solutions, a separation in two BCC phases is predicted, which has not been observed in recent experiments [161]. Thus, all alloy systems except for those among fourth group elements are included. Results for the screening of binary alloys are presented in Fig. 5.17. Screw dislocation-controlled alloys are shown as black filled dots, edge dislocation-controlled alloys as red filled dots, and alloys above the threshold for stable BCC solid solutions are shown as empty black dots.

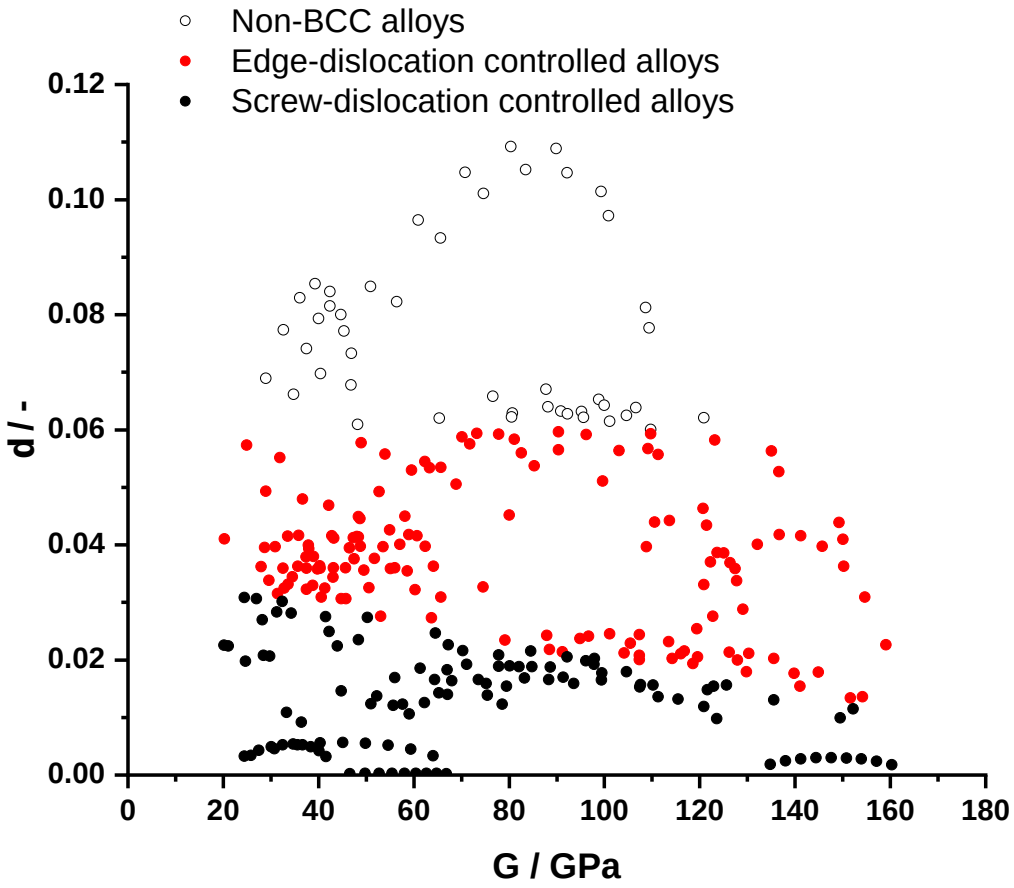

Figure 5.17: A screening of all possible binary solid solutions among refractory metals in increments of 10 at%. Solid black symbols are screw dislocation-controlled solid solutions, red symbols are edge dislocation-controlled. The alloys with the empty black symbols above $\delta = 0.06$ do not form BCC solid solutions. Alloys among fourth group elements are excluded as they form HCP solid solutions.

Alloys with the largest misfits are alloys containing Cr, Zr and Hf. The lattice parameter of Cr is the smallest of all refractory metals (a_{Cr} =2.91 Å, all data in this paragraph from Ref. [12]), while the extrapolated BCC lattice parameters of Zr and Hf are the largest, a_{Zr} =3.58 Å and a_{Hf} =3.56 Å, respectively. Due to the extreme values of lattice parameters, the according misfits are large in their alloys. From the alloys screened, a total of 46 compositions have misfits larger than the BCC stability threshold. 22 compositions contain Cr, 22 Zr and 18 Hf. Note that this includes alloys between these elements, thus the total of the numbers is larger than 46. Also among solid solutions with a large misfit, $0.04 < \delta < 0.06$, most contain Cr, Zr and Hf with 22, 22 and 19 out of 66, respectively. This makes these elements the most promising ones for edge dislocation-controlled strength in BCC solid solutions, if BCC solid solutions can be obtained.

In contrast to the modulus-independent threshold from Ref. [13], additional alloys can now be identified as likely edge dislocation-controlled. In total, 55 out of 157 alloys are below the threshold of 0.035, but have a sufficiently large moduli to cross the threshold function from Eq. 5.31. Accordingly, W and Mo, the metals with the largest shear moduli, are the most common components among those alloys (20 and 18 alloys, respectively).

The threshold function is found for binary alloys, however the Maresca-Curtin models have been developed for systems with an arbitrary number of constituents. Based on the limited number of data points available for Fig. 5.16, MSS also follow the suggested function. While the lattice parameter and, consequently, also the misfit volume can be accurately described by concentration-dependent functions for binary solid solutions, linear approximations of lattice parameters and misfit volumes are commonly used for the modelling of MSS [5, 11, 12, 13, 162] and have been found experimentally [9]. The same approximations have been used in the screening of binary alloys. Elastic properties are estimated from the concentration weighted single crystal stiffnesses. Even when alloys are considered that contain elements not included here, for example Al-containing MSS [59], shear moduli and lattice parameters can be obtained via independent experimental methods, and the model can be applied accordingly. Thus, regarding the edge dislocation model, there are no additional considerations necessary to transfer the threshold function to MSS or alloys containing non-refractory metals. Similarly, the energy contributions to form self-interstitials, vacancies and kink pairs are obtained as concentration weighted averages of the elemental properties, both for binary as well as for MSS. The limits of these quantities are solely determined by the elemental values, and no further complexity arises with an increasing number of constituents. Thus, the strength contribution from cross-kink breaking in the model for screw dislocation-controlled strength also can readily be calculated for MSS.

A final contribution that needs to be considered is the interaction energy $\Delta\tilde{E}_\mathrm{p}$. For Mo-25Nb and Mo-80Ti, the anchoring points of the threshold function, $\Delta\tilde{E}_{\mathrm{p,25Nb}} = 61\,\mathrm{meV}$ and $\Delta\tilde{E}_{\mathrm{p,25Nb}} = 60\,\mathrm{meV}$ are found. Values from Ref. [13] for alloys with competitive strengthening were $\Delta\tilde{E}_{\mathrm{p,W\text{-}50Ta}} = 84\,\mathrm{meV}$ and $\Delta\tilde{E}_{\mathrm{p,W\text{-}40Ta}} = 79\,\mathrm{meV}$. The alloy W-20Ta with $\Delta\tilde{E}_{\mathrm{p,W\text{-}20Ta}} = 60\,\mathrm{meV}$ was identified as edge dislocation-controlled. On the other hand, Nb-50Ti was identified as screw dislocation-controlled with a value of $\Delta\tilde{E}_{\mathrm{p,Nb\text{-}50Ti}} = 55\,\mathrm{meV}$. Thus, based solely on the dislocation-solute interaction energy, no clear trend for either dislocation type can be observed for binary solid solutions. This situation is similar for MSS: In Ref. [13], two MSS of the Nb-Hf-W-Ta-Zr system are identified as edge dislocation-controlled with $\Delta\tilde{E}_\mathrm{p}$-values of 95 and 96 meV. One alloy of the Nb-Hf-Ti-W-Ta-Zr system is identified as screw dislocation-controlled with a $\Delta\tilde{E}_\mathrm{p}$-value of 56 meV. Again, no trend is observed. Thus, based on the currently available data, the screw-to-edge dislocation-controlled threshold can not be reliably estimated using $\Delta\tilde{E}_\mathrm{p}$. This supports the approach to determine the threshold using parameters from the edge dislocation model. With a larger number of available data sets or theoretical progress to correlate the interaction energy to other material properties, patterns might emerge, which then might allow to properly distinguish screw and edge dislocation-controlled strength including this parameter.

6 Conclusions

Two questions have been stated in the introduction of this work:

- Is it possible to identify a transition between screw and edge dislocation-controlled yield strength in BCC solid solutions?
- Do the observations allow the derivation of general guidelines for this transition?

To answer these, Mo-Ti and Mo-Nb solid solutions have been investigated experimentally, and the results have been correlated to available models of solid solution strengthening. Indeed, a transition between both dislocation types as strength-controlling has been found, and the results yield a generalized correlation for arbitrary BCC solid solutions.

Both systems have been thoroughly characterized across several length scales. Very good correlations of nanoindentation, Vickers hardness and compression testing are obtained in both systems, indicating no significant impact of grain size, oxide formation or grain orientation on the yield strength. The combination of HCGE and APT reveals up to 0.4 at% interstitial O in the Mo-Ti solid solutions with high Ti contents. Two different model-consistent approaches are applied to account for the strengthening contributions from interstitial O. For Mo-Nb solid solutions, no correction is required as O contents are below detection limit. X-ray diffraction measurements confirm a single-phase BCC structure for all alloys and two distinct behaviors: While the lattice parameters in Mo-Nb solid solutions increases approximately linearly with increasing Nb content, the lattice parameters in Mo-Ti increases non-linearly. The slope of the lattice parameter function quantifies the atomic misfit, which is an important contribution to edge dislocation-controlled strength.

Different established models have been applied to model the yield strength controlled by screw and edge dislocations in both systems. Although the Labusch model is still used today, there are fundamental problems in the application to BCC solid solutions. Accordingly, no reasonable results are obtained using this model. The Suzuki model, including recent changes, models the strength solely controlled by screw dislocations. Its mathematical complexity results in the necessity to use numerical solving methods, and, as a result, different modelling results by different authors. However, the strength in both solid solution series can be reproduced in this model using the solving approach presented here. The screw dislocation strengthening model by Maresca and Curtin can be solved analytically, and also models the strength in both systems. However, both screw dislocation models require the use of interaction energy parameters which have to be obtained either by DFT calculations or by fitting the data to the experimental results. The edge dislocation model by Maresca and Curtin is specifically developed for BCC solid solutions and can be solved analytically. Its input parameters can be obtained by independent experimental methods, thus no fitting of the model is required. It reveals that the strong change in slope in the Mo-Ti lattice parameter function results in a competitive strength by edge dislocation motion compared to screw dislocations. However, also in Mo-Nb solid solutions, with a smaller slope in the function, competitive strength by edge dislocation motion is obtained for all tested concentrations.

Based on the obtained results on competitive strengthening by both dislocation types in Mo-Ti and Mo-Nb, a generalization is proposed: Assuming that a general misfit threshold must be surpassed to obtain competitive edge dislocation strengthening, a linear dependency on the shear modulus is found. Based on this relation, all binary solid solutions of refractory metals can be screened, and 62% of the solid solutions might be edge dislocation-controlled. As the Maresca-Curtin models are developed for systems with arbitrary numbers of constituent elements, the threshold function holds also for MSS. Based on these results, the selection of the models used for solid solution strengthening can be refined vastly, leading to a faster and more reliable alloy design.

However, the identification of edge dislocation-controlled solid solutions and the following derivation are based exclusively on model comparison. Experimental proof, for example using dislocation character analyses in TEM have been successfully applied to MSS, where edge dislocations have been found as predominant dislocation type [10, 12]. A similar analysis is not yet available in binary solid solutions. Thus, no data are available that confirm (or falsify) the determined threshold function for competitive screw and edge dislocations. The function is found using Mo-80Ti and Mo-25Nb solid solutions, and accordingly both screw and edge dislocation are expected in these alloys. However, binary alloys with larger misfit-shear modulus combination, for example solid solutions of Mo or W with Zr or Hf, might be a better starting point for TEM analyses. So far, proof for edge dislocation-controlled strength in binary solid solutions is missing in the first place, and these solid solutions are more promising due to their larger misfit than Mo-Ti and Mo-Nb solid solutions.

If this threshold is confirmed experimentally, the found function allows for more precise design of BCC alloys: For good mechanical stability at high-temperatures, high-melting point refractory metals (e.g., W and Ta) are desired. However, these come with the downside of high densities. By contrast, low-melting point refractory metals (e.g. Ti, Cr) also have lower densities and are desired for increased engine efficiency. Using the threshold function described here, computer-assisted alloy design can be improved regarding finding a compositional balance between the yield strength and density.

Besides the use of substitutional solutes, interstitials might also be used to adjust the strength-controlling dislocation type. As interstitials cause large local lattice strains, a transition from screw to edge dislocation-controlled strength might thus also be triggered by interstitial content. Mo-50Ti is a promising alloy for an investigation of this phenomenon as it is already close to competitive strengthening, making edge dislocation motion very sensitive to additional misfit contributions. The selection of interstitial atoms however requires some additional preliminary investigation in order to avoid evaporation or precipitation of metal-interstitial compounds.

The application of the models, especially of the screw dislocation strengthening models is restricted to a small number of research groups due to their complexity and the need for DFT calculated energy values. While the model code used in this work cannot provide support on DFT calculations, it allows to apply the models either by fitting the model to experimental data or by using published energy parameters as input. The code is commented thoroughly so that adaptation to different model systems can easily be made. Additional theoretical work is required to derive methods for predicting the solute-dislocation interaction energy without the need of DFT calculations to open up this topic of research for more researchers.

7 Appendix

7.1 Compression Testing Data

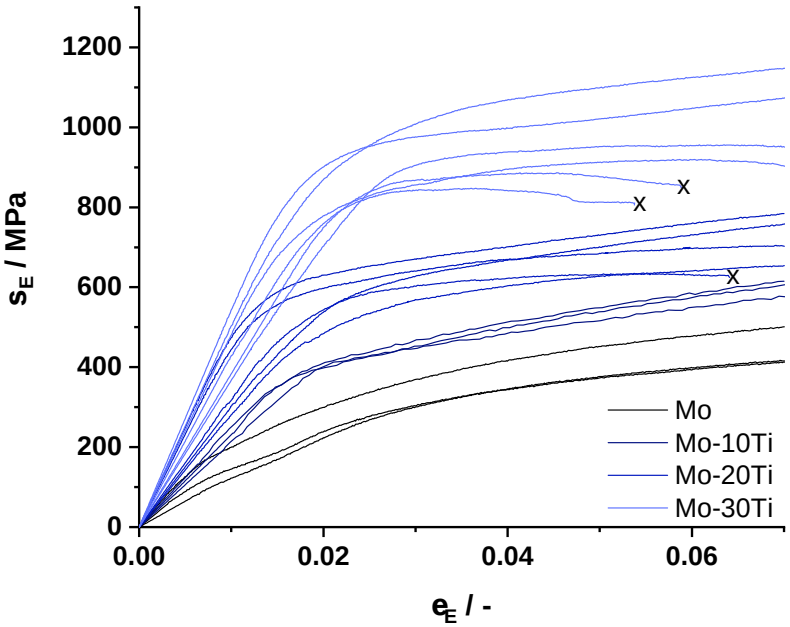

Figure 7.1: Engineering stress-strain data for all Ti-lean Mo-Ti solid solutions. Data marked with "x" indicate sample failure.

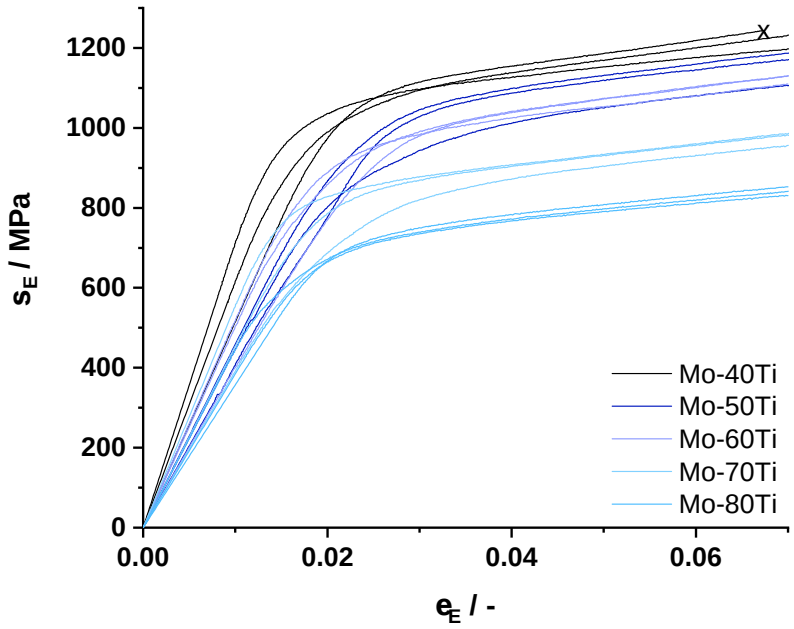

Figure 7.2: Engineering stress-strain data for all Ti-rich Mo-Ti solid solutions. Data marked with "x" indicate sample failure.

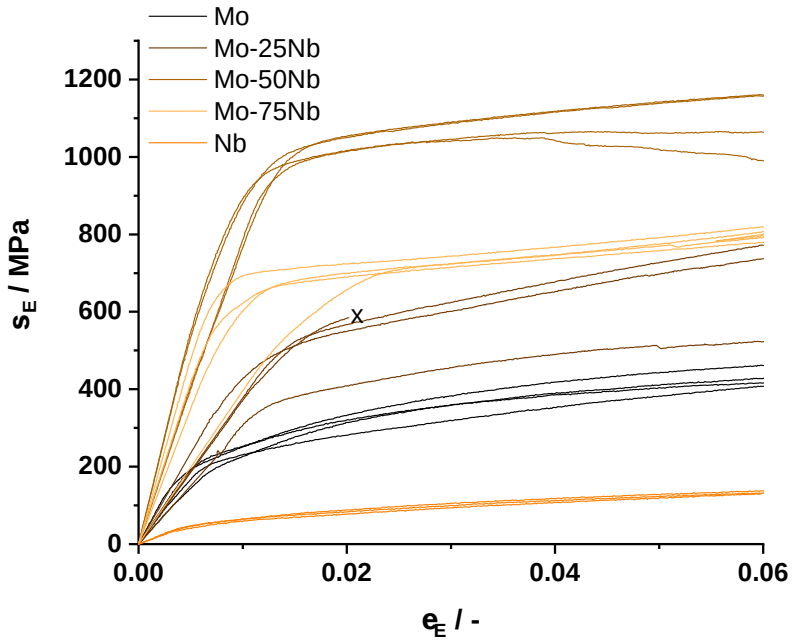

Figure 7.3: Engineering stress-strain data for all Mo-Nb solid solutions. Data marked with "x" indicate sample failure.

7.2 Nanoindentation Data

On the following pages, the data obtained in nanoindentation is presented. For each alloy, the load-displacement data is shown as large image, while the therefrom derived Young's modulus and nanohardness data are shown as smaller images. Note that the established colour coding is not maintained in this section.

7.2.1 Mo-Ti solid solutions

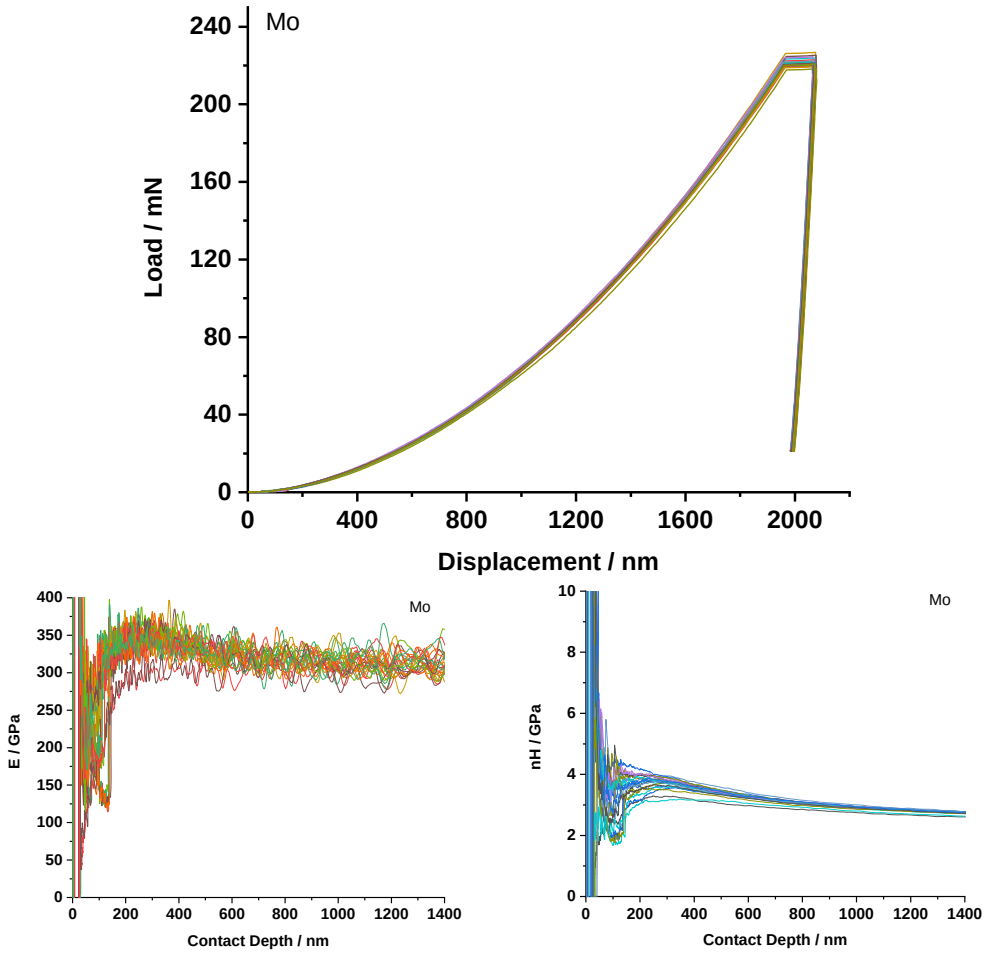

Figure 7.4: Load-displacement (top) and Young's modulus and nanohardness data (bottom) for Mo in Mo-Ti solid solutions.

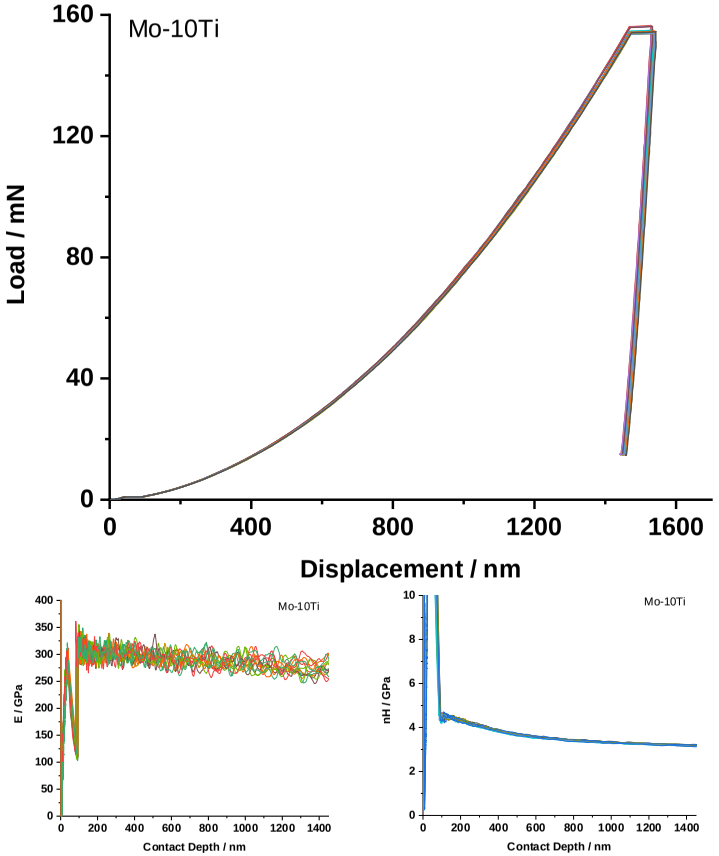

Figure 7.5: Load-displacement (top) and Young's modulus and nanohardness data (bottom) for Mo-10Ti solid solutions.

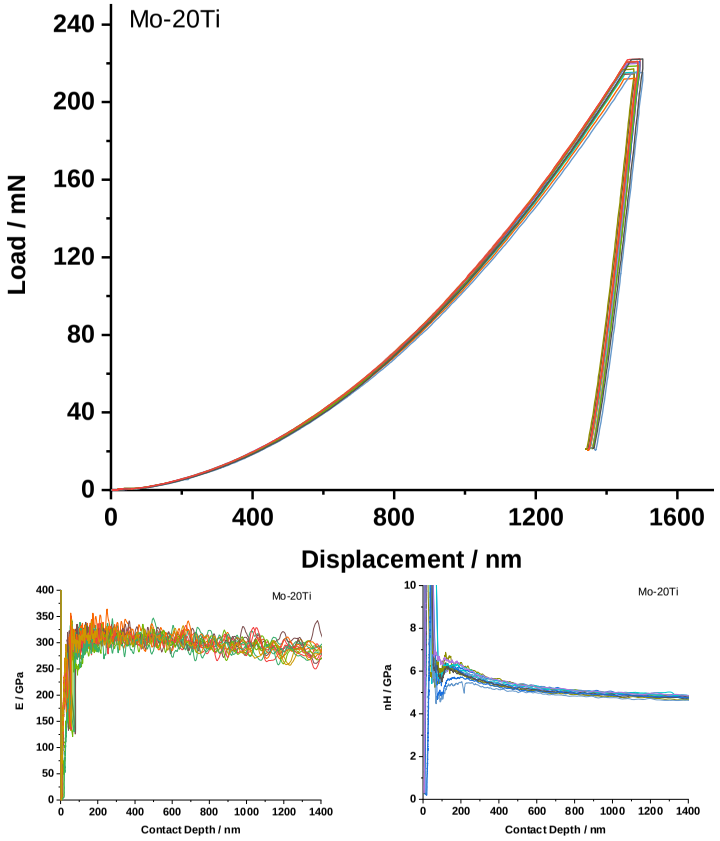

Figure 7.6: Load-displacement (top) and Young's modulus and nanohardness data (bottom) for Mo-20Ti solid solutions.

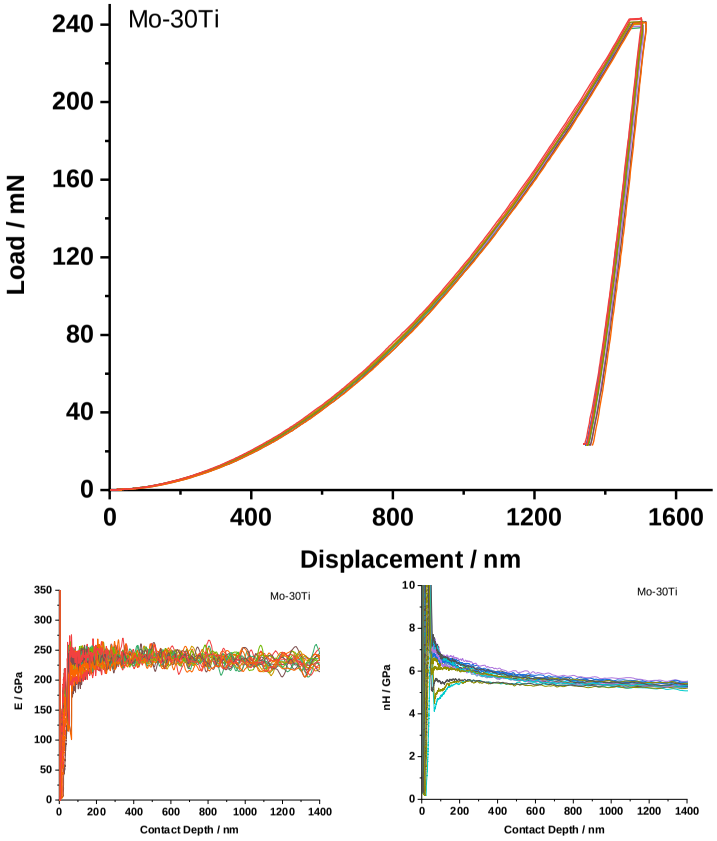

Figure 7.7: Load-displacement (top) and Young's modulus and nanohardness data (bottom) for Mo-30Ti solid solutions.

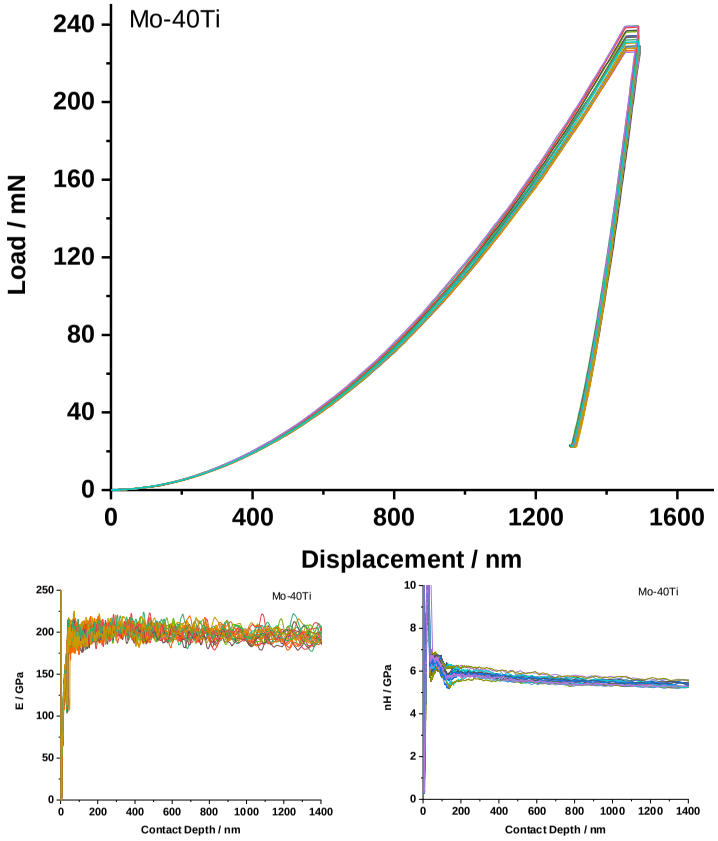

Figure 7.8: Load-displacement (top) and Young's modulus and nanohardness data (bottom) for Mo-40Ti solid solutions.

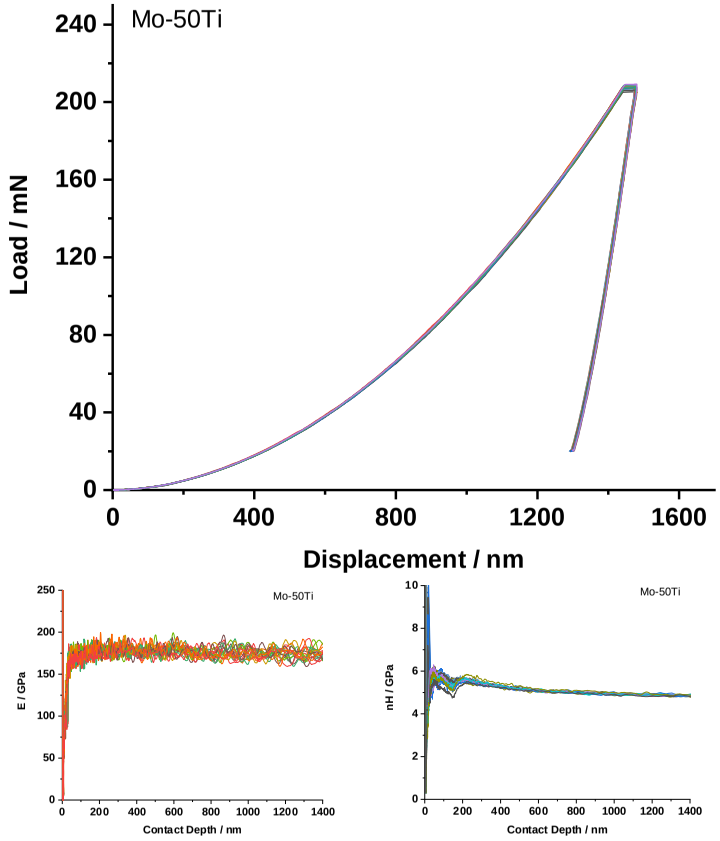

Figure 7.9: Load-displacement (top) and Young's modulus and nanohardness data (bottom) for Mo-50Ti solid solutions.

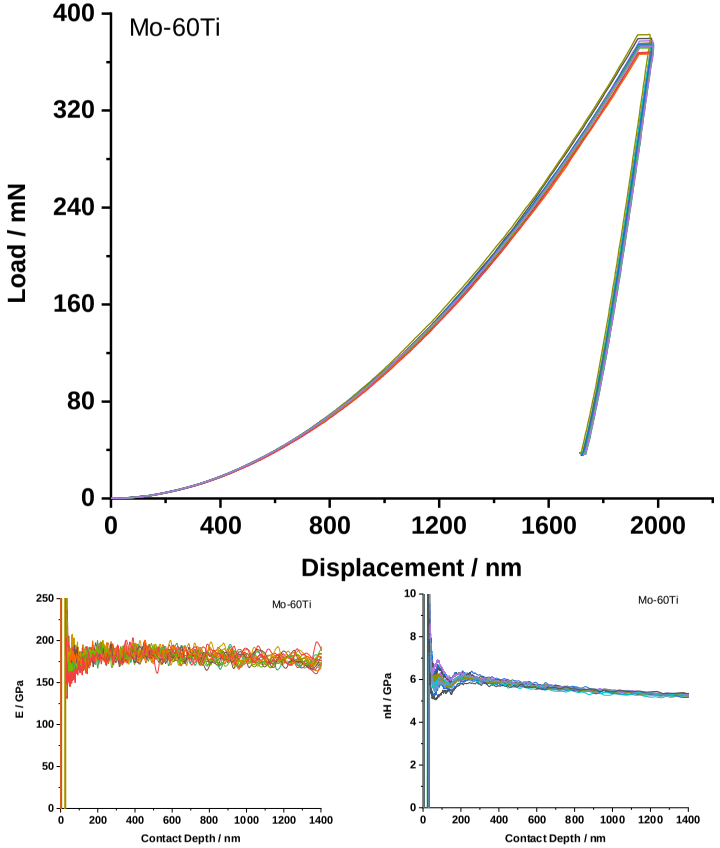

Figure 7.10: Load-displacement (top) and Young's modulus and nanohardness data (bottom) for Mo-60Ti solid solutions.

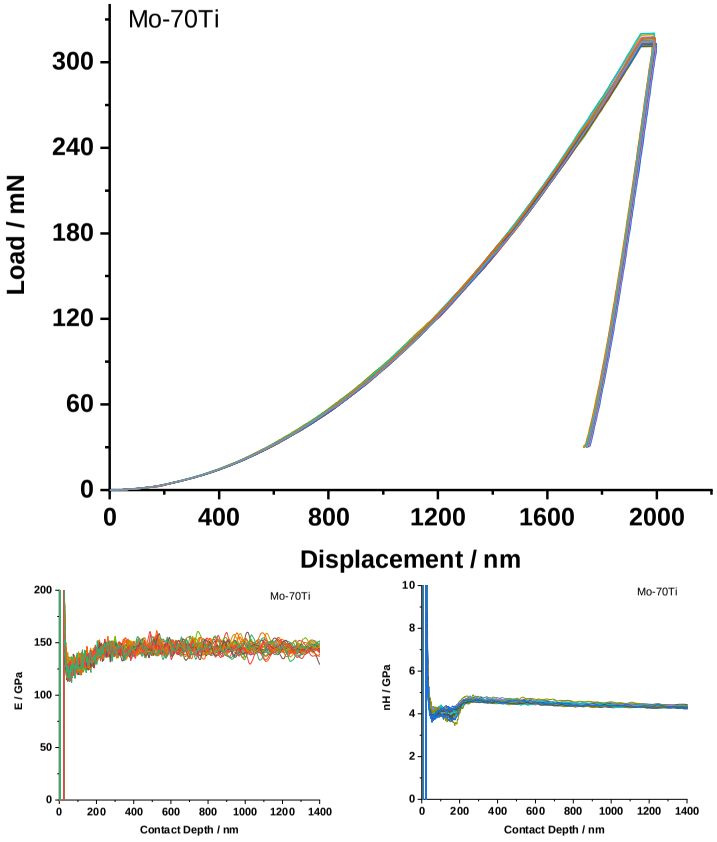

Figure 7.11: Load-displacement (top) and Young's modulus and nanohardness data (bottom) for Mo-70Ti solid solutions.

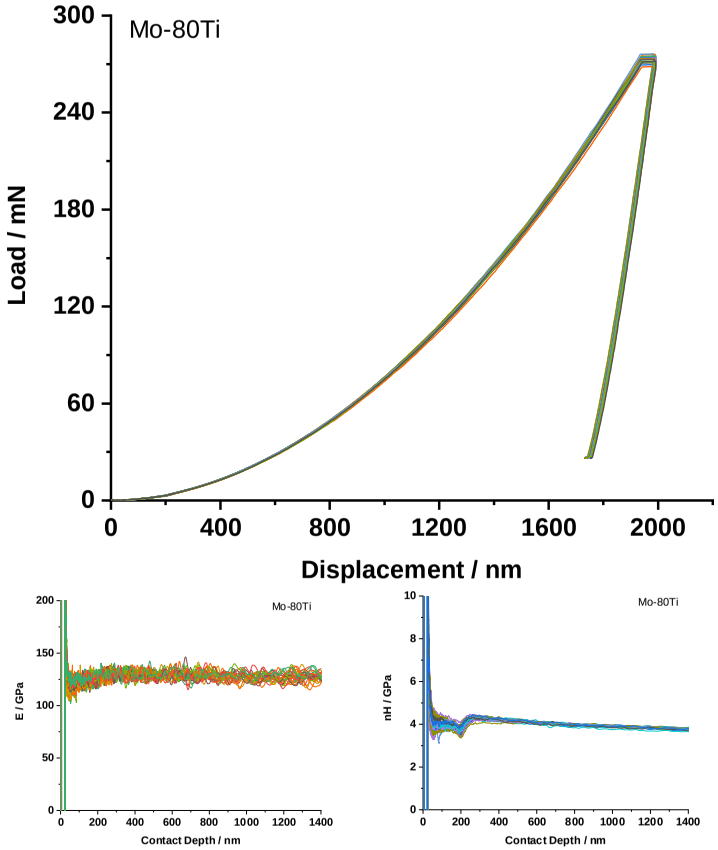

Figure 7.12: Load-displacement (top) and Young's modulus and nanohardness data (bottom) for Mo-80Ti solid solutions.

7.2.2 Mo-Nb solid solutions

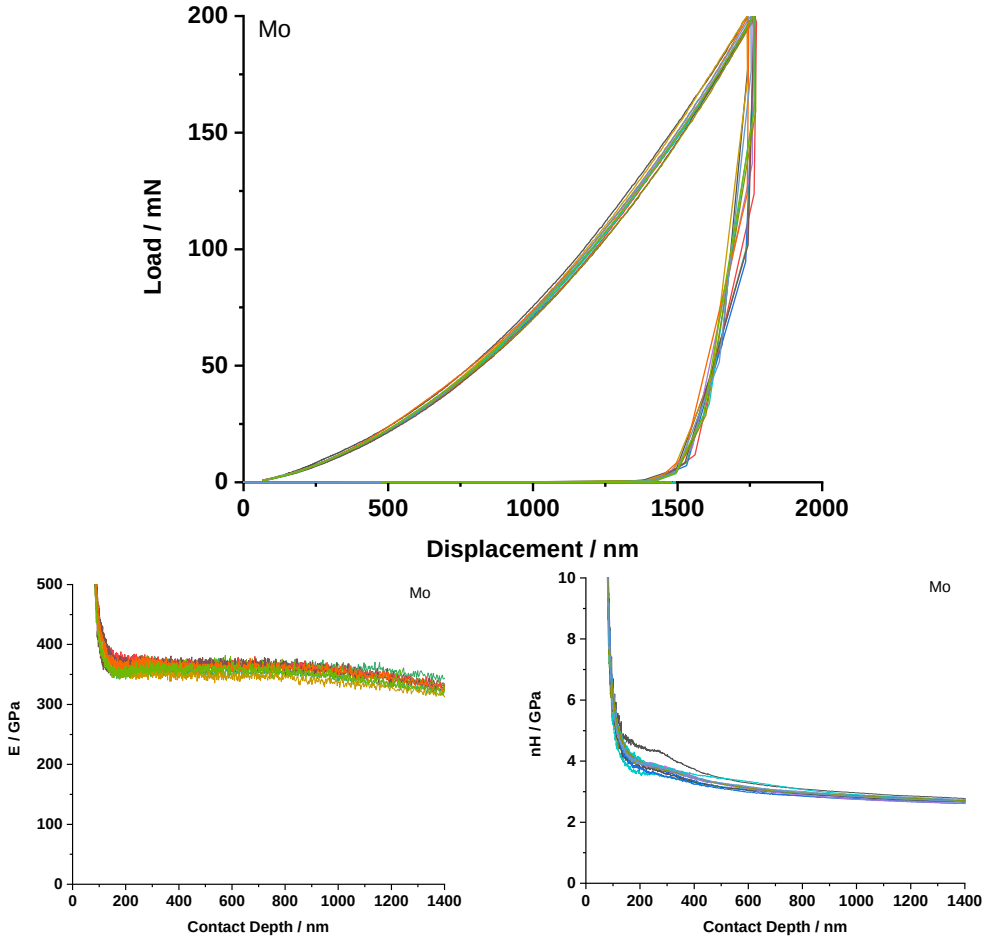

Figure 7.13: Load-displacement (top) and Young's modulus and nanohardness data (bottom) for Mo in Mo-Nb solid solutions.

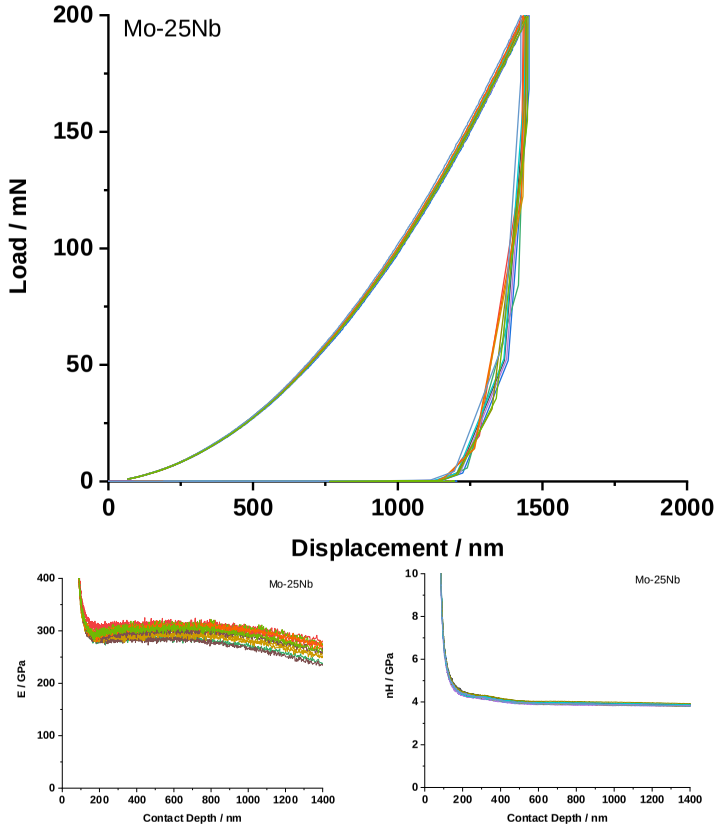

Figure 7.14: Load-displacement (top) and Young's modulus and nanohardness data (bottom) for Mo-25Nb solid solutions.

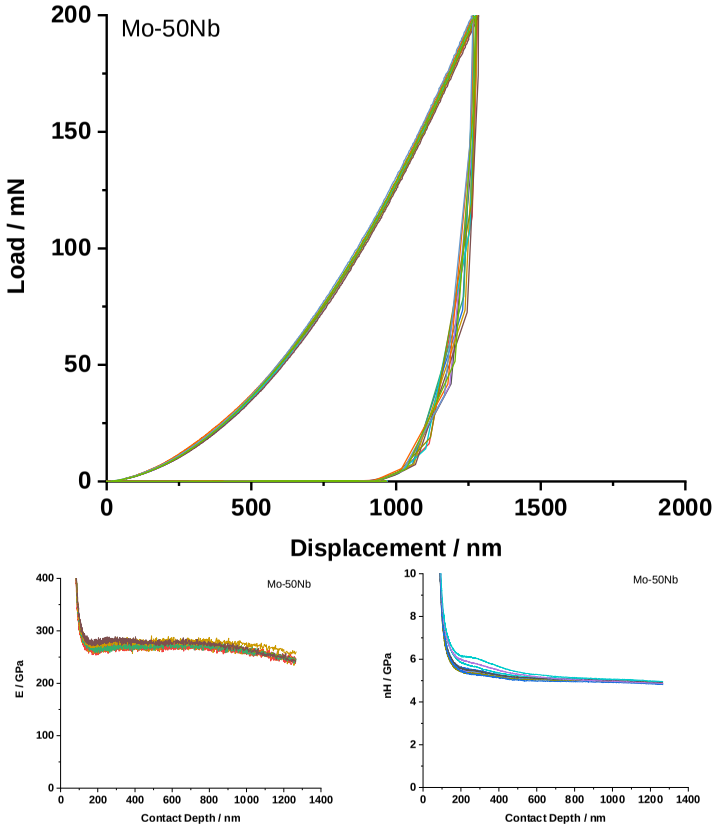

Figure 7.15: Load-displacement (top) and Young's modulus and nanohardness data (bottom) for Mo-50Nb solid solutions.

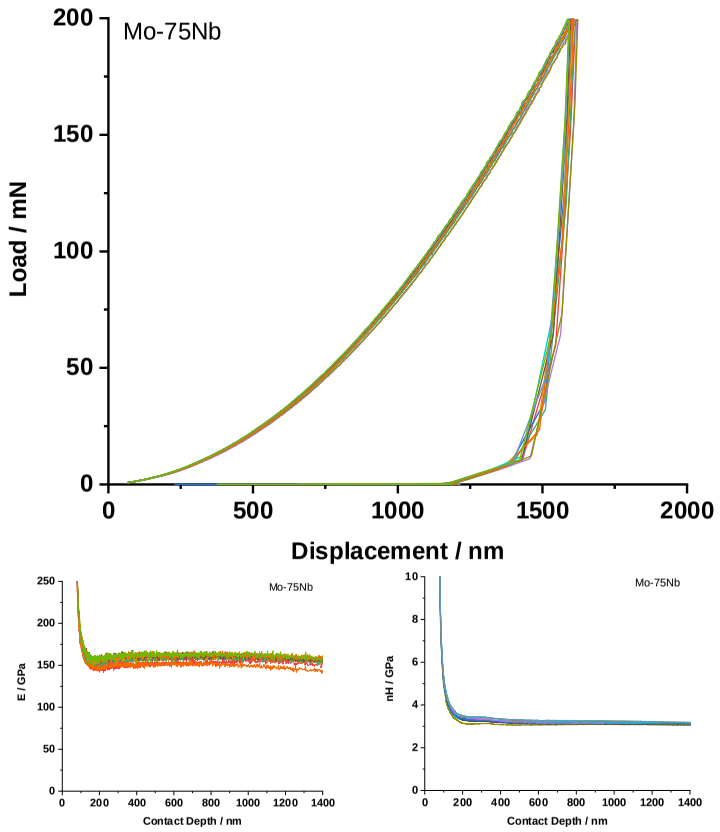

Figure 7.16: Load-displacement (top) and Young's modulus and nanohardness data (bottom) for Mo-75Nb solid solutions.

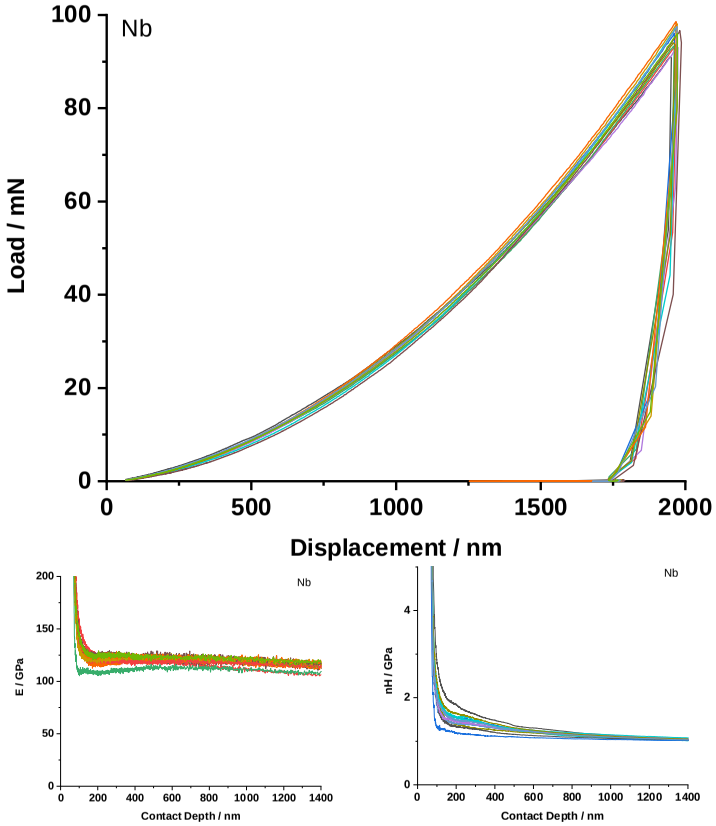

Figure 7.17: Load-displacement (top) and Young's modulus and nanohardness data (bottom) for Nb in the Mo-Nb solid solutions.

8 Acknowledgements

This work would not have been possible without the help and support by many people, which I want to thank here briefly.
First of all I thank Prof. Heilmaier and Prof. Schwaiger for accepting me as doctoral student. This thesis would not have been successful without their constant support, both regarding the freedom as well as guidelines needed to shape this project into its final form. Especially the circumstances introduced by the pandemic and the uncommon supervision structure required some flexibility to bring this thesis to a successful end. I also thank Prof. Kirchlechner for his assessment of and valuable input to the thesis on short notice.
Of course, this successful end would not have been possible without the constant support by Alexander Kauffmann and insistent challenge to improve myself, my research and this thesis to their best possible versions.
I want to thank also my other colleagues from the Physical Metallurgy group for their constant support, especially Frauke and Chitto as well as Adi and Stephan, but also Hans, Sascha, Cami, Susanne, Daniel, Marcel, Lars, Gabriely, Sandipan, Sri and Liu.
Also, I want to thank my colleagues from IEK-2 for their support. Here, Jin, Steffen and Nico must be mentioned first, but also Silva, Velislava, Taegeon and Nobu and everyone else who joined during my time as doctoral student.
I also would like to thank the DFG for the financial support of the GRK 2561, which allowed us to form this close group of colleagues and even friends, especially Nathalie, Andreas, Katharina and Nils, but also everyone else of the first and second cohort. Additionally, I want to thank all the other people who supported my work; the technicians in the mechanical workshop, metallography and laboratories in Karlsruhe and Jülich, the team of Dr. Bergfeldt at IAM-AWP for a lot of chemical analyses, as well as my students, assistants, and interns, Johannes, Isabelle and Karl, Anna and Max. I also have to thank Carol, You and Prof. Curtin for the insightful discussions about the modelling.
Finally, for their support throughout this time (even at a distance, and even with social distancing), my family and friends from all across Europe. It would not have been possible without you.
A final thank you has to go to Dr. Douglas Capp, who, situated in Australia, did not hesitate to provide the necessary documents, hastily handwritten, to obtain his PhD thesis.

List of Publications

- **Winkens, Georg**; Kauffmann, Alexander; Herrmann, Johannes; Czerny, Andreas K.; Obert, Susanne; Seils, Sascha; Boll, Torben; Baruffi, Carolina; Rao, You; Curtin, William A.; Schwaiger, Ruth; Heilmaier, Martin, *The influence of lattice misfit on screw and edge dislocation-controlled solid solution strengthening in Mo-Ti alloys*, Communications Materials **4** (2023), 26, DOI: 10.1038/s43246-023-00353-8.
  Own contribution: Data acquisition, analysis, visualization; Modelling; Writing and finalization of the draft.

- Tirunilai, Aditya Srinivasan; Hinrichs, Frauke; Schliephake, Daniel; Engstler, Michael; Mücklich, Frank; Obert, Susanne; **Winkens, Georg**; Kauffmann, Alexander; Heilmaier, Martin, *Phase Continuity, Brittle to Ductile Transition Temperature, and Creep Behavior of a Eutectic Mo–20Si–52.8Ti Alloy*, Advanced Engineering Materials **24** (2022), 2200918, DOI: 10.1002/adem.202200918.
  Own contribution: Data acquisition and analysis; Editing of the draft.

- Hinrichs, Frauke; Kauffmann, Alexander; Tirunilai, Aditya Srinivasan; Schliephake, Daniel; Beichert, Bonita; **Winkens, Georg**; Beck, Katharina; Ulrich, Anke Silvia; Galetz, Mathias Christian; Long, Zhongmin; Thota, Hemanth; Eggeler, Yolita; Pundt, Astrid; Heilmaier, Martin, *A novel nitridation- and pesting-resistant Cr-Si-Mo alloy*, Corrosion Science **207** (2022), 110566, DOI: 10.1016/j.corsci.2022.110566.
  Own contribution: Data analysis, Editing of the draft.

- Nathalie Thor, **Georg Winkens**, Jan Bernauer, Nils-Christian Petry, Katharina Beck, Jin Wang, Ruth Schwaiger, Ralf Riedel, Ute Kolb, Maren Lepple, Astrid Pundt, *Microstructure Characterization and Mechanical Properties of Polymer-Derived HfxTa(1-x))C/SiC Ceramic Prepared upon Field-Assisted Sintering Technique/Spark Plasma Sintering*, Advanced Engineering Materials **26** (2024), 17, 2301841, DOI: 10.1002/adem.202301841.
  Own contribution: Data analysis; Editing of the draft.

- Stephan Laube; **Georg Winkens**; Alexander Kauffmann; Juan Li; Christoph Kirchlechner; Martin Heilmaier, *Strength of Disordered and Ordered Al-Containing Refractory High-Entropy Alloys*, Advanced Engineering Materials **26** (2024), 17, 2301797, DOI: 10.1002/adem.202301797.
  Own contribution: Modelling; Editing of the draft.

List of Figures

1.1 Yield strength of refractory metal solid solutions and Ni-based superalloys. . . . 2

2.1 Concept of the Peierls barrier. . . . 5
2.2 Comparison of yield strength for Mo and Ni. . . . 6
2.3 Differential displacements around a screw dislocation. . . . 7
2.4 Kink pair formation principle. . . . 8
2.5 Fleischer model concept. . . . 11
2.6 Labusch model concept. . . . 13
2.7 Suzuki model concept. . . . 15
2.8 Interaction energy in the Suzuki model. . . . 19
2.9 Maresca-Curtin screw model concept. . . . 24
2.10 Cross-kink breaking by loop formation. . . . 25

3.1 Operation principle of ICP-OES. . . . 32
3.2 APT tip. . . . 33
3.3 Operation principle of APT. . . . 35
3.4 Measurement principles of nanoindentation. . . . 38
3.5 Length scales in Nanoindentation. . . . 39
3.6 CSM measurement principle 41
3.7 Vickers indent in Nb. . . . 42
3.8 Analysis principle for stress-strain data. . . . 44

4.1 Microstructures of Mo-Nb solid solutions. . . . 46
4.2 Microstructures of Mo-Ti solid solutions. . . . 46
4.3 Diffraction patterns. . . . 48
4.4 Mo-Ti phase diagram. . . . 49
4.5 O contents in alloys and raw materials. . . . 51
4.6 Lattice parameters and fits. . . . 53
4.7 Misfit parameters for both systems. . . . 55
4.8 Indentation moduli for both systems. . . . 56
4.9 H and nH in Mo-Ti. . . . 57
4.10 H and nH in Mo-Nb. . . . 58
4.11 Offset yield strength in Mo-Ti. . . . 59
4.12 Offset yield strength in Mo-Nb. . . . 60
4.13 Correlations of mechanical properties in Mo-Ti. . . . 62
4.14 Correlations of mechanical properties in Mo-Nb. . . . 63

5.1 Comparison of methods to calculate E. . . . 67
5.2 Single crystal stiffnesses in Mo-Nb solid solutions. . . . 68

5.3 Indentation and Young's modulus in Mo-Nb. 69
5.4 Experimental indentation and modelled Young's moduli. 70
5.5 Vickers hardness in Ti-9Mo and model fits. 72
5.6 Offset yield strength corrected for interstitial O. 73
5.7 Results of the Labusch modelling in Mo-Ti. 76
5.8 Results of the Suzuki modelling in Mo-Ti. 81
5.9 Results of the Suzuki modelling in Mo-Nb. 81
5.10 Different Suzuki implementations for Mo-Nb. 84
5.11 Different Suzuki implementations for Mo-Ti. 85
5.12 Optimized energy parameter for the Suzuki model in Mo-Ti. 87
5.13 Results of the Maresca-Curtin modellings in Mo-Nb. 89
5.14 Results of the Maresca-Curtin modellings in Mo-Ti. 90
5.15 Summary of the modelling results in Mo-Ti and Mo-Nb. 96
5.16 Plot for δ over G. 99
5.17 Screening of binary refractory alloys. 103

7.1 Stress-strain data for Ti-lean solid solutions. 109
7.2 Stress-strain data for Ti-rich solid solutions. 110
7.3 Stress-strain data for Mo-Nb solid solutions. 110
7.4 Nanoindentation of Mo. 111
7.5 Nanoindentation of Mo-10Ti. 112
7.6 Nanoindentation of Mo-20Ti. 112
7.7 Nanoindentation of Mo-30Ti. 113
7.8 Nanoindentation of Mo-40Ti. 113
7.9 Nanoindentation of Mo-50Ti. 114
7.10 Nanoindentation of Mo-60Ti. 114
7.11 Nanoindentation of Mo-70Ti. 115
7.12 Nanoindentation of Mo-80Ti. 115
7.13 Nanoindentation of Mo. 116
7.14 Nanoindentation of Mo-25Nb. 117
7.15 Nanoindentation of Mo-50Nb. 117
7.16 Nanoindentation of Mo-75Nb. 118
7.17 Nanoindentation of Nb. 118

List of Tables

3.1 Raw elements used in synthesis. 29
3.2 Metallographic preparation steps. 30

4.1 Chemical compositions. 50

5.1 Single crystal stiffnesses. 66
5.2 Parameters used in the Suzuki model. 79
5.3 Solute-dislocation interaction energies used in the Suzuki model. . . . 79
5.4 Self-interstitial, vacancy and kink formation energies. 91
5.5 Misfits, shear moduli and $\Delta\tilde{E}_{\mathrm{p}}$ of Mo-Ti and Mo-Nb. 100
5.6 Alloy data calculated in Ref. [13]. 101
5.7 Input parameters used in Ref. [13]. 102

Bibliography

[1] D. B. Miracle and O. N. Senkov, "A critical review of high entropy alloys and related concepts," *Acta Materialia*, vol. 122, pp. 448–511, 2017.

[2] D. F. Paulonis and J. J. Schirra, "Alloy 718 at Pratt & Whitney: Historical Perspective and Future Challenges," in *Superalloys 718, 625, 706 and Various Derivatives (2001)*, pp. 13–23, TMS, 6/17/2001 - 6/20/2001.

[3] W. Xia, X. Zhao, L. Yue, and Z. Zhang, "A review of composition evolution in Ni-based single crystal superalloys," *Journal of Materials Science & Technology*, vol. 44, pp. 76–95, 2020.

[4] O. N. Senkov, G. B. Wilks, J. M. Scott, and D. B. Miracle, "Mechanical properties of Nb25Mo25Ta25W25 and V20Nb20Mo20Ta20W20 refractory high entropy alloys," *Intermetallics*, vol. 19, no. 5, pp. 698–706, 2011.

[5] Y. Rao, C. Baruffi, A. de Luca, C. Leinenbach, and W. A. Curtin, "Theory-guided design of high-strength, high-melting point, ductile, low-density, single-phase BCC high entropy alloys," *Acta Materialia*, vol. 237, no. 5, p. 118132, 2022.

[6] W. A. Curtin, S. I. Rao, and C. Woodward, "Progress and challenges in the theory and modeling of complex concentrated alloys," *MRS Bulletin*, vol. 47, no. 2, pp. 151–157, 2022.

[7] B. Šesták and A. Seeger, "Gleitung und Verfestigung in kubisch-raumzentrierten Metallen und Legierungen," *Zeitschrift für Metallkunde*, vol. 69, no. 4, pp. 195–202, 1978.

[8] A. S. Argon, *Strengthening mechanisms in crystal plasticity*, vol. 4 of *Oxford materials*. Oxford: Oxford Univ. Press, 2008.

[9] H. Chen, A. Kauffmann, S. Laube, I.-C. Choi, R. Schwaiger, Y. Huang, K. Lichtenberg, F. Müller, B. Gorr, H.-J. Christ, and M. Heilmaier, "Contribution of Lattice Distortion to Solid Solution Strengthening in a Series of Refractory High Entropy Alloys," *Metallurgical and Materials Transactions A*, vol. 49, no. 3, pp. 772–781, 2018.

[10] F. Wang, G. H. Balbus, S. Xu, Y. Su, J. Shin, P. F. Rottmann, K. E. Knipling, J.-C. Stinville, L. H. Mills, O. N. Senkov, I. J. Beyerlein, T. M. Pollock, and D. S. Gianola, "Multiplicity of dislocation pathways in a refractory multiprincipal element alloy," *Science*, vol. 370, no. 6512, pp. 95–101, 2020.

[11] F. Maresca and W. A. Curtin, "Mechanistic origin of high strength in refractory BCC high entropy alloys up to 1900K," *Acta Materialia*, vol. 182, pp. 235–249, 2020.

[12] C. Lee, F. Maresca, R. Feng, Y. Chou, T. Ungar, M. Widom, K. An, J. D. Poplawsky, Y.-C. Chou, P. K. Liaw, and W. A. Curtin, "Strength can be controlled by edge dislocations in refractory high-entropy alloys," *Nature communications*, vol. 12, no. 1, p. 5474, 2021.

[13] C. Baruffi, F. Maresca, and W. A. Curtin, "Screw vs. edge dislocation strengthening in body-centered-cubic High Entropy Alloys and implications for guided alloy design," *MRS Communications*, vol. 122, no. 8, p. 448, 2022.

[14] G. Zhao, X. Li, and N. Petrinic, "Materials information and mechanical response of TRIP/TWIP Ti alloys," *npj Computational Materials*, vol. 7, no. 1, p. 809, 2021.

[15] J. W. Christian and S. Mahajan, "Deformation twinning," *Progress in Materials Science*, vol. 39, no. 1-2, pp. 1–157, 1995.

[16] G. Gottstein, *Materialwissenschaft und Werkstofftechnik*. Berlin, Heidelberg: Springer, 2014.

[17] R. Peierls, "The size of a dislocation," *Proceedings of the Physical Society*, vol. 52, no. 1, pp. 34–37, 1940.

[18] A. Seeger, "Peierls barriers, kinks, and flow stress: Recent progress," *Zeitschrift für Metallkunde*, vol. 93, no. 8, pp. 760–777, 2002.

[19] Cahn R.W. and Haasen, Peter, eds., *Physical Metallurgy: Volume III*. Amsterdam: Elsevier Science B.V., 4 ed., 1996.

[20] R. P. Carreker and R. W. Guard, "Tensile Deformation of Molybdenum as a function of Temperature and Strain Rate," *Journal of Metals*, vol. 8, no. 2, pp. 178–184, 1956.

[21] W. D. Jenkins, T. G. Digges, and C. R. Johnson, "Tensile properties of copper, nickel, and 70-percent-copper-30-percent-nickel and 30-percent-copper-70-percent-nickel alloys at high temperatures," *Journal of Research of the National Bureau of Standards*, vol. 58, no. 4, p. 201, 1957.

[22] W. D. Jenkins and T. G. Digges, "Effect of temperature on the tensile properties of high-purity nickel," *Journal of Research of the National Bureau of Standards)*, vol. 48, no. 4, pp. 313–321, 1952.

[23] H. J. Frost and M. F. Ashby, *Second report on deformation mechanism maps. Final report. AD 769821*. Cambridge: Harvard Univ., Div. of Engineering and Applied Physics, 1973.

[24] M. Yamaguchi and V. Vitek, "Core structures of non screw 1 / 2 (111) dislocations on (112) planes of b.c.c. crystals. I. Core structure in an unstressed crystal," *Reviews of Physics in Technology*, vol. 5, no. 1, pp. 1–10, 1975.

[25] E. Clouet, "Ab Initio Models of Dislocations," in *Handbook of Materials Modeling* (W. Andreoni and S. Yip, eds.), pp. 1503–1524, Cham: Springer International Publishing, 2020.

[26] B. G. Mendis, Y. Mishin, C. S. Hartley, and K. J. Hemker, "Use of the Nye tensor in analyzing HREM images of bcc screw dislocations," *Philosophical Magazine*, vol. 86, no. 29-31, pp. 4607–4640, 2006.

[27] J. P. Hirth and J. Lothe, *Theory of dislocations*. New York: Cambridge University Press, second ed., 1992.

[28] L. P. Kubin, B. Devincre, and M. Tang, "Mesoscopic modelling and simulation of plasticity in fcc and bcc crystals: Dislocation intersections and mobility," *Journal of Computer-Aided Materials Design*, vol. 5, no. 1, pp. 31–54, 1998.

[29] H. Park, M. R. Fellinger, T. J. Lenosky, W. W. Tipton, D. R. Trinkle, S. P. Rudin, C. F. Woodward, J. W. Wilkins, and R. G. Hennig, "Ab initio based empirical potential used to study the mechanical properties of molybdenum," *Physical Review B*, vol. 85, no. 21, p. 181, 2012.

[30] X. Wang, S. Xu, W.-R. Jian, X.-G. Li, Y. Su, and I. J. Beyerlein, "Generalized stacking fault energies and Peierls stresses in refractory body-centered cubic metals from machine learning-based interatomic potentials," *Computational Materials Science*, vol. 192, no. 5, p. 110364, 2021.

[31] F. C. Frank and W. T. Read, "Multiplication Processes for Slow Moving Dislocations," *Physical Review*, vol. 79, no. 4, pp. 722–723, 1950.

[32] R. Gröger and V. Vitek, "Explanation of the discrepancy between the measured and atomistically calculated yield stresses in body-centred cubic metals," *Philosophical Magazine Letters*, vol. 87, no. 2, pp. 113–120, 2007.

[33] J. R. Stephens and W. R. Witzke, "Alloy hardening and softening in binary molybdenum alloys as related to electron concentration," *Journal of the Less Common Metals*, vol. 29, no. 4, pp. 371–388, 1972.

[34] R. Fleischer, "Substitutional solution hardening," *Acta Metallurgica*, vol. 11, no. 3, pp. 203–209, 1963.

[35] R. Labusch, "A Statistical Theory of Solid Solution Hardening," *physica status solidi (b)*, vol. 41, no. 2, pp. 659–669, 1970.

[36] H. Suzuki, *A theory of solid solution hardening in body-centered cubic alloys*, vol. 6 of *Nachrichten der Akademie der Wissenschaften in Göttingen, Mathematisch-Physikalische Klasse*. Göttingen: Vandenhoeck & Ruprecht, 1971.

[37] I. Toda-Caraballo and P. E. Rivera-Díaz-del Castillo, "Modelling solid solution hardening in high entropy alloys," *Acta Materialia*, vol. 85, no. 5, pp. 14–23, 2015.

[38] S. I. Rao, E. Antillon, C. F. Woodward, B. Akdim, T. A. Parthasarathy, and O. N. Senkov, "Solution hardening in body-centered cubic quaternary alloys interpreted using Suzuki's kink-solute interaction model," *Scripta Materialia*, vol. 165, pp. 103–106, 2019.

[39] C. Varvenne, G. Leyson, M. Ghazisaeidi, and W. A. Curtin, "Solute strengthening in random alloys," *Acta Materialia*, vol. 124, no. 3, pp. 660–683, 2017.

[40] F. Maresca and W. A. Curtin, "Theory of screw dislocation strengthening in random BCC alloys from dilute to "High-Entropy" alloys," *Acta Materialia*, vol. 182, no. 309–310, pp. 144–162, 2020.

[41] I. H. Kim, H. S. Oh, S. J. Kim, and E. S. Park, "Rapid assessment of solid solution hardening via atomic size misfit parameter in refractory concentrated alloys," *Journal of Alloys and Compounds*, vol. 886, no. 3, p. 161320, 2021.

[42] D. Sturm, M. Heilmaier, J. H. Schneibel, P. Jéhanno, B. Skrotzki, and H. Saage, "The influence of silicon on the strength and fracture toughness of molybdenum," *Materials Science and Engineering: A*, vol. 463, no. 1-2, pp. 107–114, 2007.

[43] I. Wesemann, A. Hoffmann, T. Mrotzek, and U. Martin, "Investigation of solid solution hardening in molybdenum alloys," *International Journal of Refractory Metals and Hard Materials*, vol. 28, no. 6, pp. 709–715, 2010.

[44] H. Hattendorf and A. R. Büchner, "A Review of Suzuki's Solid Solution Hardening Theory for Substitutional bcc Alloys," *Zeitschrift für Metallkunde*, vol. 83, no. 9, pp. 690–698, 1992.

[45] S. I. Rao, C. F. Woodward, B. Akdim, O. N. Senkov, and D. B. Miracle, "Theory of solid solution strengthening of BCC Chemically Complex Alloys," *Acta Materialia*, vol. 209, no. C3, p. 116758, 2021.

[46] S. I. Rao, C. F. Woodward, and B. Akdim, "Solid solution softening and hardening in binary BCC alloys," *Acta Materialia*, vol. 243, no. 5, p. 118440, 2023.

[47] A. Ghafarollahi and W. A. Curtin, "Screw-controlled strength of BCC non-dilute and high-entropy alloys," *Acta Materialia*, vol. 226, no. 9, p. 117617, 2022.

[48] R. Fleischer, "Solution hardening," *Acta Metallurgica*, vol. 9, no. 11, pp. 996–1000, 1961.

[49] Haasen, Peter, "Solution Hardening in f.c.c. Metals," in *Dislocations in solids* (F. R. N. Nabarro, ed.), vol. 4, pp. 157–186, Amsterdam: North-Holland, 1979.

[50] L. Čižek, P. Kratochvíl, and B. Smola, "Solid solution hardening of copper crystals," *Journal of Materials Science*, vol. 9, no. 9, pp. 1517–1520, 1974.

[51] J. Friedrichs and P. Haasen, "Ternary solution-hardening of copper single crystals," *Philosophical Magazine*, vol. 31, no. 4, pp. 863–869, 1975.

[52] O. Vöhringer, "Temperatur- und Geschwindigkeitsabhängigkeit der Streckgrenze von α-Kupfer-Legierungen," *International Journal of Materials Research*, vol. 65, no. 1, pp. 32–36, 1974.

[53] G. Leyson and W. A. Curtin, "Friedel vs. Labusch: the strong/weak pinning transition in solute strengthened metals," *Philosophical Magazine*, vol. 93, no. 19, pp. 2428–2444, 2013.

[54] H. Suzuki, "Solid Solution hardening in b.c.c. alloys," in *Dislocations in solids* (F. R. N. Nabarro, ed.), vol. 4, pp. 193–216, Amsterdam: North-Holland, 1979.

[55] H. Suzuki, "Solid Solution Hardening," in *Strength of Metals and Alloys: Proceedings of the 5th International Conference, Aachen, Federal Republic of Germany, August 27-31, 1979* (Haasen, Peter, V. Gerold, and G. Kostorz, eds.), vol. 3 of *International Series on the Strength and Fracture of Materials and Structures*, pp. 1595–1614, Toronto, Ontario: Pergamon Press, 1980.

[56] S. Takeuchi, "Solid-Solution Strengthening in Single Crystals of Iron Alloys," *Journal of the Physical Society of Japan*, vol. 27, no. 4, pp. 929–940, 1969.

[57] S. I. Rao, C. F. Woodward, B. Akdim, and O. N. Senkov, "A model for interstitial solid solution strengthening of body centered cubic metals," *Materialia*, vol. 9, no. 4, p. 100611, 2020.

[58] G. Winkens, A. Kauffmann, J. K. Herrmann, A. K. Czerny, S. Obert, S. Seils, T. Boll, C. Baruffi, Y. Rao, W. A. Curtin, R. Schwaiger, and M. Heilmaier, "The influence of lattice misfit on screw and edge dislocation-controlled solid solution strengthening in Mo-Ti alloys," *Communications Materials*, vol. 4, no. 1, 2023.

[59] S. Laube, G. Winkens, A. Kauffmann, J. Li, C. Kirchlechner, and M. Heilmaier, "Strength of disordered and ordered al-containing refractory high-entropy alloys," *Advanced Engineering Materials*, vol. 26, no. 17, p. 2301797, 2024.

[60] J. M. Rosenberg and H. R. Piehler, "Calculation of the taylor factor and lattice rotations for bcc metals deforming by pencil glide," *Metallurgical Transactions*, vol. 2, no. 1, pp. 257–259, 1971.

[61] C. Varvenne, A. Luque, and W. A. Curtin, "Theory of strengthening in fcc high entropy alloys," *Acta Materialia*, vol. 118, no. 3, pp. 164–176, 2016.

[62] X. Wang, F. Maresca, and P. Cao, "The hierarchical energy landscape of screw dislocation motion in refractory high-entropy alloys," *Acta Materialia*, vol. 234, no. 12, p. 118022, 2022.

[63] A. Ghafarollahi and W. A. Curtin, "Theory of kink migration in dilute BCC alloys," *Acta Materialia*, vol. 215, no. 4, p. 117078, 2021.

[64] Y. Zhao, L. Dezerald, M. Pozuelo, X. Zhou, and J. Marian, "Simulating the mechanisms of serrated flow in interstitial alloys with atomic resolution over diffusive timescales," *Nature communications*, vol. 11, no. 1, p. 1227, 2020.

[65] P.-J. Yang, Q.-J. Li, T. Tsuru, S. Ogata, J.-W. Zhang, H.-W. Sheng, Z.-W. Shan, G. Sha, W.-Z. Han, J. Li, and E. Ma, "Mechanism of hardening and damage initiation in oxygen embrittlement of body-centred-cubic niobium," *Acta Materialia*, vol. 168, pp. 331–342, 2019.

[66] E. S. Fisher, D. G. Westlake, and S. T. Ockers, "Effects of hydrogen and oxygen on the elastic moduli of vanadium, niobium, and tantalum single crystals," *physica status solidi (a)*, vol. 28, no. 2, pp. 591–602, 1975.

[67] Q. Wei, L. Wang, Y. Fu, J. Qin, W. Lu, and Di Zhang, "Influence of oxygen content on microstructure and mechanical properties of Ti–Nb–Ta–Zr alloy," *Materials & Design*, vol. 32, no. 5, pp. 2934–2939, 2011.

[68] S. Obert, A. Kauffmann, S. Seils, S. Schellert, M. Weber, B. Gorr, H.-J. Christ, and M. Heilmaier, "On the chemical and microstructural requirements for the pesting-resistance of Mo–Si–Ti alloys," *Journal of Materials Research and Technology*, vol. 9, no. 4, pp. 8556–8567, 2020.

[69] G. F. Vander Voort, "Metallographic Specimen Preparation for Electron Backscattered Diffraction Part II*," *Practical Metallography*, vol. 48, no. 10, pp. 527–543, 2011.

[70] G. Calota, N. Maximova, K. S. Ziemer, and S. Müftü, "Investigation of Chemical/Mechanical Polishing of Niobium," *Tribology Transactions*, vol. 52, no. 4, pp. 447–459, 2009.

[71] Z. G. Neale, "Inductively coupled plasma optical emission spectroscopy (ICP-OES) Overview," 2020.

[72] TAZ Gesellschaft für Analyse UND Messtechnik mbH, "Thermal extraction with carrier gas: Analysis of the elements nitrogen (N), oxygen (O), hydrogen (H), carbon (C) and sulfur (S)."

[73] B. Gault, A. Chiaramonti, O. Cojocaru-Mirédin, P. Stender, R. Dubosq, C. Freysoldt, S. K. Makineni, T. Li, M. Moody, and J. M. Cairney, "Atom probe tomography," *Nature reviews. Methods primers*, vol. 1, no. 51, 2021.

[74] J. M. Cairney, D. W. Saxey, D. McGrouther, and S. P. Ringer, "Site-specific specimen preparation for atom probe tomography of grain boundaries," *Physica B: Condensed Matter*, vol. 394, no. 2, pp. 267–269, 2007.

[75] M. P. Moody, L. T. Stephenson, A. V. Ceguerra, and S. P. Ringer, "Quantitative binomial distribution analyses of nanoscale like-solute atom clustering and segregation in atom probe tomography data," *Microscopy research and technique*, vol. 71, no. 7, pp. 542–550, 2008.

[76] DIN-Normenausschuss Materialprüfung, "Stahl - Mikrophotographische Bestimmung der erkennbaren Korngröße (ISO 643:2019, korrigierte Fassung 2020-03); Deutsche Fassung ISO_643:2020."

[77] L. Spieß, G. Teichert, R. Schwarzer, H. Behnken, and C. Genzel, *Moderne Röntgenbeugung: Röntgendiffraktometrie für Materialwissenschaftler, Physiker und Chemiker*. Springer eBook Collection, Wiesbaden: Vieweg+Teubner, second ed., 2009.

[78] H. W. King and E. A. Payzant, "An Experimental Examination of Error Functions for Bragg-Brentano Powder Diffractometry," *Advances in X-ray Analysis*, vol. 36, pp. 663–670, 1992.

[79] A. Kumar and B. L. Eyre, "Grain boundary segregation and intergranular fracture in molybdenum," *Proceedings of the Royal Society of London. A. Mathematical and Physical Sciences*, vol. 370, no. 1743, pp. 431–458, 1980.

[80] D. Tabor, "The hardness of solids," *Reviews of Physics in Technology*, vol. 1, no. 3, pp. 145–179, 1970.

[81] DIN-Normenausschuss Materialprüfung, "Metallische Werkstoffe - Instrumentierte Eindringprüfung zur Bestimmung der Härte und anderer Werkstoffparameter - Teil 1: Prüfverfahren (ISO 14577-1:2015)."

[82] DIN-Normenausschuss Materialprüfung, "Metallische Werkstoffe – Härteprüfung nach Vickers – Teil 1: Prüfverfahren (ISO/DIS 6507-1:2022)."

[83] B. Merle, W. H. Higgins, and G. M. Pharr, "Extending the range of constant strain rate nanoindentation testing," *Journal of Materials Research*, vol. 35, no. 4, pp. 343–352, 2020.

[84] A. Karimzadeh, S. S. R. Koloor, M. R. Ayatollahi, A. R. Bushroa, and M. Y. Yahya, "Assessment of Nano-Indentation Method in Mechanical Characterization of Heterogeneous Nanocomposite Materials Using Experimental and Computational Approaches," *Scientific reports*, vol. 9, no. 1, p. 15763, 2019.

[85] T. Chudoba and F. Richter, "Investigation of creep behaviour under load during indentation experiments and its influence on hardness and modulus results," *Surface and Coatings Technology*, vol. 148, no. 2-3, pp. 191–198, 2001.

[86] W. C. Oliver and G. M. Pharr, "An improved technique for determining hardness and elastic modulus using load and displacement sensing indentation experiments," *Journal of Materials Research*, vol. 7, no. 6, pp. 1564–1583, 1992.

[87] W. C. Oliver and G. M. Pharr, "Measurement of hardness and elastic modulus by instrumented indentation: Advances in understanding and refinements to methodology," *Journal of Materials Research*, vol. 19, no. 1, pp. 3–20, 2004.

[88] Y.-T. Cheng and C.-M. Cheng, "Relationships between hardness, elastic modulus, and the work of indentation," *Applied Physics Letters*, vol. 73, no. 5, pp. 614–616, 1998.

[89] M. Yamamoto, M. Tanaka, and O. Furukimi, "Hardness-Deformation Energy Relationship in Metals and Alloys: A Comparative Evaluation Based

on Nanoindentation Testing and Thermodynamic Consideration," *Materials*, vol. 14, no. 23, 2021.

[90] J. Vlassak and W. Nix, "Measuring the elastic properties of anisotropic materials by means of indentation experiments," *Journal of the Mechanics and Physics of Solids*, vol. 42, no. 8, pp. 1223–1245, 1994.

[91] X. Li and B. Bhushan, "A review of nanoindentation continuous stiffness measurement technique and its applications," *Materials Characterization*, vol. 48, no. 1, pp. 11–36, 2002.

[92] P. Sudharshan Phani and W. C. Oliver, "A critical assessment of the effect of indentation spacing on the measurement of hardness and modulus using instrumented indentation testing," *Materials & Design*, vol. 164, p. 107563, 2019.

[93] W. Xiong, Y. Du, Y. Liu, B. Y. Huang, H. H. Xu, H. L. Chen, and Z. Pan, "Thermodynamic assessment of the Mo–Nb–Ta system," *Calphad*, vol. 28, no. 2, pp. 133–140, 2004.

[94] J. L. Murray, "The Mo−Ti (Molybdenum-Titanium) system," *Bulletin of Alloy Phase Diagrams*, vol. 2, no. 2, pp. 185–192, 1981.

[95] M. Hansen, E. L. Kamen, H. D. Kessler, and D. J. McPherson, "Systems Titanium-Molybdenum and Titanium-Columbium," *Journal of Metals*, vol. 3, no. 10, pp. 881–888, 1951.

[96] S. Terauchi, H. Matsumoto, T. Sugimoto, and K. Kamei, "Investigation of the Titanium-Molybdenum Binary Phase Diagram," *Journal of the Japan Institute of Metals*, vol. 41, no. 6, pp. 632–637, 1977.

[97] R. R. Hake, D. H. Leslie, and T. G. Berlincourt, "Electrical resistivity, Hall effect and superconductivity of some b.c.c. titanium-molybdenum alloys∗," *Journal of Physics and Chemistry of Solids*, vol. 20, no. 3-4, pp. 177–186, 1961.

[98] P. Duwez, "Effect of Rate of Cooling on the Alpha-Beta Transformation in Titanium and Titanium-Molybdenum Alloys," *Journal of Metals*, vol. 3, no. 9, pp. 765–771, 1951.

[99] E. W. Collings and J. C. Ho, "Physical Properties of Titanium alloys," in *The Science, Technology and Application of Titanium* (R. I. Jaffee and Promisel N. E., eds.), vol. 191, pp. 331–347, Oxford: Pergamon Press, 1970.

[100] E. Rudy, *Compendium of phase diagram data*. Ohio: Air Force Materials Laboratory, Metals and Ceramics Division, 1969.

[101] H. M. Flower, S. D. Henry, and D. R. F. West, "The $\beta \leftrightarrow \alpha$transformation in dilute Ti-Mo alloys," *Journal of Materials Science*, vol. 9, no. 1, pp. 57–64, 1974.

[102] S. C. Srivastava and L. L. Seigle, "Solubility and thermodynamic properties of oxygen in solid molybdenum," *Metallurgical Transactions*, vol. 5, no. 1, p. 271, 1974.

[103] B. Predel, "O-Ti (Oxygen-Titanium)," in *Ni-Np – Pt-Zr* (O. Madelung, ed.), vol. I of *Landolt-Börnstein - Group IV Physical Chemistry*, pp. 1–12, Berlin/Heidelberg: Springer, 1998.

[104] P. Samimi, D. A. Brice, I. Ghamarian, Y. Liu, and P. C. Collins, "Systematic Assessment of the Influence of Mo Concentration on the Oxygen Ingress in Ti–Mo System During High Temperature Oxidation," *Oxidation of Metals*, vol. 85, no. 3-4, pp. 357–368, 2016.

[105] R. Bryant, "The solubility of oxygen in transition metal alloys," *Journal of the Less Common Metals*, vol. 4, no. 1, pp. 62–68, 1962.

[106] A. Taylor and N. J. Doyle, "The solid-solubility of oxygen in Nb and Nb-rich Nb-Hf, Nb-Mo and Nb-W alloys," *Journal of the Less Common Metals*, vol. 13, no. 3, pp. 338–351, 1967.

[107] K. A. Chao and G. S. Ansell, "Electronic Effect on the Solubility of Interstitials in Transition Metal Alloys," *Journal of Applied Physics*, vol. 41, no. 1, pp. 417–421, 1970.

[108] M. E. Eberhart, T. E. Jones, M. A. Batchelder, and G. B. Olson, "Structure property relationships in the design of alloy composition: Moving beyond electron to atom ratios," *Journal of Materials Research*, vol. 20, no. 5, pp. 1330–1335, 2005.

[109] D. W. Jones, N. Pessall, and A. D. McQuillan, "Correlation between magnetic susceptibility and hydrogen solubility in alloys of early transition elements," *Reviews of Physics in Technology*, vol. 6, no. 63, pp. 455–459, 1961.

[110] P. Franke and D. Neuschütz, "Nb-O," in *Binary Systems. Part 4: Binary Systems from Mn-Mo to Y-Zr* (P. Franke and D. Neuschütz, eds.), vol. 19B4 of *Landolt-Börnstein - Group IV Physical Chemistry*, pp. 1–2, Berlin/Heidelberg: Springer, 2006.

[111] H. J. Goldschmidt and J. A. Brand, "The constitution of the chromium-niobium-molybdenum system," *Journal of the Less Common Metals*, vol. 3, no. 1, pp. 44–61, 1961.

[112] E. Rudy, C. E. Brukl, and S. Windisch, "Consititution of Niobium (Columbium)-Molybdenum-Carbon alloys," *Transactions of the Metallurgical Society of AIME*, vol. 239, no. 11, pp. 1796–1808, 1967.

[113] J. L. Murray, "The Ti−W (Titanium-Tungsten) system," *Bulletin of Alloy Phase Diagrams*, vol. 2, no. 2, pp. 192–196, 1981.

[114] T. Górecki, "The relations between the shear modulus, the bulk modulus and young's modulus for polycrystalline metallic elements," *Materials Science and Engineering*, vol. 43, no. 3, pp. 225–230, 1980.

[115] W. Köster, "Die Temperaturabhängigkeit des Elastizitätsmoduls reiner Metalle," *Zeitschrift für Metallkunde*, vol. 39, no. 1, pp. 1–9, 1948.

[116] C. D. Statham, D. Vesely, and J. W. Christian, "Slip in single crystals of niobium-molybdenum alloys deformed in compression," *Acta Metallurgica*, vol. 18, no. 12, pp. 1243–1252, 1970.

[117] B. C. Peters and A. A. Hendrickson, "Solid solution strengthening in Nb-Ta and Nb-Mo alloy single crystals," *Metallurgical Transactions*, vol. 1, no. 8, pp. 2271–2280, 1970.

[118] I. Milne and R. E. Smallman, "Plastic Deformation of Niobium (Columbium)-Molybdenum Alloy Single Crystals," *Transactions of the Metallurgical Society of AIME*, no. 242(1), pp. 120–127, 1968.

[119] E. Miura, K. Yoshimi, and S. Hanada, "Solid-Solution Strengthening by Oxygen in Nb-Ta and Nb-Mo Single Crystals," *physica status solidi (a)*, vol. 185, no. 2, pp. 357–372, 2001.

[120] C. Minnert, H. ur Rehman, and K. Durst, "Thermally activated dislocation mechanism in Mo studied by indentation, compression and impact testing," *Journal of Materials Research*, vol. 36, no. 12, pp. 2397–2407, 2021.

[121] J.-F. Croteau, M. Peroni, S. Atieh, N. Jacques, and E. Cantergiani, "Effect of Strain Rate on the Tensile Mechanical Properties of Electron Beam Welded OFE Copper and High-Purity Niobium for SRF Applications," *Journal of Dynamic Behavior of Materials*, vol. 7, no. 3, pp. 485–498, 2021.

[122] W. D. Nix and H. Gao, "Indentation size effects in crystalline materials: A law for strain gradient plasticity," *Journal of the Mechanics and Physics of Solids*, vol. 46, no. 3, pp. 411–425, 1998.

[123] P. M. Rice and R. E. Stoller, "Correlation of Nanoindentation and Conventional Mechanical Property Measurements," *MRS Proceedings*, vol. 649, p. 462, 2000.

[124] Y. Yang, C. Zhang, Z. Ding, C. Su, T. Yan, Y. Song, and Y. Cheng, "A correlation between micro- and nano-indentation on materials irradiated by high-energy heavy ions," *Journal of Nuclear Materials*, vol. 498, no. 21, pp. 129–136, 2018.

[125] N. A. Sakharova, J. V. Fernandes, J. M. Antunes, and M. C. Oliveira, "Comparison between Berkovich, Vickers and conical indentation tests: A three-dimensional numerical simulation study," *International Journal of Solids and Structures*, vol. 46, no. 5, pp. 1095–1104, 2009.

[126] S. Jakob, A. Leitner, A. Lorich, M. Eidenberger-Schober, W. Knabl, R. Pippan, H. Clemens, and V. Maier-Kiener, "Influence of crystal orientation and Berkovich tip rotation on the mechanical characterization of grain boundaries in molybdenum," *Materials & Design*, vol. 182, p. 107998, 2019.

[127] R. Hill, "The Elastic Behaviour of a Crystalline Aggregate," *Zeitschrift für Angewandte Mathematik und Mechanik*, vol. 65, no. 5, pp. 349–354, 1952.

[128] W. Voigt, *Lehrbuch der Kristallphysik*. Wiesbaden: Vieweg+Teubner, 1966.

[129] A. Reuss, "Berechnung der Fließgrenze von Mischkristallen auf Grund der Plastizitätsbedingung für Einkristalle," *Zeitschrift für Angewandte Mathematik und Mechanik*, vol. 9, no. 1, pp. 49–58, 1929.

[130] J. P. Hirth and J. Lothe, "Elastic and Core Anisotropies for the ⟨111⟩ Screw Dislocation in Cubic Crystals," *physica status solidi (b)*, vol. 15, no. 2, pp. 487–494, 1966.

[131] A. Foreman, "Dislocation energies in anisotropic crystals," *Acta Metallurgica*, vol. 3, no. 4, pp. 322–330, 1955.

[132] U. F. Kocks, A. S. Argon, and M. F. Ashby, *Thermodynamics and kinetics of slip*, vol. 19 of *Progress in materials science*. Oxford: Pergamon Press, 1. ed. ed., 1975.

[133] J. M. Dickinson and P. E. Armstrong, "Temperature Dependence of the Elastic Constants of Molybdenum," *Journal of Applied Physics*, vol. 38, no. 2, pp. 602–606, 1967.

[134] W. Petry, A. Heiming, J. Trampenau, Alba M., C. Herzig, H. R. Schober, and G. Vogl, "Phonon dispersion of the bcc phase of group-IV metals. I. bcc titanium," *Physical Review B*, vol. 43, no. 13, pp. 10933–10947, 1991.

[135] K. J. Carroll, "Elastic Constants of Niobium from 4.2° to 300°K," *Journal of Applied Physics*, vol. 36, no. 11, pp. 3689–3690, 1965.

[136] W. C. Hubbell and F. R. Brotzen, "Elastic constants of niobium–molybdenum alloys in the temperature range −190 to +100°C," *Transactions of the Metallurgical Society of AIME*, vol. 43, no. 8, pp. 3306–3312, 1972.

[137] R. L. Smialek and T. E. Mitchell, "Interstitial solution hardening in tantalum single crystals," *Reviews of Physics in Technology*, vol. 22, no. 180, pp. 1105–1127, 1970.

[138] K. V. Ravi and R. Gibala, "Dislocation dynamics in niobium-oxygen," *Metallurgical Transactions*, vol. 3, no. 12, pp. 3081–3085, 1972.

[139] O. N. Carlson, D. G. Alexander, and G. Elssner, "The effect of oxygen on the strength and ductility of polycrystalline vanadium in the range of 4.2 to 400 K," *Metallurgical and Materials Transactions A*, vol. 8, no. 1, pp. 99–104, 1977.

[140] X. Min, P. Bai, S. Emura, X. Ji, C. Cheng, B. Jiang, and K. Tsuchiya, "Effect of oxygen content on deformation mode and corrosion behavior in β-type Ti-Mo alloy," *Materials Science and Engineering: A*, vol. 684, pp. 534–541, 2017.

[141] Y. Wu, Q. Wang, D. Lin, X. Chen, T. Wang, W. Y. Wang, Y. Wang, and X. Hui, "Phase Stability and Deformation Behavior of TiZrHfNbO High-Entropy Alloys," *Frontiers in Materials*, vol. 7, p. 100, 2020.

[142] L. K. Iroc, O. U. Tukac, B. B. Tanrisevdi, O. El-Atwani, M. A. Tunes, Y. E. Kalay, and E. Aydogan, "Design of oxygen-doped TiZrHfNbTa refractory high entropy alloys with enhanced strength and ductility," *Materials & Design*, vol. 223, p. 111239, 2022.

[143] D. Nguyen-Manh, A. P. Horsfield, and S. L. Dudarev, "Self-interstitial atom defects in bcc transition metals: Group-specific trends," *Journal of Nuclear Materials*, vol. 73, no. 2, p. 67, 2006.

[144] R. E. Kubilay, A. Ghafarollahi, F. Maresca, and W. A. Curtin, "High energy barriers for edge dislocation motion in body-centered cubic high entropy alloys," *npj Computational Materials*, vol. 7, no. 1, p. 698, 2021.

[145] A. Tunde Raji, S. Scandolo, R. Mazzarello, S. Nsengiyumva, M. Härting, and D. T. Britton, "Ab initio pseudopotential study of vacancies and self-interstitials in hcp titanium," *Philosophical Magazine*, vol. 89, no. 20, pp. 1629–1645, 2009.

[146] H. R. Schober and P. H. Dederichs, "Mo," in *Phonon States of Elements. Electron States and Fermi Surfaces of Alloys* (K.-H. Hellwege and J. L. Olsen, eds.), vol. 13a of *Landolt-Börnstein - Group III Condensed Matter*, pp. 86–92, Berlin/Heidelberg: Springer, 1981.

[147] R. I. Sharp, "The lattice dynamics of niobium I. Measurements of the phonon frequencies," *Journal of Applied Physics*, vol. 2, no. 3, pp. 421–431, 1969.

[148] G. Schoeck, "The Activation Energy of Dislocation Movement," *physica status solidi (b)*, vol. 8, no. 2, pp. 499–507, 1965.

[149] D. Brunner and V. Glebovsky, "Analysis of flow-stress measurements of high-purity tungsten single crystals," *Materials Letters*, vol. 44, no. 3-4, pp. 144–152, 2000.

[150] D. Wen and M. S. Titus, "pySSpredict: A python-based solid-solution strength prediction toolkit for complex concentrated alloys," *Computational Materials Science*, vol. 220, no. 11, p. 111977, 2023.

[151] G. Winkens, "Solid solution strengthening in Mo-Nb modelled using the Suzuki approach." 10.5445/ir/1000157208.

[152] M. Semchyshen, "Development and properties of arc-cast molybdenum-base alloys," in *The Metal Molybdenum: Proceedings of a Symposium Held September 18 and 19, 1956 at Rackham Memorial Building, Engineering Society of Detroit, Detroit, Michigan* (J. J. Harwood, ed.), American Society for Metals, 1958.

[153] A. Ghafarollahi, F. Maresca, and W. A. Curtin, "Solute/screw dislocation interaction energy parameter for strengthening in bcc dilute to high entropy alloys," *Transactions of the Metallurgical Society of AIME*, vol. 27, no. 8, p. 085011, 2019.

[154] A. Ghafarollahi and W. A. Curtin, "Theory of double-kink nucleation in dilute BCC alloys," *Acta Materialia*, vol. 196, no. 5754, pp. 635–650, 2020.

[155] L. Dezerald, L. Proville, L. Ventelon, F. Willaime, and D. Rodney, "First-principles prediction of kink-pair activation enthalpy on screw dislocations in bcc transition metals: V, Nb, Ta, Mo, W, and Fe," *Physical Review B*, vol. 91, no. 9, p. 244, 2015.

[156] Y.-J. Hu, M. R. Fellinger, B. G. Butler, Y. Wang, K. A. Darling, L. J. Kecskes, D. R. Trinkle, and Z.-K. Liu, "Solute-induced solid-solution softening and hardening in bcc tungsten," *Acta Materialia*, vol. 141, pp. 304–316, 2017.

[157] M. Niinomi, Y. Liu, M. Nakai, H. Liu, and H. Li, "Biomedical titanium alloys with Young's moduli close to that of cortical bone," *Regenerative biomaterials*, vol. 3, no. 3, pp. 173–185, 2016.

[158] R. Darvishi Kamachali and L. Wang, "Elastic energy of multi-component solid solutions and strain origins of phase stability in high-entropy alloys," *Scripta Materialia*, vol. 206, p. 114226, 2022.

[159] "Spinger materials - properties of materials." https://materials.springer.com/, 2023. Accessed: 01.09.2023.

[160] J. L. Murray, "The Ti−Zr (Titanium-Zirconium) system," *Bulletin of Alloy Phase Diagrams*, vol. 2, no. 2, pp. 197–201, 1981.

[161] F. Hinrichs. private communication, 05.07.2023.

[162] B. Yin, F. Maresca, and W. A. Curtin, "Vanadium is an optimal element for strengthening in both fcc and bcc high-entropy alloys," *Acta Materialia*, vol. 188, pp. 486–491, 2020.